Technical Report Documentation Page

1. Report No.	2. Government Accession No.	3. Recipient's Catalog No.
FHWA/TX-03/1857-2		

4. Title and Subtitle	5. Report Date
Nondestructive Testing of Prestressed Bridge Girders with Distributed Damage	August 2002
	6. Performing Organization Code
7. Author(s)	8. Performing Organization Report No.
B. V. Tinkey, T. J. Fowler, and R. E. Klingner	Research Report 1857-2
9. Performing Organization Name and Address	10. Work Unit No. (TRAIS)
Center for Transportation Research The University of Texas at Austin 3208 Red River, Suite 200 Austin, TX 78705-2650	11. Contract or Grant No. Research Study 0-1857
12. Sponsoring Agency Name and Address	13. Type of Report and Period Covered
Texas Department of Transportation Research and Technology Transfer Section, Construction Division P.O. Box 5080 Austin, TX 78763-5080	Research Report (9/99-8/02)
	14. Sponsoring Agency Code

15. Supplementary Notes

Project conducted in cooperation with the U.S. Department of Transportation, Federal Highway Administration, and the Texas Department of Transportation.

16. Abstract

Four different nondestructive tests were evaluated for detecting and quantifying the amount of distributed damage in prestressed concrete bridge girders. This was in response to a number of bridges throughout Texas exhibiting premature concrete deterioration due to a combination of delayed ettringite formation and alkali silica reaction.

Visual inspection, acoustic emission, short pulse radar, and impact echo are described, and possible procedures to apply these methods to concrete with distributed damage are presented and evaluated.

17. Key Words	18. Distribution Statement
nondestructive evaluation, acoustic emission, concrete, damage, rehabilitation, ettringite	No restrictions. This document is available to the public through the National Technical Information Service, Springfield, Virginia 22161.

19. Security Classif. (of report)	20. Security Classif. (of this page)	21. No. of pages	22. Price
Unclassified	Unclassified	106	

Form DOT F 1700.7 (8-72) Reproduction of completed page authorized

Nondestructive Testing of Prestressed Bridge Girders with Distributed Damage

by

B. V. Tinkey, T. J. Fowler, and R. E. Klingner

Research Report 1857-2

Research Project 0-1857

STRUCTURAL ASSESSMENT OF IN-SERVICE BRIDGES WITH PREMATURE CONCRETE DETERIORATION

conducted for the

Texas Department of Transportation

in cooperation with the

U.S. Department of Transportation
Federal Highway Administration

by the

CENTER FOR TRANSPORTATION RESEARCH
BUREAU OF ENGINEERING RESEARCH
THE UNIVERSITY OF TEXAS AT AUSTIN

November 2000

Research performed in cooperation with the Texas Department of Transportation and the U.S. Department of Transportation, Federal Highway Administration.

ACKNOWLEDGEMENTS

We greatly appreciate the financial support from the Texas Department of Transportation that made this project possible. The support of the project director, Brian Merrill (BRG), program coordinator, Jeff Seiders (CST), and former program coordinator Lee Lawrence (MAT), is also very much appreciated. We thank Project Monitoring Committee members, Keith Ramsey (BRG), Thomas Rummell (BRG), John Vogel (HOU), and Moon Won (CST).

DISCLAIMER

The contents of this report reflect the views of the authors, who are responsible for the facts and the accuracy of the data presented herein. The contents do not necessarily reflect the view of the Federal Highway Administration or the Texas Department of Transportation. This report does not constitute a standard, specification, or regulation.

NOT INTENDED FOR CONSTRUCTION,

PERMIT, OR BIDDING PURPOSES

T. J. Fowler

R. E. Klingner, Texas P.E. #42483

Research Supervisors

TABLE OF CONTENTS

CHAPTER 1 – INTRODUCTION 1

1.1 BACKGROUND OF PROJECT 1

1.2 BACKGROUND OF PROJECT 1

1.3 SCOPE OF THIS THESIS 1

1.4 ORGANIZATION OF THESIS 2

CHAPTER 2 – DESCRIPTION OF TEST SPECIMENS 3

2.1 DESCRIPTION OF BOX GIRDERS 3

2.2 DESCRIPTION OF TYPE C GIRDERS 5

CHAPTER 3 – VISUAL INSPECTION 7

3.1 INTRODUCTION TO VISUAL INSPECTION 7

3.2 APPLICATION OF VISUAL INSPECTION TO CONCRETE 7

3.3 RESULTS OF VISUAL INSPECTION ON BOX GIRDER SECTIONS 7

3.4 RESULTS OF VISUAL INSPECTION ON TYPE C GIRDER SECTIONS 13

3.5 DISCUSSION 15

3.6 CONCLUSION 16

CHAPTER 4 – ACOUSTIC EMISSION 17

4.1 INTRODUCTION TO ACOUSTIC EMISSION 17

4.2 APPLICATION OF ACOUSTIC EMISSION TO CONCRETE IN GENERAL 18

4.2.1 Difficulties with Acoustic Emission in Concrete 18

4.2.2 Kaiser Effect 20

4.2.3 Rate Process Analysis 21

4.2.4 Moment Tensor Analysis 21

4.3 ACOUSTIC EMISSION RESPONSE OF FLEXURAL CRACKING IN UNREINFORCED CONCRETE 23

4.3.1 Test Setup 23

4.3.2 Analysis and Results 25

4.3.3 Discussion 28

4.4 AE RESPONSE OF FULL SCALE PRESTRESSED BOX GIRDERS IN FLEXURE 28

4.4.1 Setup of Flexure-Dominated Box Girder Tests 28

4.4.2 Results of Flexure-Dominated Tests on Box Girders 32

4.4.3 Discussion of Flexure-Dominated Tests on Box Girders 38

4.5 AE RESPONSE OF FULL SCALE PRESTRESSED BOX GIRDERS IN SHEAR 40

4.5.1 Setup of Shear-Dominated Tests on Box Girders 40

4.5.2 Results of the Shear-Dominated Tests on Box Girders 42
4.5.3 Discussion of the Shear-Dominated Tests on Box Girders 51
4.6 SHEAR TESTS OF FULL SCALE TYPE C GIRDERS 53
4.6.1 Test Setup for Shear-Dominated Test on Type C Girders 53
4.6.2 Results of Shear-Dominated Test on Type C Girders 54
4.6.3 Discussion of Shear-Dominated Tests on Type C Girders 65
4.7 DISCUSSION OF ACOUSTIC EMISSION TESTING AND EVALUATION CRITERIA 66
4.8 CONCLUSIONS FROM ACOUSTIC EMISSION TESTING 68

CHAPTER 5 – SHORT-PULSE RADAR 69
5.1 INTRODUCTION TO SHORT PULSE RADAR 69
5.2 TEST SETUP 71
5.3 RESULTS OF THE SHORT PULSE RADAR SURVEY 72
5.4 DISCUSSION 73
5.5 CONCLUSION 74

CHAPTER 6 – IMPACT-ECHO 75
6.1 INTRODUCTION TO IMPACT-ECHO 75
6.2 APPLICATION OF IMPACT-ECHO TO CONCRETE WITH DISTRIBUTED DAMAGE 77
6.3 TESTING PROGRAM 78
6.4 RESULTS 84
6.5 DISCUSSION OF IMPACT ECHO RESULTS 85
6.6 CONCLUSIONS REGARDING IMPACT-ECHO 86

CHAPTER 7 – SUMMARY AND CONCLUSIONS 87
7.1 VISUAL INSPECTION 87
7.2 ACOUSTIC EMISSION 87
7.3 SHORT-PULSE RADAR 87
7.4 IMPACT-ECHO 88
7.5 CONCLUSIONS AND RECOMMENDATIONS 88

APPENDIX – IMPACT-ECHO DATA 89

REFERENCES 95

LIST OF FIGURES

Figure 2.1 – Cross-Section Dimensions of Box Girder Specimens 3
Figure 2.2 – Plan View of Box Girder 4
Figure 2.3 – Overall View of Box Girder 4
Figure 2.4 – Typical End Conditions of Girders with Intermediate Damage 4
Figure 2.5 – Cross Section of the Type C Specimens 6
Figure 2.6 – View of Type C Girder with Slab Prior to Testing 6
Figure 3.1 – End View of A-Side of BG1 8
Figure 3.2 – Side of BG1 at A-End 8
Figure 3.3 – End View of B-End of BG1 9
Figure 3.4 – Side View of B-Side of BG1 9
Figure 3.5 – Spalled Concrete on Specimen BG2 10
Figure 3.6 – End Damage on Specimen BG2 10
Figure 3.7 – End View of A-End of BG3 11
Figure 3.8 – Side View on B-End of BG3 11
Figure 3.9 – Damage at Interior Blockout on BG3 12
Figure 3.10 – Side View of A-End of BG4 12
Figure 3.11 – Typical Damage along the Length of BG4 13
Figure 3.12 – Northwest end of BG4 13
Figure 3.13 – West End of Girder 1 14
Figure 3.14 – East End of Girder 1 15
Figure 3.15 – East End of Girder 2 15
Figure 4.1 – Sample Acoustic Emission Waveform Showing Evaluation Parameters 17
Figure 4.2 – Example of Rectified Acoustic Emission Waveform Illustrating MARSE 18
Figure 4.3 – Example of Attenuation in Concrete (Uomoto 1987) 19
Figure 4.4 – Typical Graphs Showing Attenuation of Acoustic Emission in Concrete (Uomoto 1987) 19
Figure 4.5 – Moment Tensor Results on Prestressed Girder (Yepez 1997) 22
Figure 4.6 – Experimental Setup Used for Plain Concrete Tests 23
Figure 4.7 – Dimensions of plain concrete specimens 24
Figure 4.8 – AE Response of a Typical Notched Specimen 25
Figure 4.9 – Historic Index for a Typical Prenotched Specimen 26
Figure 4.10 – Typical AE Response of Notch Free Specimen 27
Figure 4.11 – Historic Index for a Typical Notch free Specimen 28
Figure 4.12 – Detail of Spreader Beams used in Flexure Tests 29
Figure 4.13 – BG1 Prior to Testing 29

Figure 4.14 – Loading Schedule for BG1 30
Figure 4.15 – Attenuation Curve for R6I Sensor 31
Figure 4.16 – Plan View of Sensor Locations on Box Girder Specimens 31
Figure 4.17 – Load vs. Cumulative MARSE before Cracking for BG1 32
Figure 4.18 – Time Based Graphs for BG1 34
Figure 4.19 – Cumulative MARSE vs, Load for BG2 35
Figure 4.20 – Time Based Graphs for BG2 36
Figure 4.21 – Cumulative MARSE vs. Load for BG4 37
Figure 4.22 – Time Based Graphs for BG4 38
Figure 4.23 – Felicity Effect for Flexure Specimens 39
Figure 4.24 – Test Setup for BG1S and BG4S 40
Figure 4.25 – Test Setup of BG2S 41
Figure 4.26 – Sensor Locations on all Shear Specimens 41
Figure 4.27 – Loading Schedule for BG1S 42
Figure 4.28 – Load Vs Cumulative MARSE for BG1S 42
Figure 4.29 – Time Based Graphs for BG1S 44
Figure 4.30 – Cumulative MARSE vs. Load for BG2S 45
Figure 4.31 – Time Based Graphs for BG2S 46
Figure 4.32 – Bearing Failure of BG4S 47
Figure 4.33 – Compression Strut Failure of BG1S 47
Figure 4.34 – Amplitude vs Log Duration for BG4S 48
Figure 4.35 – Amplitude vs Log Duration for BG4S after Swansong II Filter 49
Figure 4.36 – Cumulative MARSE vs. Load for BG4S 49
Figure 4.37 – Time Based Graphs for BG4S 51
Figure 4.38 – Felicity Ratios for the Shear-Dominated Test on Box Girders 52
Figure 4.39 – Test Setup for Type C Girders 53
Figure 4.40 – Sensor Placement for Type C Specimens 54
Figure 4.41 – Loading Schedule for G2WS 55
Figure 4.42 – Cumulative MARSE vs. Load for G2WS 55
Figure 4.43 – Time Based Graphs for G2WS 56
Figure 4.44 – Loading Schedule for G2ES 57
Figure 4.45 – Cumulative MARSE vs. Load for G2ES 57
Figure 4.46 – Time Based Graphs for G2ES 59
Figure 4.47 – Loading Schedule for G1WS 60
Figure 4.48 – G1WS under test at 270 kips 60
Figure 4.49 – Cumulative MARSE vs. Load for G1WS 61
Figure 4.50 – Time Based Graphs for G1WS 62

Figure 4.51 – Loading Schedule for G1ES 63
Figure 4.52 – Cumulative MARSE vs. Load for G1ES 63
Figure 4.53 – Time Based Graphs for G1ES 65
Figure 4.54 – Felicity Ratios for the Shear Tests on Type C Girders 66
Figure 4.55 – Proposed Evaluation Criteria and Test Results 67
Figure 5.1 – Propagation of Electromagnetic Waves through Media of Different Dielectric Constants 70
Figure 5.2 – Typical A-Scan and B-Scan from Sample BG2 71
Figure 5.3 – Short Pulse Radar Equipment 72
Figure 5.4 – Dielectric Values on West Side of BG2 73
Figure 5.5 – Dielectric Values on East Side of BG2 at the A-End 73
Figure 5.6 – Dielectric Values on the East Side of BG4 73
Figure 6.1 – Schematic Representation of Impact-Echo Test 75
Figure 6.2 – Typical Displacement History for an Impact-Echo Test 76
Figure 6.3 – Frequency Spectrum of a Typical Impact-Echo Test 76
Figure 6.4 – Calculation of the Decay Coefficient 78
Figure 6.5 – Photo of the Test Point 8 feet from Centerline on BG1 79
Figure 6.6 – Photo of the Test Point 7 feet from the South End of BG1 80
Figure 6.7 – Photo of the Test Point 3 feet from the North End of BG3 81
Figure 6.8 – Photo of the Test Point 22 feet from the South End of BG3 81
Figure 6.9 – Photo of DOCtor Impact-Echo Equipment 82
Figure 6.10 – (a) Unfiltered Displacement History in Time Domain (b) Unfiltered Frequency Spectrum 83
Figure 6.11 – (a) Filtered Displacement History in Time Domain (b) Filtered Frequency Spectrum 83
Figure 6.12 – Results of Filtering the Displacement History 86

LIST OF TABLES

Table 2.1 – Description of Tests on Box Girder Specimens 5
Table 3.1 – Crack Ratios for Type C Girders 14
Table 4.1 – Felicity Ratios for the Second and Third Loading (Yuyama and Murakami 1996) 21
Table 4.2 – Properties of Mixtures Used on Plain Concrete Specimens 24
Table 4.3 – Test Parameters for Unreinforced Concrete Specimens 25
Table 4.4 – K values used in Historic Index (Fowler et al. 1989) 26
Table 4.5 – Test Parameters for Full-Scale Tests 32
Table 4.6 – Felicity Ratios for BG1 33
Table 4.7 – Values for K used in Calculating Historic Index 33
Table 4.8 – Felicity Ratios for BG2 35
Table 4.9 – Felicity Ratios for BG4 37
Table 4.10 – Felicity Ratios for BG1S 43
Table 4.11 – Felicity Ratios for BG2S 45
Table 4.12 – Definition of a "Telltale" Hit for the Swansong II Filter 48
Table 4.13 – Felicity Ratios for BG4S 50
Table 4.14 – Crack Ratios for Type C Girders 53
Table 4.15 – Dimensions of Test Setup 54
Table 4.16 – Dimension for Sensor Placement on Type C Girders 54
Table 4.17 – Felicity Ratios for G2ES 58
Table 4.18 – Felicity Ratios for G1WS 61
Table 4.19 – Felicity Ratios for G1ES 64
Table 4.20 – Suggested Evaluation Criteria for Distributed Damage 67
Table 5.1 – Typical Dielectric Constants for Various Materials 69
Table 6.1 – Results of Finite Element Models for 130 mm Thick Concrete Plate (Kesner 1997) 78
Table 6.2 – Results of Impact-Echo Tests on BG1 84
Table 6.3 – Results of Impact-Echo Tests on BG3 84
Table 6.4 – Decay Constants for a Test Performed on BG3 85

SUMMARY

Four different nondestructive tests were evaluated for detecting and quantifying the amount of distributed damage in prestressed concrete bridge girders. This was in response to a number of bridges throughout Texas exhibiting premature concrete deterioration due to a combination of delayed ettringite formation and alkali silica reaction.

Visual inspection, acoustic emission, short pulse radar, and impact echo are described, and possible procedures to apply these methods to concrete with distributed damage are presented and evaluated.

CHAPTER 1 – INTRODUCTION

Throughout Texas, many bridges are currently experiencing premature concrete deterioration due to a combination of delayed ettringite formation and alkali-silica reaction. The Texas Department of Transportation (TxDOT) has sponsored Research Project 1857 to help decide whether to repair or replace these bridges. The goal of this research is to determine how the amount of deterioration can be quantified, how quickly it is progressing, and how it affects the strength of those bridges.

1.1 BACKGROUND OF PROJECT

Within the last 10 years, TxDOT became aware of deterioration in several prestressed girders throughout the state. The damage is due to a combination of delayed ettringite formation and alkali-silica reaction (Lawrence 1997). During a statewide bridge inspection program, other bridges throughout Texas that were built around the same time were determined to have the same problem. A few examples of these bridges include:

- Woodlands Parkway and IH45 in Houston;
- US90 and San Jacinto River;
- FM 1979 at Lake Ivie in Concho County;
- US 54 and Sheridan Road in El Paso;

Project 1857 was implemented to determine how the deterioration affects the long-term serviceability and strength of structures in service.

1.2 BACKGROUND OF PROJECT

The original scope of the project as outlined in the project proposal (Klingner and Fowler 1998) consists of seven tasks:

Task 1 – Conduct field investigations to confirm and monitor existing premature concrete deterioration, the rate of increase of such deterioration, and the effect of different remedial measures on that rate of increase.

Task 2 – Conduct laboratory investigations of local effects of premature concrete deterioration.

Task 3 – Develop nondestructive evaluation techniques for determining degree and type of concrete deterioration.

Task 4 – Develop petrographic techniques for assessing severity of deterioration from samples taken from field investigations.

Task 5 – Develop engineering models for evaluating the global reduction in capacity of a structural element due to local premature concrete deterioration.

Task 6 – Develop an overall methodology for predicting the probable loss in capacity over time of a deteriorated structural element, based on external evidence, nondestructive evaluation, and engineering models.

Task 7 – Develop recommended actions by TxDOT for handling any given case of premature concrete deterioration.

1.3 SCOPE OF THIS REPORT

The overall scope of this report can be directly related to Task 3 as outlined in Section 1.2, and consists of the following 3 objectives:

- Develop nondestructive tests to detect concrete deterioration.
- Once deterioration is detected, use nondestructive tests to determine the degree and location of damage.
- In the presence of distributed damage, suggest methods to further monitor the deterioration.

To accomplish these tasks, four possible nondestructive test methods were identified and preliminary tests were performed to evaluate their effectiveness in quantifying distributed damage in concrete. These test methods were visual inspection, short-pulse radar, impact-echo, and acoustic emission.

Possible methods that are not covered here are liquid-penetrant, radiography, and ultrasonics. Liquid penetrant was not investigated deeply because all the deteriorated specimens have extensive map cracking (small, shallow cracks distributed in a spider-web pattern) making it difficult to distinguish between different degrees of damage. Radiography was not researched due to safety issues and the large radiation source that would be required for concrete. Ultrasonics was initially ruled out due to the high attenuation of ultrasound in concrete, but will be investigated later by Piya Chotickai, another researcher on the project. His research will consist of evaluating additional test methods and developing test procedures for bridges in service.

1.4 ORGANIZATION OF REPORT

Since each nondestructive test method is independent, this report is organized with each test method in a separate chapter. In addition, a separate chapter is dedicated to describing test specimens, which are similar for every method. Therefore, Chapter 2 describes the specimens used for all of the test methods; Chapter 3 discusses visual inspection; Chapter 4 discusses acoustic emission; Chapter 5 discusses short-pulse radar; Chapter 6 discusses impact-echo; and Chapter 7 summarizes findings and presents principal conclusions and recommendations.

CHAPTER 2 – DESCRIPTION OF TEST SPECIMENS

Nondestructive testing was performed on two different prestressed girder sections: a box section, and a Type C section. The specimens were experiencing varying degrees of damage from a combination of delayed ettringite formation (DEF) and alkali-silica reaction (ASR).

The specimens described in this chapter were tested at the Ferguson Structural Engineering Laboratory at the J.J. Pickle Research Campus of The University of Texas at Austin.

2.1 DESCRIPTION OF BOX GIRDERS

Four prestressed concrete box girders were shipped to Ferguson Structural Engineering Laboratory in the spring of 1999 from the Heldenfels Brothers, Inc. plant in San Marcos, Texas. These girders were chosen from approximately 55 similar girders that displayed distributed damage early enough that they were never put into service. Since they were cast in September of 1991, the girders had been stored outside and exposed to weather in the casting yard.

Dimensions of the cross section are shown in Figure 2.1. The overall dimensions of the girders are 4 feet wide and 27 inches tall. The wall thickness is 5 inches with a styrofoam filler that was used as formwork for the void. The void was included to conserve concrete and decrease weight. In addition, 30 - ½ inch, 270 ksi, low-relaxation prestressing strands are spaced at 2-inch intervals as shown in the figure. Concrete design strength was 6000 psi; the actual strength measured from cores taken after testing, however, was closer to 10,000 psi.

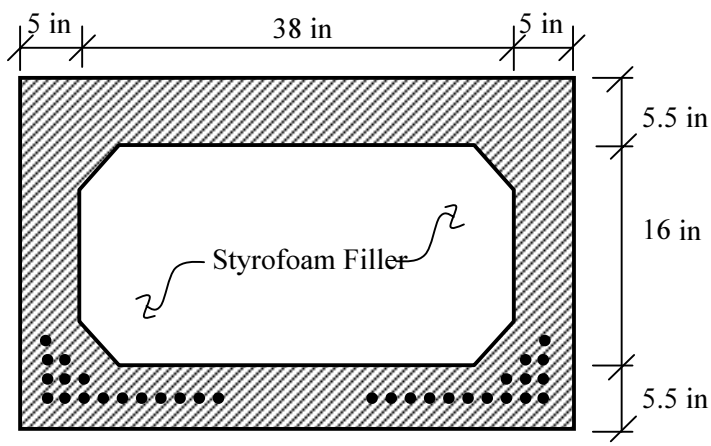

Figure 2.1 – Cross-Section Dimensions of Box Girder Specimens

The girders were 69 feet - 11 inches long, with 2 foot - 2 inch solid end blocks and two intermittent 1 foot solid blockouts. A plan view of half of one girder is shown in Figure 2.2. An overall view of one of the box girders being moved into the laboratory is shown in Figure 2.3.

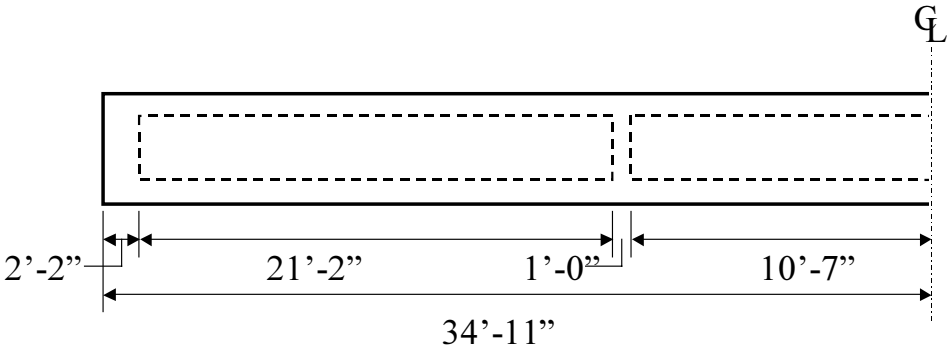

Figure 2.2 – Plan View of Box Girder

Figure 2.3 – Overall View of Box Girder

The four girders were chosen to cover a wide range of damage, as determined by visual inspection. One girder with very little damage (BG1) was picked as a control; another girder with very bad end damage (BG2) was chosen as a worst case. The remaining two girders (BG3 and BG4) have intermediate damage distributed along the length. Typical end conditions from the girders with intermediate damage are shown in Figure 2.4.

Figure 2.4 – Typical End Conditions of Girders with Intermediate Damage

The control specimen, BG1, and the most deteriorated specimen, BG2, were tested in flexure; one of the remaining halves from each girder was then tested in shear. Specimens were taken from the other half for concrete strength and pullout tests after the flexure test was completed. BG3 and BG4 were left outside to monitor crack growth and for future testing. BG4 was continually wetted and dried with a soaker hose in an attempt to accelerate damage, and was then tested in flexure and shear. Table 2.1 summarizes the specimens and the tests performed on each.

Table 2.1 – Description of Tests on Box Girder Specimens

Specimen	Description	Tests Performed
BG1	Best Condition/ Control	Flexure and shear
BG2	Bad End Damage	Flexure and shear
BG3	Intermediate Damage along the length	Crack growth monitored (future fatigue test)
BG4	Intermediate Damage along the length	Continuously wetted to accelerate damage then tested in flexure and shear

2.2 DESCRIPTION OF TYPE C GIRDERS

Two concrete prestressed girders were removed and replaced from an in-service structure located on I-10 in Beaumont, Texas. These girders were located on the outside of the bridge, and therefore were exposed to the harshest weather conditions. The other girders at the site have been monitored and are showing increasing deterioration (Boenig 2000).

Dimensions of the cross section are shown in Figure 2.5. The overall dimensions of the girders are 22 inches wide, 40 inches tall and 78 and 88 feet in length. In addition, an eight-inch concrete slab was cast on top of the girder at Ferguson Lab. The slab was added to better represent the behavior that is found in the bridge. A view of one of the girders before testing is shown in Figure 2.6.

Thirty eight, ½-inch, 270 ksi, low-relaxation prestressing strands are spaced at 2-inch intervals as shown in Figure 2.5. Eight of the thirty-eight strands are draped from the position shown in the figure, which is at the end of the beam, to the same level as the bottom strands 5 feet away from the centerline. Concrete design strength was 6000 ksi, whereas the actual strength measured from cores taken after testing was closer to 10,000 ksi.

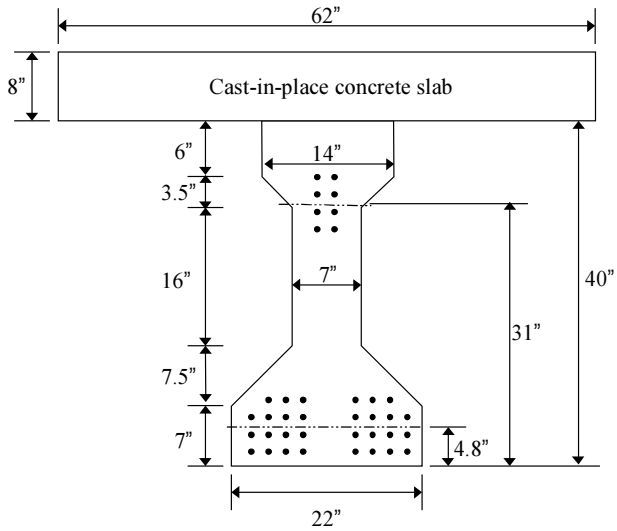

Figure 2.5 – Cross Section of the Type C Specimens

Figure 2.6 – View of Type C Girder with Slab Prior to Testing

CHAPTER 3 – VISUAL INSPECTION

As a basis for comparison, a visual inspection was carried out on all of the full-scale test specimens. Visual inspections are quick, convenient, and inexpensive and are a necessary first step. Unfortunately, they can be used to inspect only the surface, are inspector-dependent, and do not provide quantitative information. Even with these drawbacks, visual inspection is one of the most common nondestructive test methods.

3.1 INTRODUCTION TO VISUAL INSPECTION

Visual inspection is a surface inspection, with or without optical aids. Although this method is often overlooked as a nondestructive test, it can give a good indication of larger defects.

Visual inspection can use a variety of measuring devices including tape measures, calipers, crack comparators (a device with lines of specific widths to compare to crack widths), or feeler gages (metal shims of specific thickness). These devices can give good estimates of the length and width of cracks and other surface defects, as well as their position in the specimen.

In addition to measuring devices, optical aids can facilitate visual inspections. One of the more common aids are small, hand-held lenses that can improve the accuracy of crack comparators. Other aids include fiber-optic borescopes that can inspect areas with limited access, and miniature cameras that can be positioned remotely when human access is not possible (Halmshaw 1991).

3.2 APPLICATION OF VISUAL INSPECTION TO CONCRETE

In concrete specimens, visual inspection normally consists of the documentation of visual cracks and spalled concrete. Areas of concern are inspected and sketched to scale. Crack widths are measured so that changes over time can be monitored. Stains, efflorescence, or other surface indications are also noted.

From these data, it may be possible to determine how the load is affecting the specimen. For example, orientation of cracks can indicate whether the specimen is cracking under shear, flexure, or another influence such as alkali-silica reaction. Also, monitoring crack growth over time can indicate how quickly deterioration is increasing.

3.3 RESULTS OF VISUAL INSPECTION ON BOX GIRDER SECTIONS

As mentioned in Chapter 2, four prestressed box girder sections were delivered to Ferguson Laboratory for testing. Before testing, the condition of the girders was inspected visually by researchers Luz Fúnez, Anna Boenig, and Brian Tinkey. The tools used in the inspection consisted of a tape measure and a visual crack-width gage without magnification. The results are presented in this section.

The least deteriorated specimen was BG1; it serves as the control against which the other girders may be compared. Even this specimen was showing some signs of deterioration. Most of the damage was concentrated in the 26 inch long end block, with crack widths ranging from 0.002 inches to 0.06 inches. In addition, a horizontal crack at the joint between the first and second pours (5.5 inches from the bottom of the girder) ran the entire length. The final crack worth noting was a horizontal crack 17 inches from the bottom that ran intermittently along the length. Girder BG1 is shown in Figure 3.1 to Figure 3.4.

Figure 3.1 – End View of A-Side of BG1

Figure 3.2 – Side of BG1 at A-End

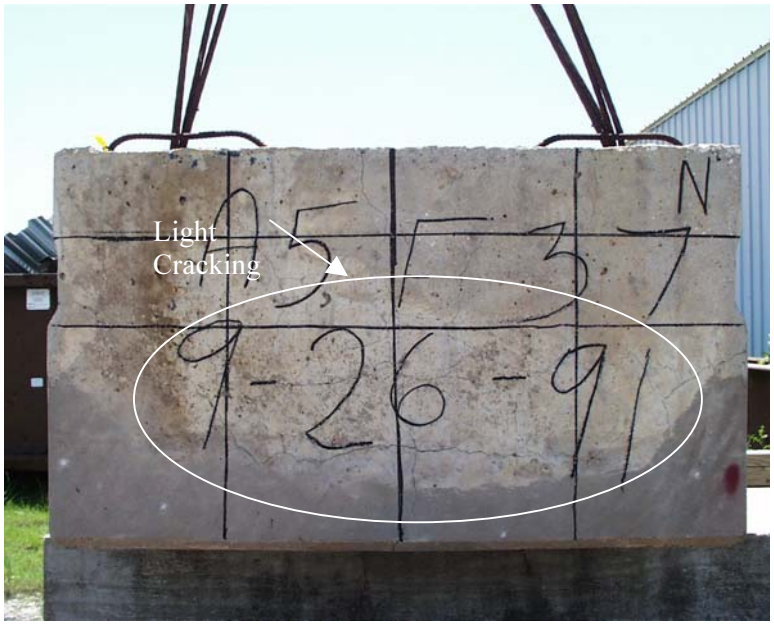

Figure 3.3 – End View of B-End of BG1

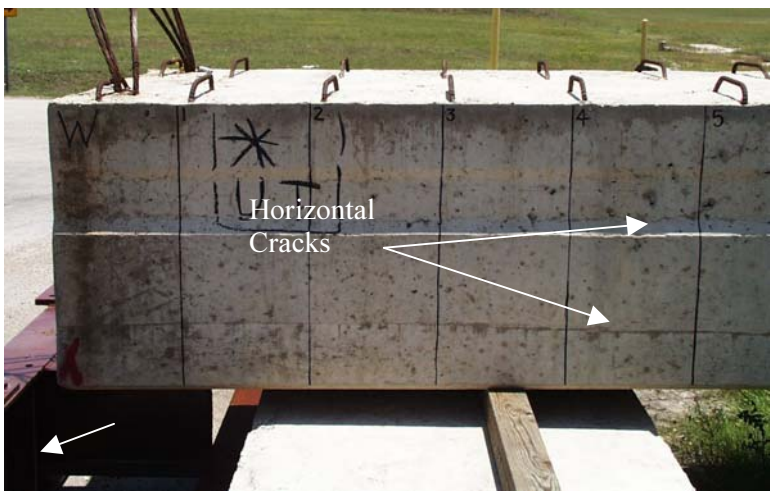

Figure 3.4 – Side View of B-Side of BG1

The specimen with the worst end damage was BG2. The ends of this specimen had cracks 10 to 20 inches long and up to 3/8 to 1/2 inch wide. In addition, at the ends some of the corners had spalled off, exposing corroded reinforcement. The horizontal cracks along the length 5.5 inches from the bottom and 17 inches from the bottom that were seen in BG1 were also seen in BG2 with a width of approximately 0.013 inches. Girder BG2 is shown in Figure 3.5 and Figure 3.6.

Figure 3.5 – Spalled Concrete on Specimen BG2

Figure 3.6 – End Damage on Specimen BG2

The third girder, BG3, was chosen because its damage, while not as severe as that of BG2, was more distributed along the length, and was also quite severe at the ends and near the interior blockouts. A crack along the pour joint had a maximum width of 0.01 inches. Figures 3.7 though 3.9 document the condition of BG3.

Figure 3.7 – End View of A-End of BG3

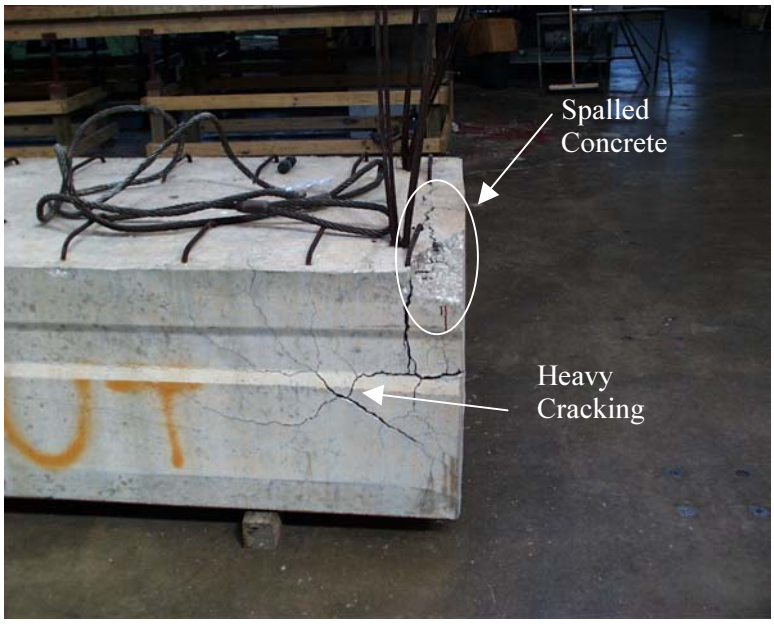

Figure 3.8 – Side View on B-End of BG3

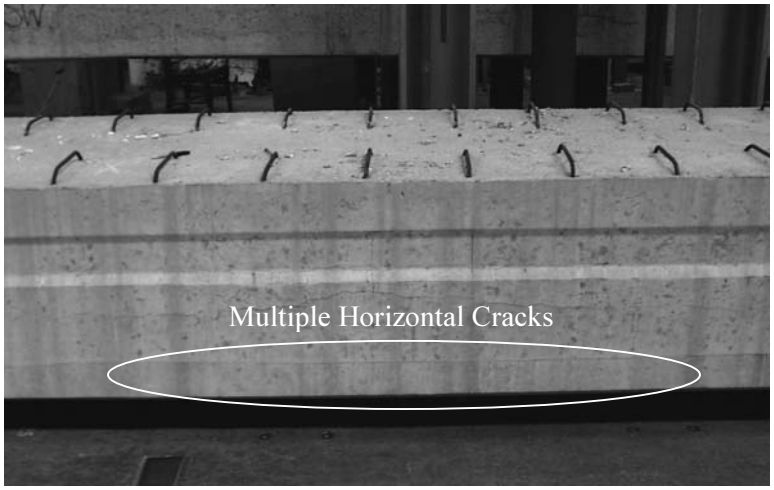

Figure 3.9 – Damage at Interior Blockout on BG3

The final specimen, BG4, was continually wetted and dried to accelerate deterioration. Its most significant damage was in the solid ends and at the solid blockouts. The crack patterns at these locations most closely resembled the ends of BG2. Efflorescence was seen at these locations. At one of the interior blockouts, water could be found leaking from the girder, indicating a full-thickness crack. Other locations along the beam had intermittent cracking with heavy staining from corroding transverse reinforcement. Figures 3.10 though 3.12 demonstrate the condition of BG4.

Figure 3.10 – Side View of A-End of BG4

Figure 3.11 – Typical Damage along the Length of BG4

Figure 3.12 – Northwest end of BG4

During the shear test of BG4, water was observed leaking out of the girder. This indicates that the bottom face of the girder had no through-thickness cracks.

3.4 RESULTS OF VISUAL INSPECTION ON TYPE C GIRDER SECTIONS

Because the two Type C girder specimens had been removed from a bridge in service, one face of each girder was painted, making visual inspection there difficult.

The same general cracking trends were noticed in these girders as in the box girders. The ends showed more deterioration, and cracks away from the end sections were oriented horizontally.

Each end of the girders was visually inspected by researcher Yong-mook Kim and rated for comparison purposes. The total area of the cracks 4 feet from the end was calculated and then divided by the total

surface area to develop a surface crack ratio. The smaller the crack ratio, the better the condition. This ratio for each end just before testing is shown in Table 3.1.

Figures 3.13 though 3.15 show the typical condition of the Type C girders.

Table 3.1 – Crack Ratios for Type C Girders

Specimen	Crack Ratio, %
Girder 1 – East End (G1ES)	1.64
Girder 1 – West End (G1WS)	1.57
Girder 2 – East End (G2ES)	0.71
Girder 2 – West end (G2WS)	1.76

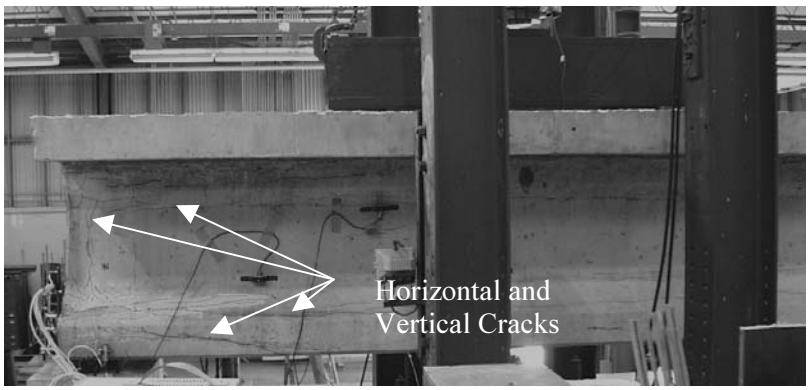

Figure 3.13 – West End of Girder 1

Figure 3.14 – East End of Girder 1

Figure 3.15 – East End of Girder 2

3.5 DISCUSSION

Results of visual inspection are difficult to quantify. One possible numerical index is the crack ratio presented in Section 3.2. Other possible indices include the sum of the lengths of the cracks multiplied by their corresponding widths, the sum of the lengths of the cracks multiplied by their widths squared, the largest crack width, or the number of cracks.

Although visual inspection is quick and easy, it has drawbacks, notably its dependence on surface condition. Bridges in service usually have some type of obstruction on the surface, making accurate visual inspection difficult. These obstructions can consist of paint, as on the Type C girders, or other substances such as efflorescence, dirt, mold, or corrosion stains.

Another problem with the method is the difficulty of acquiring accurate measurements. Crack-width readings using a crack comparator, even with magnification, are very operator-sensitive. Visual inspections of other materials often use a more consistent feeler gage, consisting of a series of flat metal sheets of different thicknesses. By inserting each sheet into the crack until the correct size is found, the crack width can be accurately and consistently determined. Unfortunately, in concrete the surface of the crack can be jagged, making it difficult to insert a feeler gage.

Finally, visual inspection is a surface method only, and cannot determine the depth of cracks or identify interior defects. Although clues such as staining and efflorescence can indicate the depth of deterioration, they are not always present at deep cracks. Finally, visual inspection is limited to areas that are easily accessible.

3.6 CONCLUSION

Visual inspection is a rapid nondestructive test method that can give an initial qualitative evaluation of damage. It is the most commonly used test method, and requires very little equipment. It is highly subjective, however, and can evaluate only surface conditions.

CHAPTER 4 – ACOUSTIC EMISSION

Acoustic emission is a passive, nondestructive test method that has been very effective for steel and fiber-reinforced plastics (Fowler 1997). It has been incorporated into many testing programs, including standard procedures developed by the Association of American Railroads (AAR IM-101), the American Society for Nondestructive Testing (ASNT-CARP 1999), the American Society for Testing and Materials (ASTM E 1316), and the American Society of Mechanical Engineers (ASME Code Section 5 Article 12). This research is directed at applying acoustic emission to concrete applications. If successful, this technology will be extremely useful in civil engineering. Some of the benefits include the fact that it is a global test (one test can investigate the entire specimen) and that it detects only structurally significant flaws.

4.1 INTRODUCTION TO ACOUSTIC EMISSION

Acoustic emission (AE) is produced when energy is suddenly released from a material under stress, due to a change of state of the material such as crack growth or dislocations. This energy release causes transient elastic stress waves to propagate throughout the specimen. These stress waves are recorded by sensitive resonant piezoelectric sensors mounted on the surface.

Acoustic emission sensors can be classified into two categories: resonant and wideband. Resonant sensors are more sensitive at certain frequencies, which depend on the internal resonant frequency of a ceramic piezoelectric crystal. Wideband sensors are manufactured similarly, but use an energy-absorbing backing material to damp out the predominant frequencies. This results in a wider frequency range but lower sensitivity. In the studies presented in this report, low-frequency resonant sensors were used, since concrete attenuates emission strongly and maximum sensitivity was required.

Traditionally, in AE testing a number of parameters are recorded from the signals, or sensor "hits;" from these parameters, the condition of the specimen is determined. Important parameters include hit arrival time, amplitude, duration, and MARSE. These parameters are defined below and shown in Figures 4.1 and 4.2. For illustrative purposes, a waveform generated by a pencil lead broken on a steel surface, captured by a wideband sensor, is used for illustration in Figures 4.1 and 4.2.

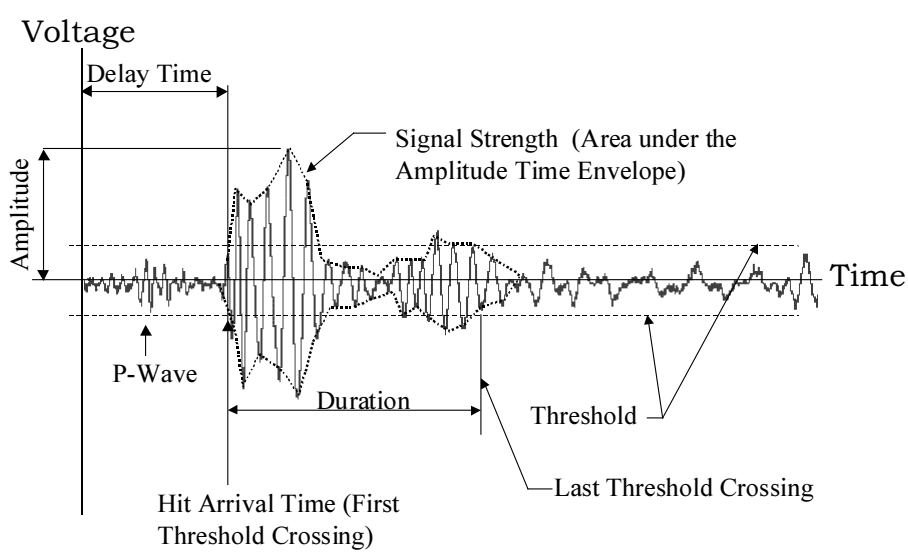

Figure 4.1 – Sample Acoustic Emission Waveform Showing Evaluation Parameters

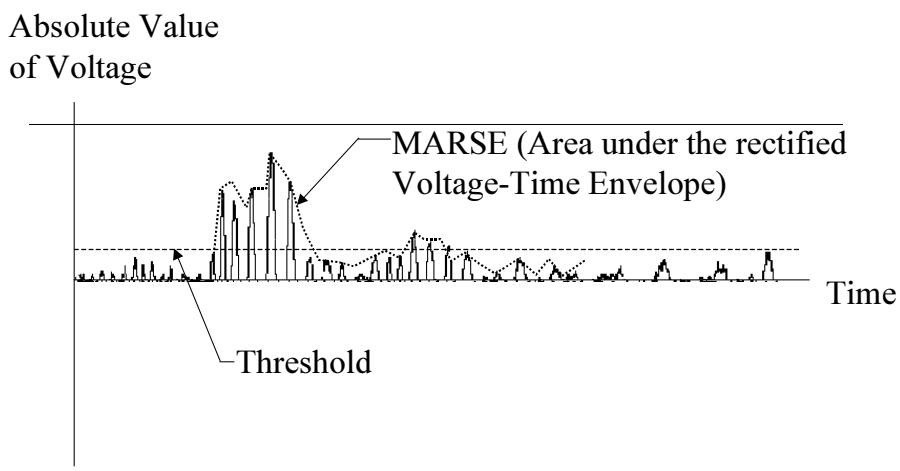

Figure 4.2 – Example of Rectified Acoustic Emission Waveform Illustrating MARSE

- **Amplitude**: The peak voltage [measured in decibels] of the largest excursion attained by the signal waveform from an emission event. (ASTM E 1316)
- **Decibel (dB):** Log scale used to measure amplitude, which is related to volts by the equation:

$$A = 20LOG\left(\frac{V}{1000}\right) \qquad \text{(Eqn. 4.1)}$$

- **Duration:** The time from the first threshold crossing to the last threshold crossing of the signal or envelope of the linear voltage time signal. (AAR IM-101)
- **MARSE**: Measured area of the rectified signal envelope. A measurement of the area under the envelope of the rectified linear voltage time signal from the sensor [for each hit]. (AAR IM-101)
- **Signal Strength:** Area under the envelope of the linear voltage time signal from the sensor. The signal strength will normally include the absolute area of both the positive and negative envelopes. (AAR IM-101)
- **Sensor Hit** (Hit): Detection and measurement of an AE signal on a channel. (AAR IM-101)
- **Voltage Threshold** (Threshold): A voltage level on an electronic comparator such that signals with absolute amplitude larger than this level will be recognized. (AAR IM-101)

4.2 APPLICATION OF ACOUSTIC EMISSION TO CONCRETE IN GENERAL

Wave propagation through a material depends on the material's damping, geometry, and elastic properties. Concrete poses a problem for wave propagation because it is heterogeneous and contains microcracks. Its constituents such as hydrated cement and aggregate vary significantly in size and material properties. In addition, its properties can vary due to uneven consolidation, differential shrinkage, or bleed water. This nonhomogeneity causes considerable scatter in results for practically any test performed on concrete, including acoustic emission. This section covers some of the research done on reducing these effects.

4.2.1 Difficulties with Acoustic Emission in Concrete

Due to its heterogeneity and microcracks, concrete attenuates the acoustic emission more quickly than steel or fiber-reinforced plastics. Figure 4.3 shows an example of how amplitude is reduced as a function of the distance between a pulser and a transducer in plain concrete specimens (Uomoto 1987). To look at

attenuation only, a pulse generator sent a pulse through the concrete and a 140 kHz resonant transducer then measured the resulting amplitude. The results show an amplitude reduction of approximately 100 dB/m. Since background noise is generally picked up around 30dB, the range of AE monitoring for this sensor is limited to 20 to 30 cm.

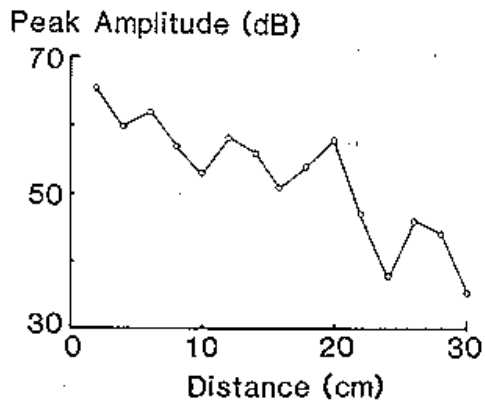

Figure 4.3 – Example of Attenuation in Concrete (Uomoto 1987)

AE signals in concrete are also attenuated by cracks. To study this, peak amplitudes were recorded with respect to stress level in concrete during flexure and compression tests (Uomoto 1987). Flexure tests were conducted on small reinforced concrete beams, while the compression tests were conducted on cylinders. A pulse was then sent longitudinally along the specimen and the peak amplitudes were recorded. The distance between the pulser and the transducer was similar for both tests. The results of those tests are summarized in Figure 4.4. Flexural cracks cause considerable attenuation, while compressive cracks have only a minor effect. The author suggested that this is because the flexural cracks are orientated perpendicular to the direction of wave travel, while cracks formed in compression are orientated parallel to the direction of travel. The effect of flexural cracking on the propagation of acoustic emission was also demonstrated at The University of Texas at Austin during tests on a concrete frame (Barnes and Fowler 1998).

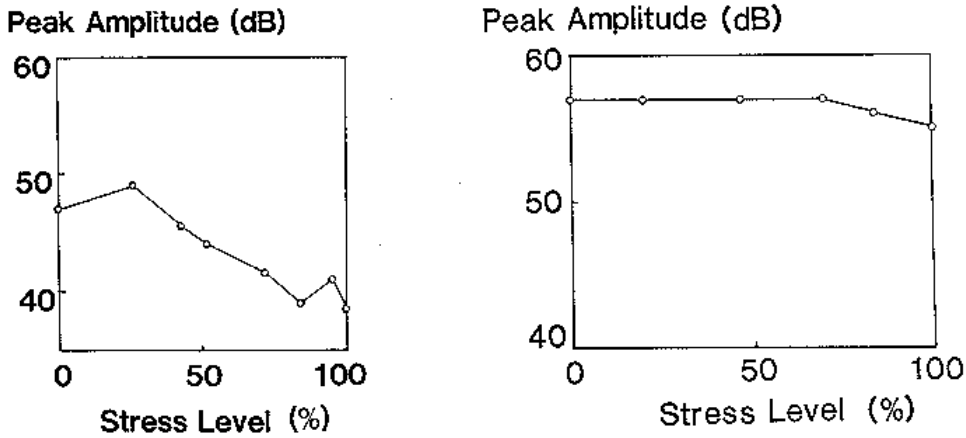

Cracks Perpendicular to Direction of Travel

Cracks Parallel to Direction of Travel

Figure 4.4 – Typical Graphs Showing Attenuation of Acoustic Emission in Concrete (Uomoto 1987)

A few methods have been proposed to minimize the effects of attenuation (Uomoto 1987). Due to dispersion, higher frequencies attenuate more quickly than lower frequencies (Bray and Stanley 1997), and therefore one of the accepted methods is to use a lower-frequency sensor. In a field test of corroded beams (Kamada et al 1996), 150 kHz sensors and 60 kHz sensors were used to monitor a structure, and the only usable data came from the 60 kHz sensors. Another method is to attach the sensors to the reinforcement instead of the concrete. Since steel is more homogenous than concrete, the acoustic emission has less attenuation.

Micro-cracking in reinforced concrete, while normal and usually not structurally significant, creates a large amount of acoustic emission. This may interfere with emission from a defect, complicating acoustic emission testing in reinforced concrete. Also, if flexural cracks lie between the acoustic emission source and the sensor, the signal may be greatly attenuated or even blocked. Even with these difficulties, acoustic emission has been applied to concrete with promising results (Barnes and Fowler 1998). Research has shown that as damage increases the rate of emission and event amplitude increase (Karabinis and Fowler 1983).

Prestressed concrete, in contrast, is usually designed not to crack; any cracking and associated emission are significant. Also, the attenuating effect of cracks on wave propagation is eliminated. These factors combine to create an ideal environment for acoustic emission (Yepez 1997).

4.2.2 Kaiser Effect

The Kaiser Effect is one of the more-studied acoustic emission phenomena in concrete. The American Society of Testing and Materials (ASTM) defines it as follows:

Kaiser Effect – *the absence of detectable acoustic emission at a fixed sensitivity level [threshold], until previously applied stress levels are exceeded. (ASTM E 1316)*

The most obvious application of the Kaiser Effect is to determine the maximum prior stress in a structure. This application has been debated, though, since some research shows that in concrete the Kaiser Effect is only temporary (Nielsen and Griffen 1977). After a long period of time, the beam can "heal" itself so that it will produce acoustic emission on subsequent loading at levels lower than previously applied. Other researchers report that the maximum prior stress can be determined from of rate of emission and rate of signal strength, or total events vs. load plots (Uomoto 1987). Even those researchers concede that there are limitations such as the prior stress must be below a critical level, and that most of the cement hydration must be completed to be valid.

Of more significance for structural evaluation is when the Kaiser Effect starts to break down. It has been found that the Kaiser Effect starts to break down as flexural crack widths increase and shear cracks start to play a role (Yuyama et al. 1996). This effect, called the Felicity Effect, shows great promise for evaluation because it is only apparent when there is damage to the specimen, and is greater when the damage is worse. This effect is defined by ASTM as:

Felicity Effect – *the presence of acoustic emission, detectable at a fixed predetermined sensitivity level [threshold] at stress levels below those previously applied. (ASTM E 1316)*

Studies have shown that the Felicity Effect starts to appear when crack widths are greater than 0.15 to 0.20 mm or when delaminations are present (Yuyama et al. 1996). An evaluation criterion, the Felicity ratio, has been proposed to quantify the degree of deterioration. This ratio is defined as the stress at the onset of AE divided by the maximum prior stress and a Felicity ratio less than unity indicates damage (Yuyama et al. 1994).

One study showed this effect in concrete with corroding reinforcement (Yuyama and Murakami 1996). Flexure specimens were immersed in a sodium chloride solution until cracks 1 mm and 4 mm wide were caused by corrosion of the reinforcement. The specimens were then tested under four-point bending, and were monitored for AE. The Felicity ratios for the second and third loading are shown in Table 4.1. The

first loading is not shown because the Felicity ratio is only defined on reloads. It can be seen that as the damage increases, the Felicity ratio decreases.

Table 4.1 – Felicity Ratios for the Second and Third Loading (Yuyama and Murakami 1996)

	Loading Cycle	
Specimen Description	2	3
No Damage	1.00	0.75
Crack width 1 mm	0.71	0.49
Crack width 4 mm	0.28	0.10

The Felicity ratio has also proven useful in determining the adequacy of repaired concrete beams (Yuyama et al 1994). The Kaiser Effect and the Felicity Effect are illustrated in detail in Section 4.4.

4.2.3 Rate Process Analysis

Rate process analysis is based on the theory that while sound concrete does not produce significant emission at low stress, concrete with significant microcracking will produce considerable emission (Ohtsu 1990). Concrete in poor condition will produce acoustic emission at low loads due to existing critical microcracks growing, while concrete in good condition does not produce acoustic emission until just prior to failure. Although rate process analysis is not used in this report, it is summarized here for informational purposes.

Rate process theory suggests that the number of AE events can be related to the stress level by the equation:

$$N=CV^{a}\exp(bV)$$

Where **N** is the number of AE events, **V** is the stress level in percent of ultimate, and **a, b,** and **C** are empirical constants determined from a least-squares fit (Ohtsu 1988). After the curve is fitted, the condition of the concrete can then be determined by the constant **a**. It can be shown that a positive value indicates significant emission at low loads, while a negative **a** value relates sound concrete that produces little emission at low loads.

Tests on concrete cores have shown that the extent of microcracking may be more accurately determined from rate process analysis of acoustic emission data than from visual examination of the crack density (Ohtsu et al 1988). It has also been shown that rate process analysis is in agreement with the ultrasonic technique of nondestructive testing (Ohtsu 1990).

4.2.4 Moment Tensor Analysis

Although the results from the Kaiser Effect and rate process analysis show promise for determining structural integrity, more quantitative information would be beneficial. The advantage of moment tensor analysis lies in its ability to indicate source location, crack classification, and direction of crack propagation.

Moment tensor analysis is based on the change in stress geometry that occurs at the source of the acoustic emission. To develop this analysis, crack motion is described by a set of linear equations with 6 unknowns, corresponding to the elements in the 3-dimensional moment tensor. An eigenvalue decomposition is then performed, from which crack type and crack propagation data are found. More specifically, eigenvalues have been found to relate to the type of crack – shear, tensile, or mixed.

Physically, the values represent the direction of the dislocation displacement vector in relation to the crack normal vector. If the dislocation displacement vector is perpendicular to the crack normal vector (that is, in the direction of the crack), the crack is a shear crack. If the dislocation displacement vector is parallel to the crack normal vector (that is, perpendicular to the crack) the crack is classified as a tensile crack. Since cracks are rarely entirely shear or tensile, results are reported as percent shear. The direction of crack propagation can be found through the eigenvectors.

The major problem with moment tensor analysis is that 6 clear P-waves need to be recorded for the same event. During one study, 1024 sets of waveforms were recorded and only 19 sets were found to be usable (Yuyama et al 1995). Other studies confirm that most recorded data are not usable for analysis (Yepez 1997).

Despite the fact that most data cannot be used, moment tensor analysis shows great promise, because it allows cracks to be identified before they are detected visually. In Figure 4.5 are shown the results of moment tensor analysis conducted at The University of Texas at Austin on a Type I prestressed girder under flexural loading (Yepez 1997). The cracks correspond well to the moment tensor results from the previous loading.

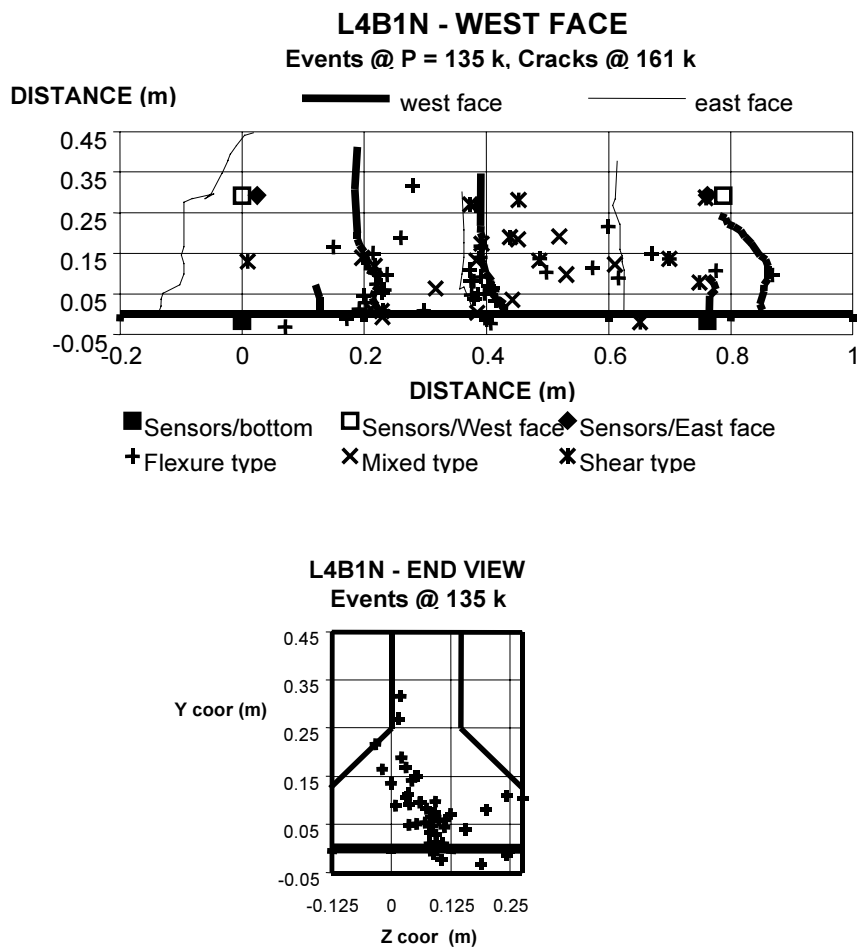

Figure 4.5 – Moment Tensor Results on Prestressed Girder (Yepez 1997)

4.3 ACOUSTIC EMISSION RESPONSE OF FLEXURAL CRACKING IN UNREINFORCED CONCRETE

The acoustic emission testing completed for this report can be divided into two parts. The first part involves understanding the AE response of plain concrete as it cracks; the second part involves applying that understanding to full-scale specimens. This section describes the behavior of the plain concrete specimens.

4.3.1 Test Setup

To study the acoustic emission behavior associated with flexural cracking in unreinforced concrete, acoustic emission was monitored during testing of a standard notched beam (RILEM 1989). John Heffington, Brent Wenger, and Brian Tinkey performed these tests at the Ferguson Laboratory. The test is conducted on both notched and notch-free unreinforced concrete beams that are simply supported and have a concentrated load at midspan. In addition to acoustic emission monitoring, a clip gauge was placed at the notch tip to monitor widening during loading, and a load cell was placed under the ram to record the load. The test setup is shown in Figure 4.6.

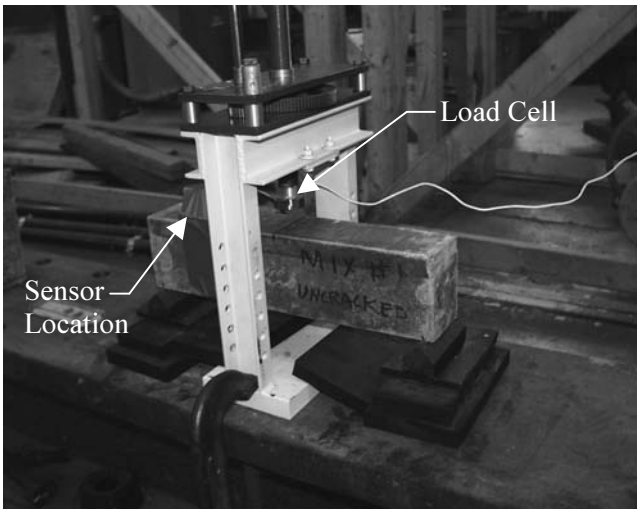

Figure 4.6 – Experimental Setup Used for Plain Concrete Tests

Three different mixture designs were cast, two lightweight and one normal-weight. Mechanical properties of the mixtures as well as their failure loads are shown in Table 4.2. Mixture 1 used lightweight coarse aggregate. This mixture achieved the highest compressive strength of the three mixtures used in these tests, an expected result due to its high cement content and low water-cement ratio. Mixture 2 also used lightweight coarse aggregate. The cement content in this mix was decreased while the water-cement ratio was increased, to produce lower compressive and tensile strengths. During the casting of the beams and cylinders with Mixture 2, the paste segregated from the aggregate due to the high slump. This segregation, however, did not seem to decrease the strengths. Mixture 3 used normal-weight river gravel as the coarse aggregate, and was a control mixture against which Mixtures 1 and 2 could be compared. Using each of the mixture designs, two beams were cast with an initial notch and one was left without any initial notch, for a total of three beams for each mixture.

Table 4.2 – Properties of Mixtures Used on Plain Concrete Specimens

Concrete Mix	Average Comp. Strength (psi)	Average Split Tensile Strength (psi)	Notch free Max Load (lbs.)	Notched Max. Load (lbs.)
1	8114	520	1542	473
2	4191	424	1214	399
3	6750	543	1468	596

Dimensions of the specimens deviated slightly from the RILEM standard due to the availability of molds. The nominal dimensions of the specimens were 3 inches wide, 4 inches deep and 16 inches long. An initial notch approximately one-half inch deep was induced into the center of some of the specimens by placing a steel shim in the mold during casting. The specimens are shown schematically in Figure 4.7.

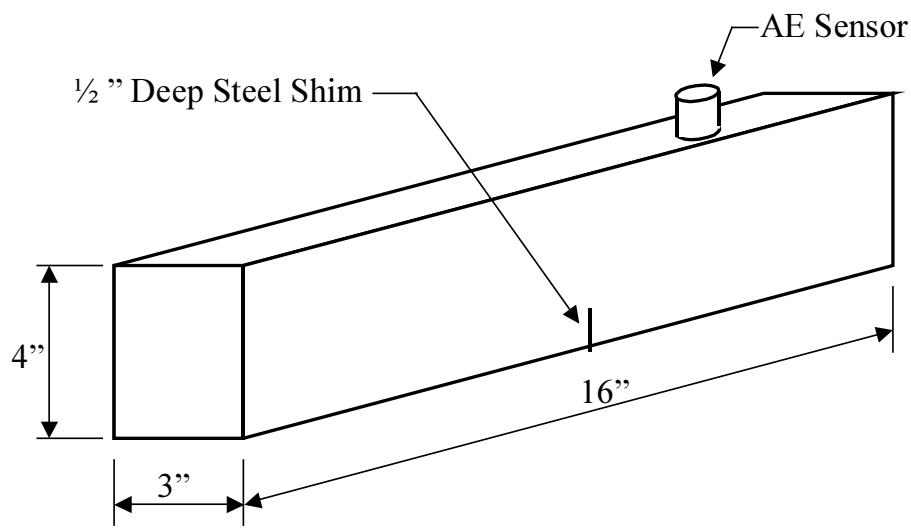

Figure 4.7 – Dimensions of plain concrete specimens

Data were collected using a Locan 320 data acquisition instrument and 60 kHz resonant sensors with internal preamplifiers (R6I) from Physical Acoustics. Specific information, including hit definition time, hardware filters, sensor preamplifier, and voltage thresholds is summarized in Table 4.3.

Table 4.3 – Test Parameters for Unreinforced Concrete Specimens

Quantity	Values
Hit Definition Time (HDT)	1000 μs
Voltage Threshold	45 dB
Sensor Preamplifier (R6I)	40 dB
Data Acquisition Preamplifier	20 dB
Bandpass Data Acquisition Filter	0-1000 kHz
Bandpass Sensor Filter	30-165 kHz

4.3.2 Analysis and Results

From examining the data, it appeared that the most useful parameter for analysis was cumulative MARSE. As outlined previously, MARSE is the area under the rectified amplitude vs. time envelope for each hit. Cumulative MARSE is the sum of the MARSE from all prior hits. Traditionally, an increase in the slope of a graph of cumulative MARSE vs. time indicates a significant change in state in the specimen (ASNT – CARP 1999). For example, in steel an increase in slope may indicate yielding, while in reinforced concrete a slope increase could indicate a new shear or flexure crack.

The cumulative MARSE plot of a representative notched specimen just prior to fracture is shown in Figure 4.8. This chart shows two distinct slope changes, or "knees," that indicate a significant change in the specimen. The first knee coincides with the first opening of the notch, corroborated by the clip gauge and a metallic sound heard at that time. The combination of these events indicates that the slope increase is most likely due to debonding of the steel shim used for the notch initiation. After the crack opened, no further damage occurred as shown by the flat slope of cumulative MARSE. Knee 2 occurs immediately before the final fracture. From the acoustic emission while loading, it was possible to predict imminent failure from the increased rate of emission.

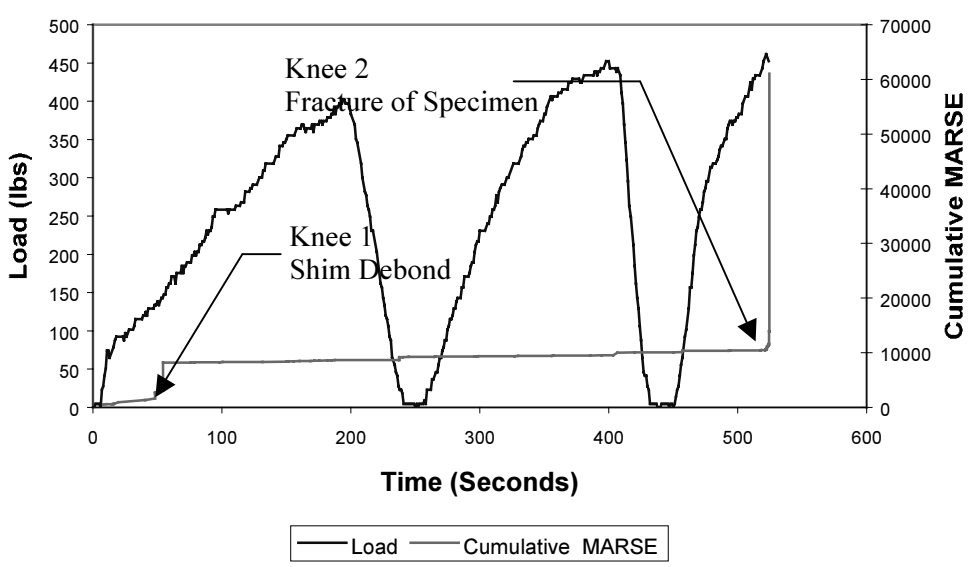

Figure 4.8 – AE Response of a Typical Notched Specimen

To more accurately identify knees in the curve of cumulative MARSE, an analysis tool called Historic Index has been developed. This tool was developed for testing pressure vessels and is currently incorporated into the MONPAC-PLUS (Fowler et al. 1989) standard for testing metal tanks and vessels. In essence, Historic Index compares the average MARSE of the last few hits with the average MARSE of all hits up to that point. The equation for Historic Index as outlined in the MONPAC-PLUS procedure is shown below:

$$H(t) = \frac{N}{N-K}\left(\frac{\sum_{t=K+1}^{N} S_{ot}}{\sum_{i=1}^{N} S_{oi}}\right) \qquad \text{(Eqn. 4.2)}$$

where N is the current number of hits, S_{oi} is the MARSE of a particular hit, and K is defined by the table below.

Table 4.4 – K values used in Historic Index (Fowler et al. 1989)

Number of Hits	K
<10	Not Applicable
10-15	0
16-75	N-15
76 to 1000	0.8N
>1000	N-200

In this study, the Historic Index was calculated using a program written in C++ and then plotted in a program written in LabView. Figure 4.9 shows the Historic Index for the small-scale specimen whose cumulative MARSE plot is shown in Figure 4.8. The knees in the MARSE curve can readily be identified because they correspond to sharp increases in the Historic Index plot. The first peak in Figure 4.9 lasts for a long time, since Historic Index is independent of time and is only updated when a new hit occurs. After the shim had fully debonded, very few new hits occurred, resulting in a long plateau.

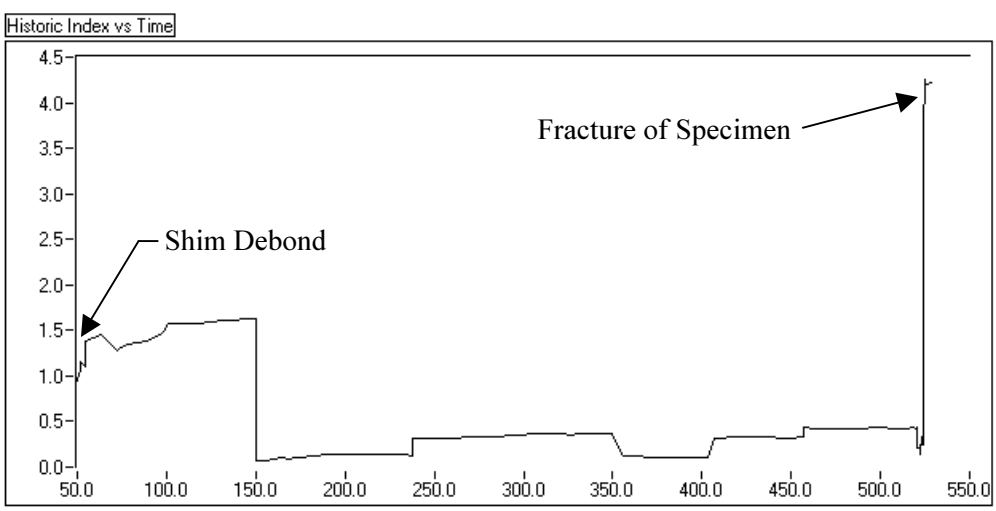

Figure 4.9 – Historic Index for a Typical Prenotched Specimen

While the notched specimens displayed little acoustic emission except at the knees in the cumulative MARSE curve, the notch-free specimens (Figure 4.10) showed relatively constant low-level emission until just prior to failure, when the rate of emission increased significantly. A probable explanation for the difference in trends between the notched and the notch-free specimens can be explained by crack initiation. Cracks form in concrete when distributed microcracks coalesce into a single crack. The notched specimens have a significant stress concentration, focusing the microcracking to a small area. If the microcracking occurs only in a small area, less microcracking will occur before a crack forms. Because acoustic emission detects the stress waves emitted from the microcracking, a notched specimen will have less emission. Another explanation is that the notched specimen fails at a much lower load than the notch-free specimens. The higher loads produce a higher stress, which causes more microcracking and more emission.

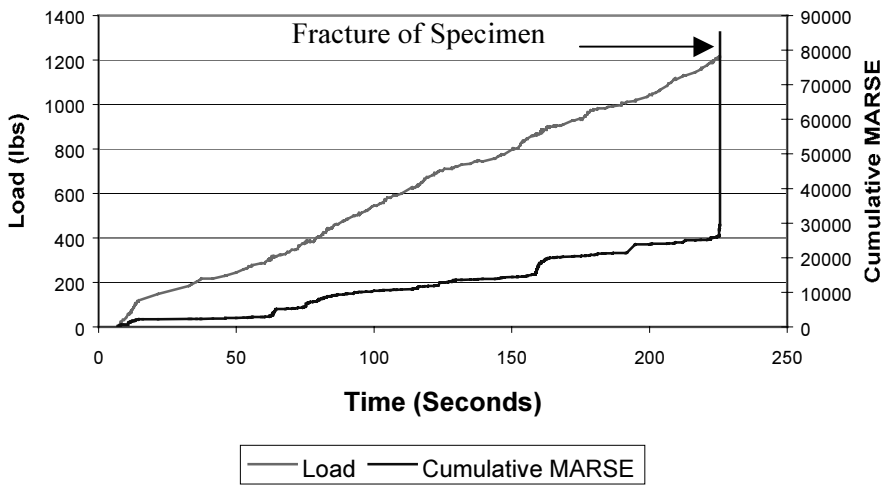

Figure 4.10 – Typical AE Response of Notch Free Specimen

As with the notched specimens, the Historic Index of the notch-free specimens is a good indicator of significant events. Figure 4.11 shows the Historic Index for the specimen whose cumulative MARSE plot is shown in Figure 4.10. The only large, sharp jump in this graph corresponds to fracture of the specimen. The Historic Index for the notch-free specimen has more scatter than that of the notched specimen.

At the beginning of the notched specimen's test, large MARSE hits were received, creating a high cumulative MARSE. Since Historic Index compares the MARSE of the last few hits with that of all hits up to that point, hits with much higher MARSE are required to create a jump with the notched specimen than with the notch-free specimen. The Historic Index for notched specimen is about 0.4 when no significant event is occurring, instead of the corresponding value of 1.0 for the notch-free specimen.

4.3.3 Discussion

The major source of acoustic emission for these small-scale, unreinforced specimens was from microcracking and cracking of concrete. Other mechanisms, such as steel yielding or debonding, were not present in these unreinforced specimens. Once one major crack develops, an unreinforced specimen fails. More acoustic emission is evident from notch-free specimens before failure, because microcracking is distributed, rather than concentrated in a particular area as with the notched specimens. Significant events identified directly by a large increase in the cumulative MARSE plot, or indirectly from the Historic Index.

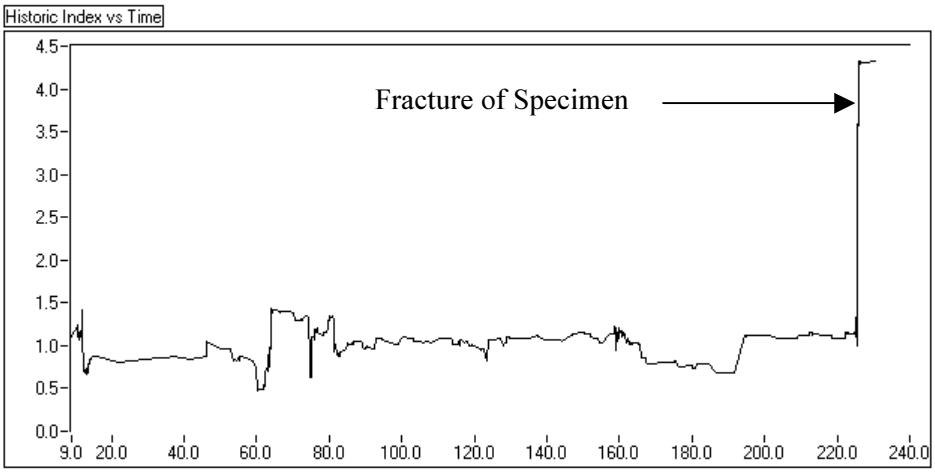

Figure 4.11 – Historic Index for a Typical Notch free Specimen

4.4 AE RESPONSE OF FULL-SCALE PRESTRESSED BOX GIRDERS IN FLEXURE

Acoustic emission monitoring was performed on prestressed concrete girders during ten tests of box sections and Type C sections under both shear and flexure. All specimens were experiencing varying degrees of damage from a combination of delayed ettringite formation (DEF) and alkali-silica reaction (ASR).

4.4.1 Setup of Flexure-Dominated Box Girder Tests

BG1, BG2, and BG4 were tested in flexure under four-point loading at Ferguson Laboratory. Specimens were supported on bearing pads to duplicate field conditions and isolate the specimen from external acoustic emission. Steel beams were used to distribute the load from the testing machine head to four points on the webs to avoid a punching shear failure though the top wall. Details of the spreader beams are shown in Figure 4.12. These beams rested on rollers, which in turn were connected to the girder with hydrostone (gypsum plaster). The hydrostone was used to provide a smooth surface to support the rollers. By compressing a thin layer of hydrostone and monitoring any resulting acoustic emission, it was found that no acoustic emission was released by the hydrostone up to loads greater than those expected during the test. Also, in an effort to isolate the beam from external noise sources, bearing pads were placed between the longitudinal and transverse spreader beams. An overall view of BG1 just prior to testing is shown in Figure 4.13.

The loading schedule for the specimens was developed so that the Kaiser and Felicity Effects could be studied. Load was increased in 10-kip increments and held at the higher value until the rate of acoustic emission decreased. The load was then decreased to 5 kips and held there for approximately 4 minutes. This cycle was then repeated until failure. The actual loading schedule for BG1 while acoustic emission was being monitored is shown in Figure 4.14. Notice there is a slight unintentional drop in load, due to relaxation of the specimen.

The expected flexure area was bracketed on both sides with six 60 kHz resonant sensors (R6I). Sensor spacing was based on an attenuation test performed on the web of a prestressed girder. This test was performed by breaking a 0.3mm Pentel 2H pencil leads on the concrete every 6 inches away from an R6I sensor for a total of 10 feet. Amplitudes of the resulting hits were then plotted to generate the attenuation curve of Figure 4.15. From the results in Figure 4.15, it can be seen that in 10 feet there was a loss of 40 dB. The attenuation in this test is much lower than that shown in Section 4.2 since prestressed concrete was tested and a sensor with a lower resonant frequency was used. As explained in Section

4.2.1, prestressed concrete does not have the nonstructural cracking that may be found in reinforced concrete, and lower frequencies attenuate less than higher ones, both leading to a more favorable attenuation curve. A six-foot spacing of sensors was chosen, with sensors placed alternately on opposite sides of the beam (Figure 4.16).

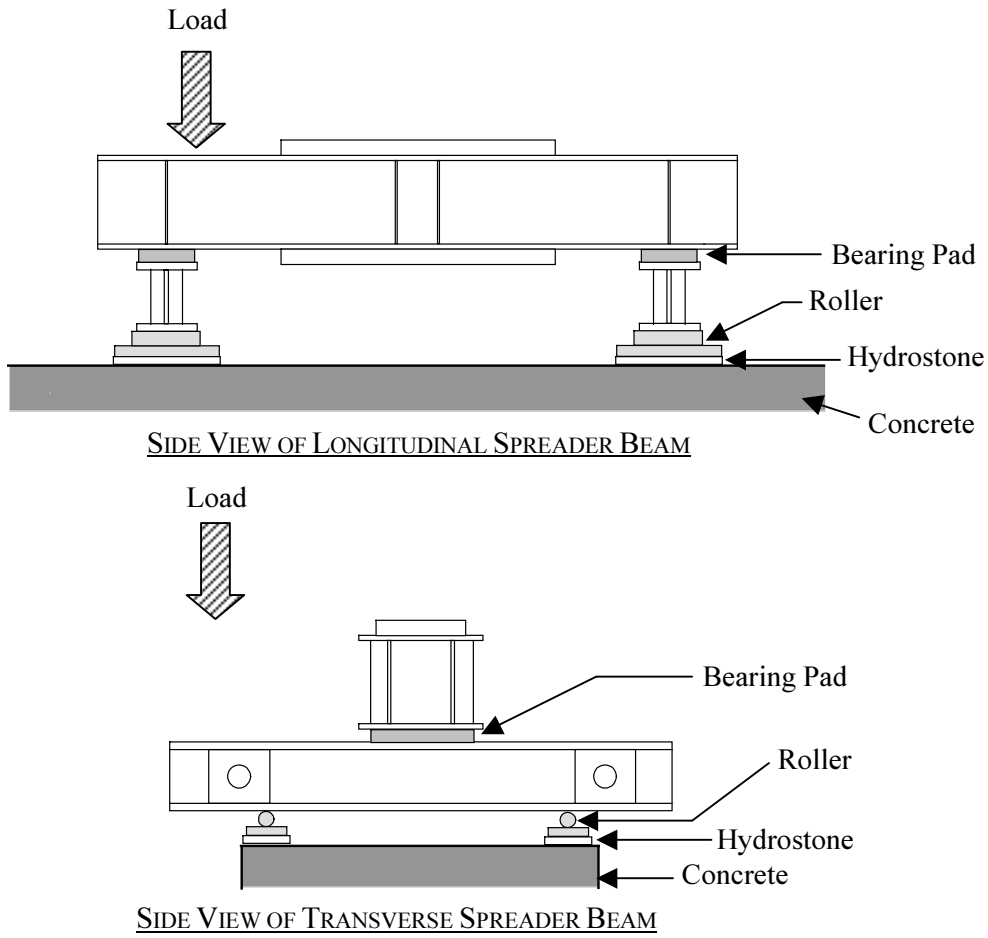

Figure 4.12 – Detail of Spreader Beams used in Flexure Tests

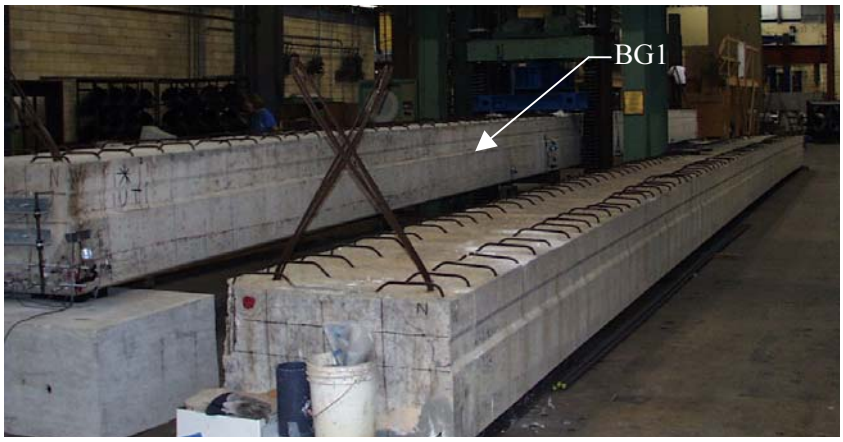

Figure 4.13 – BG1 Prior to Testing

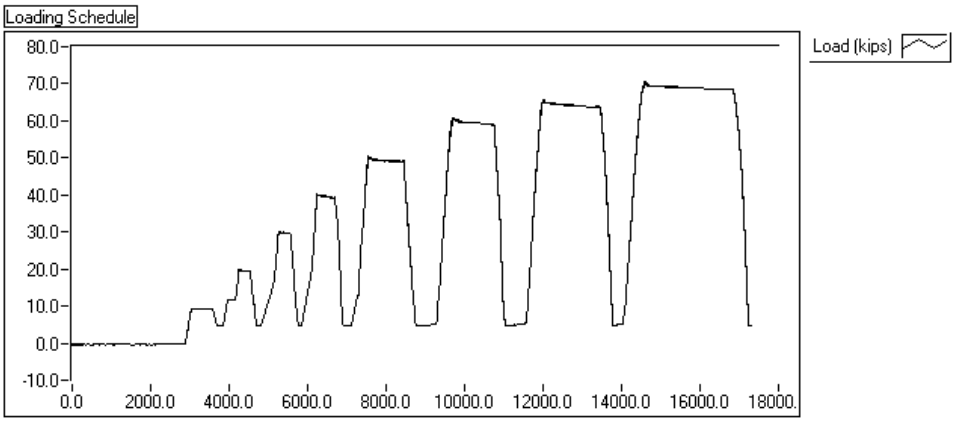

Figure 4.14 – Loading Schedule for BG1

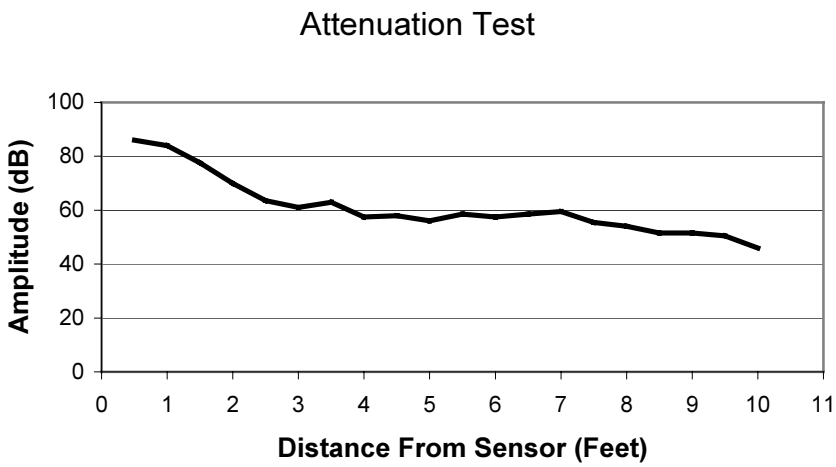

Figure 4.15 – Attenuation Curve for R6I Sensor

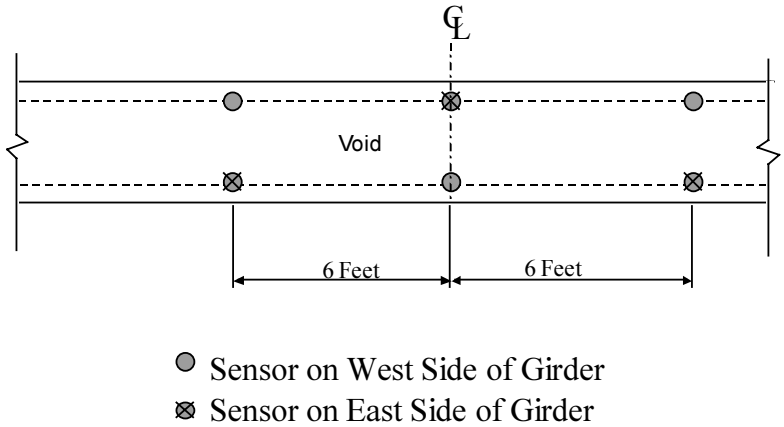

Figure 4.16 – Plan View of Sensor Locations on Box Girder Specimens

A digital MISTRAS 2001 instrument was used with 60 kHz resonant sensors (R6I) with internal preamplifiers from Physical Acoustics. Specific information, including hit-definition time, hardware filters, sensor preamplifier, and voltage thresholds for the full-scale tests is summarized in Table 4.5.

Table 4.5 – Test Parameters for Full-Scale Tests

Quantity	Values
Hit Definition Time (HDT)	800 μs
Voltage Threshold	45 dB
Sensor Preamplifier (R6I)	40 dB
Data Acquisition Preamplifier	0 dB
Bandpass Data Acquisition Filter	20-400kHz
Bandpass Sensor Filter	30-165 kHz

Data were analyzed using programs written by the author in C++ and LabView.

4.4.2 Results of Flexure-Dominated Tests on Box Girders

Significant differences in acoustic emission response can be seen between the box girder specimens. Four different parameters show promise for a nondestructive evaluation: Felicity Effect; amount of emission; emission during load holds; and amplitudes.

4.4.2.1 BG1

Figure 4.17 is the graph of cumulative MARSE vs. load until cracking for BG1, the least damaged of the specimens tested. The Kaiser Effect holds true at all load increments up to cracking. This is shown by the fact that a graph of cumulative MARSE vs. load graph is horizontal until the previous maximum load is reached. Very little emission occurs during load holds, before cracking, or during unloading.

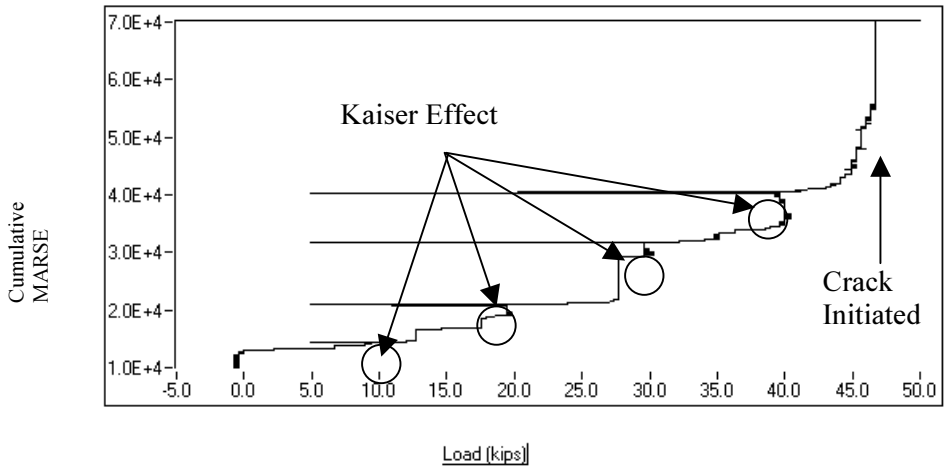

Figure 4.17 – Load vs. Cumulative MARSE before Cracking for BG1

To determine the Felicity Ratio, the load at the point where the cumulative MARSE was 300 higher than when it passed 8 kips on reloading was compared to the maximum previous load. A MARSE value of 300 was chosen because it is large enough that a few random hits would not be significant emission. A value of 8 kips was chosen since it is above all of the unloads, but still small enough to produce very little emission. Felicity ratios for BG1 are presented in Table 4.6.

Table 4.6 – Felicity Ratios for BG1

Previous Load (kips)	Emission on Reload (kips)	Felicity Ratio/CBI	
9.8	12.34	1.2	
20	25.48	1.0	
30	33.88	1.0	
39.4	40.45	1.0	First Crack Detected
50	37.16	0.9	
60	26.94	0.7	
65	30.59	0.7	

Another way of analyzing the data was to look at the Historic Index and amplitude of the hits over time. Since the amount of acoustic emission in concrete is much greater than that in steel, the K values in the definition of Historic Index in Section 4.3 were modified for the full-scale tests. The values chosen for K are similar to those used for fiber-reinforced plastics, and are shown in Table 4.7. These values give higher peaks and less scatter that the values presented in Section 4.3. Figure 4.18 shows the plots of Historic Index vs. time, amplitude vs. time, and load vs. time for BG1. These plots for BG1 do not include Channel 3, which had a wiring short and as a result gave bad data.

Table 4.7 – Values for K used in Calculating Historic Index

Number of Hits	K
<100	0
100-500	0.8N
>500	N-100

The plot of Historic Index vs. time (Figure 4.18) shows one peak at cracking, and a few smaller peaks before cracking. All of these peaks are small (less than 5), and the results show significant scatter.

The amplitude vs. time plot (Figure 4.18) shows very few high amplitude hits until cracking. In fact, there is only one hit above 90 dB before cracking.

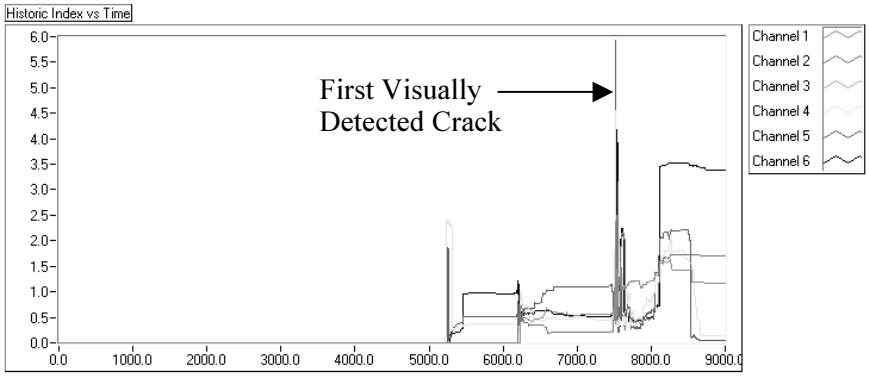

a) Historic Index Vs Time for BG1

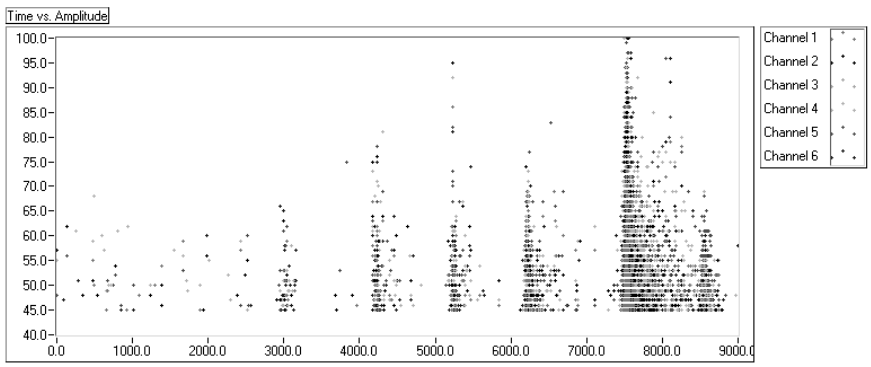

b) Amplitude vs Time for BG1

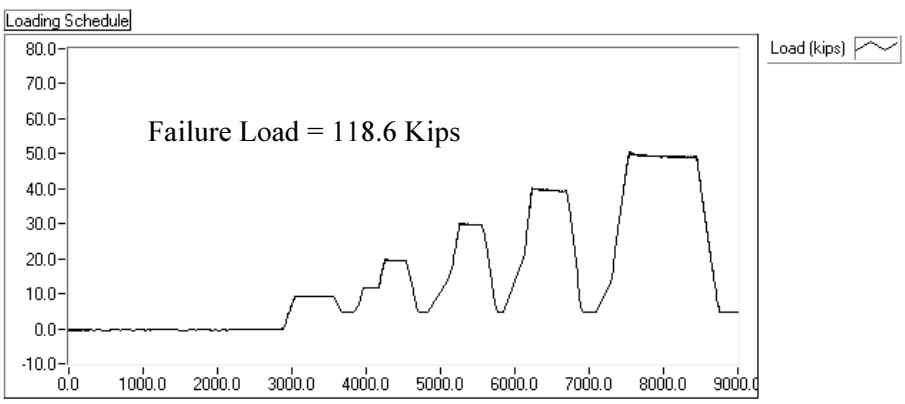

c) Load vs Time for BG1

Figure 4.18 – Time Based Graphs for BG1

4.4.2.2 BG2

Figure 4.19 is the graph of cumulative MARSE vs. load for BG2, the most damaged of the specimens tested. The Kaiser Effect does not hold for this specimen. Instead, the Felicity Effect is detected very early as seen by the separation in the unloading and reloading lines marked by "X" in Figure 4.19. The point where the Felicity Effect begins, as defined in Section 4.4.2.1, is drawn in Figure 4.19 and presented in Table 4.8. Significant emission occurs during load holds, as shown by the fact that cumulative

MARSE increases at a relatively constant load (a vertical increase in Figure 4.19). Total emission is quite large as can be seen by the scale of the vertical axis.

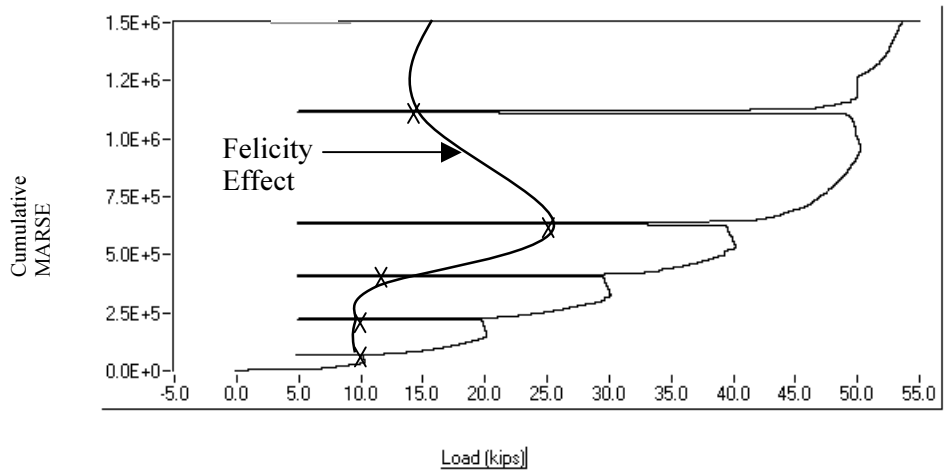

Figure 4.19 – Cumulative MARSE vs, Load for BG2

Table 4.8 – Felicity Ratios for BG2

Previous Load (kips)	Emission on Reload (kips)	Felicity Ratio/CBI	
10	9.88	1.0	
20	10.61	0.5	
30	12.44	0.4	
40	25.26	0.6	First Crack Detected
50	13.07	0.3	
60	24.45	0.4	

Graphs of amplitude vs. time and Historic Index vs. time for BG2 are shown in Figure 4.20. The only major peak in the Historic Index corresponds to the cracking load. At lower loads, there is little scatter and the Historic Index stays close to 1.0. Also, high amplitude hits occurred in every loading cycle.

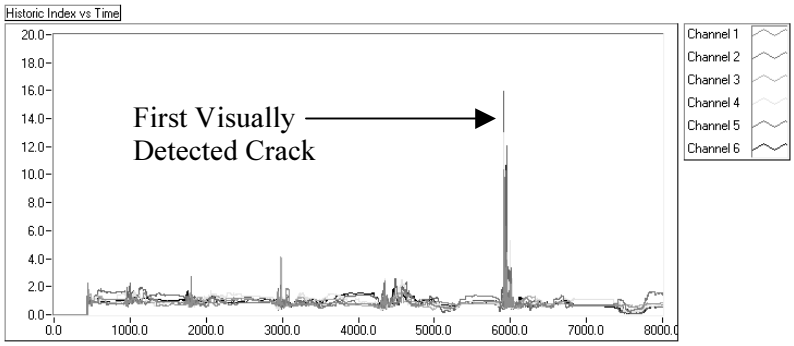

a) Historic Index vs Time for BG2

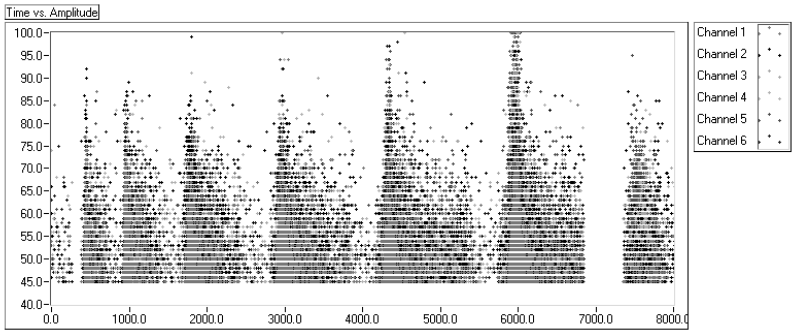

b)Amplidue vs Time for BG2

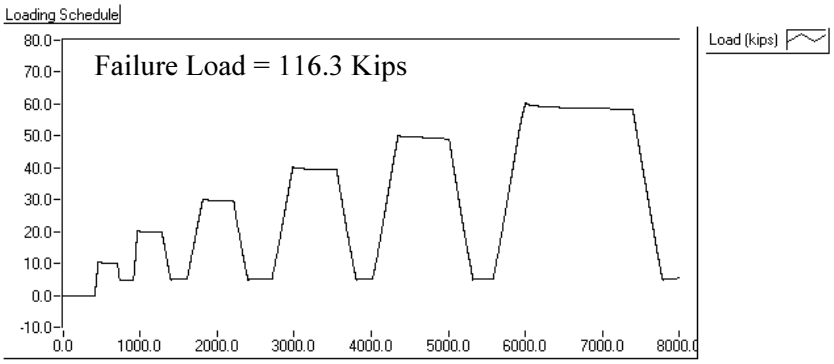

c) Load vs Time for BG2

Figure 4.20 – Time Based Graphs for BG2

4.4.2.3 BG4

The graph of cumulative MARSE vs. load for BG4 is shown in Figure 4.21. Felicity Ratios were calculated and are shown in Table 4.9. Felicity Ratios stayed high (greater than 0.9) until cracking, and then dropped off dramatically. This same trend was seen in BG1. The amount of emission in Figure 4.21 is small, and very similar to that of BG1. In addition, most emission occurs during loading and very little during load holds.

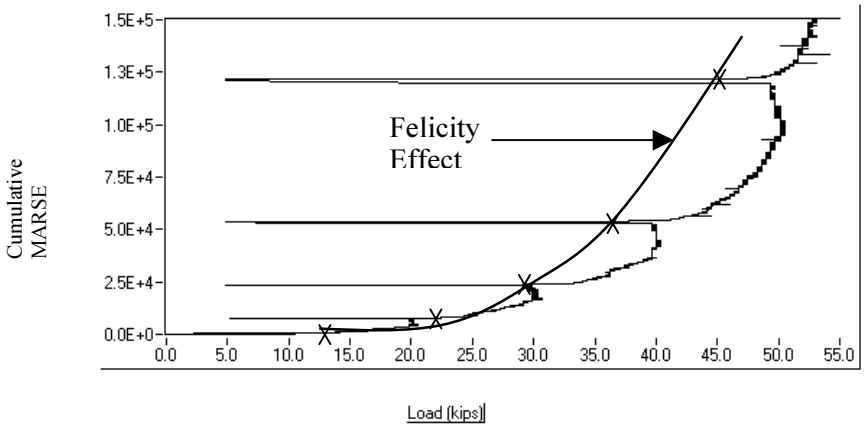

Figure 4.21 – Cumulative MARSE vs. Load for BG4

Table 4.9 – Felicity Ratios for BG4

Previous Load (kips)	Emission on Reload (kips)	Felicity Ratio/CBI	
10.0	14.2	1.42	
20.1	22.8	1.13	
30.7	29.5	0.96	
40.4	36.6	0.91	First
50.5	45.2	0.90	Crack
62.5	34.8	0.56	← Detected

Graphs of amplitude vs. time and Historic Index vs. time for BG4 are shown in Figure 4.22. The only major peak in the Historic Index corresponds to the cracking load. Amplitudes steadily increase until the cracking load, where hits over 95 dB are recorded.

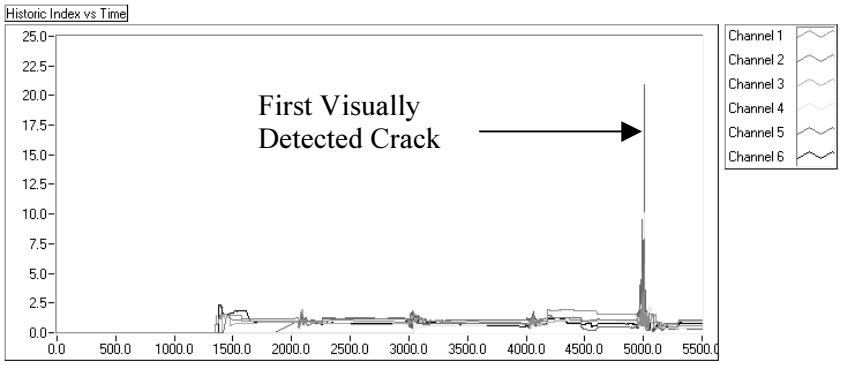

a) Historic Index Vs Time for BG4

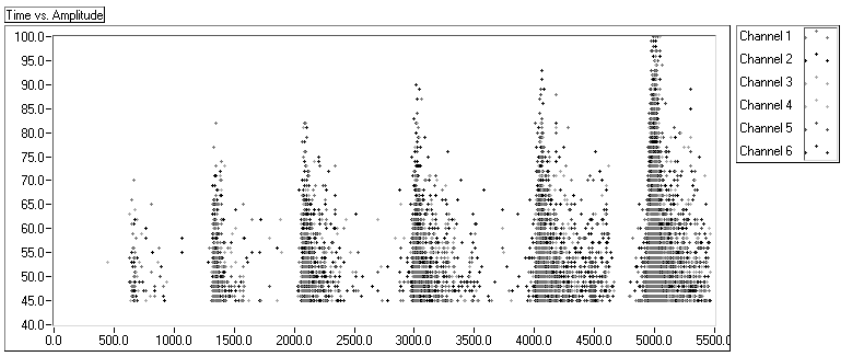

b) Amplitude vs Time for BG4

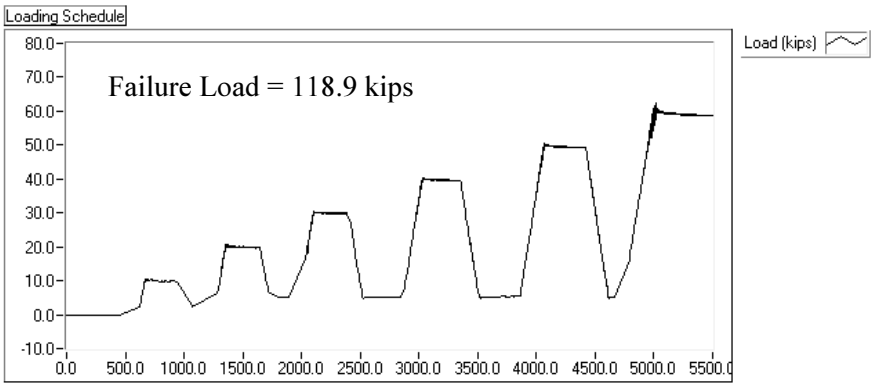

c) Load vs Time for BG4

Figure 4.22 – Time Based Graphs for BG4

4.4.3 Discussion of Flexure-Dominated Tests on Box Girders

Although BG4 was expected to be in the worst condition due to the continuous wetting, this was not seen in the flexure-dominated tests. Although some areas were significantly deteriorated, these were located at large blocks of concrete, such as at the ends and the interior block-outs. The critical region near midspan

had no major cracks, and no crack existed along the interface of the two pours as in the other specimens. Reinforcement was not corroded and no water leaked out of the flexural zone at failure, indicating very few pre-existing cracks in the flexural area. The final indication of very little distributed damage is that BG4 failed at the highest load.

The lack of damage in BG4 is also shown in its acoustic emission response. In all key AE parameters, BG4 was similar to BG1, the control beam. Although slight differences exist, indicating that BG4 is slightly more deteriorated than BG1, these two are grouped together as the less-damaged specimens for the remainder of this discussion.

The acoustic emission response of damaged specimens was considerably different from that of the less-damaged ones.

1. The most striking difference is in the amount of emission. The graphs of cumulative MARSE vs. load demonstrate that the damaged specimen has 10 times more emission before cracking than the less-damaged specimens. This is partly due to the fact that BG2 cracked at a higher load (60 kips compared to 50 kips), but there is also more emision at similar load levels.
2. Another important difference is that BG2 has more emission during load holds. This can be seen from the increase in cumulative MARSE while the load is staying constant or slightly decreasing.
3. Finally, the Felicity Effect is detected before cracking in the badly damaged specimen, while in the better specimens it was not seen until after crack initiation. Felicity ratios for BG1, BG2 and BG4 are presented in Figure 4.23. The Felicity Ratio for BG1 does not decrease below 1.0 until cracking has occurred. For the more heavily damaged specimen BG2, however, the Felicity Ratio is considerably below 1.0 after the first interval.

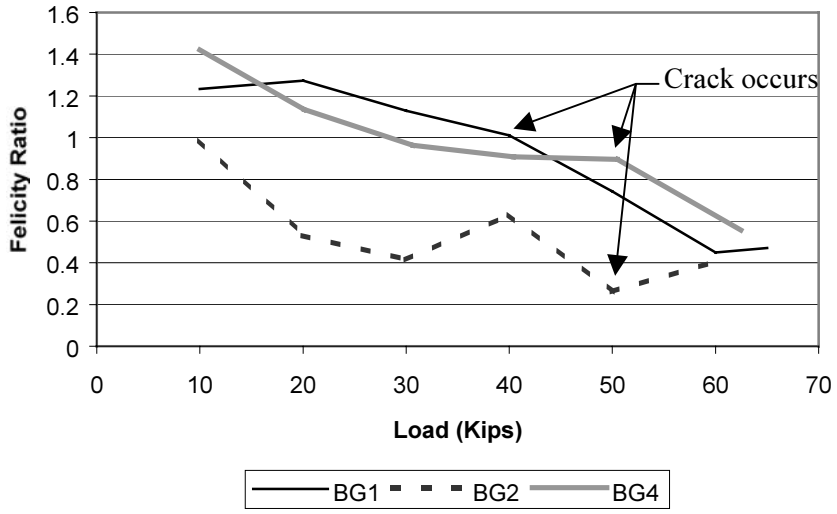

Figure 4.23 – Felicity Effect for Flexure Specimens

It was intially thought that the Historic Index would be a good indicator of significant events. It is true that at first cracking, the Historic Index has a sigificant peak for all the specimens. The good specimen BG1, however, has peaks at relatively low loads of 20 kips and 30 kips. These peaks may be due to the definition of Historic Index. Since Historic Index compares the MARSE of the last few hits to all of the previous hits, large MARSE hits early in the test create a high average MARSE at the beginning. In contrast, later in the test there is a larger base for average MARSE. Therefore a large peak in the Historic Index later in the test is more indicative of damage than one earlier in the test. Due to this fact, Historic

Index is a better indicator of a sigificant event on the more damaged specimen that has many hits immediately, where there are insigificant peaks in the good specimen.

One interesting trend in the data was the amplitude of hits over time. The less damaged specimens had very few hits over 90 dB, whereas the more damaged specimen had hits over 90 dB almost immediately.

4.5 AE RESPONSE OF FULL-SCALE PRESTRESSED BOX GIRDERS IN SHEAR

After the flexure tests were completed, there was concern that the badly deteriorated ends would weaken the bond of the concrete to the prestressing strands and decrease the capacity of the girder as governed by shear. To test this, one end from BG1, BG2, and BG4 were tested in shear while monitoring acoustic emission.

4.5.1 Setup of Shear-Dominated Tests on Box Girders

The setup for the shear tests was similar to that of the flexural tests. Steel spreader beams were used to distribute the load to four points on the web. Again, these beams rested on rollers, which were connected to the girder with hydrostone. Bearing pads were placed between the steel beams to isolate the test specimen from vibrations in the testing machine. Stronger spreader beams were required due to the increased load that was expected.

To distinguish the shear tests from the flexural tests, a different nomenclature was adopted. The shear test of the control beam (BG1) was designated BG1S; the shear test of the more deteriorated beam (BG2) was designated BG2S; and the shear test of the wetted beam was designated BG4S.

BG1S and BG4S were set up with a shear span of 2 times the distance from the top to the centroid of the prestressing strand, or 46 inches. One support was located near the end of the solid end block, and the other support was located approximately at the interior solid blockout. This resulted in a distance between the supports of 276.5 inches. Figure 4.24 shows the setup for these specimens; the large arrows represent where the beams loaded the rollers on the webs.

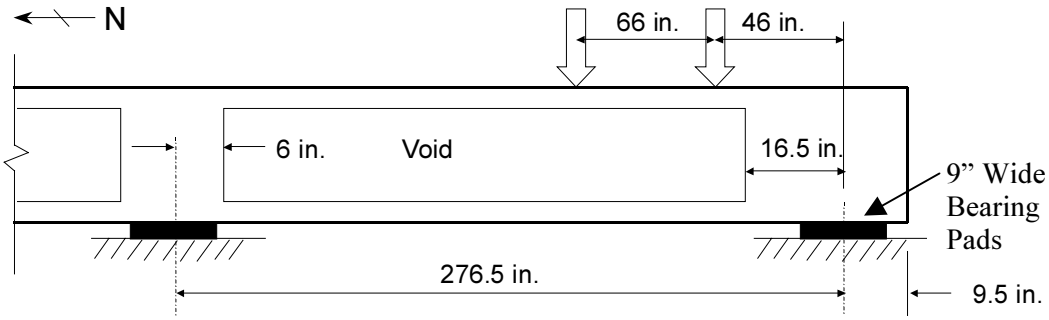

Figure 4.24 – Test Setup for BG1S and BG4S

The test setup for BG2S was similar except that it had a shear span of 1.5 times the distance from the top to the centroid of the prestressing strand, or 35.5 inches. One support was located on the northernmost point of the solid end block, and the other support was located approximately at the interior solid blockout. This resulted in a distance between the supports of 266 inches. Figure 4.25 shows the setup for BG2S. The setup of BG2S was intended to force crushing of the compression strut, while BG1S and BG4S represented support conditions used in the field.

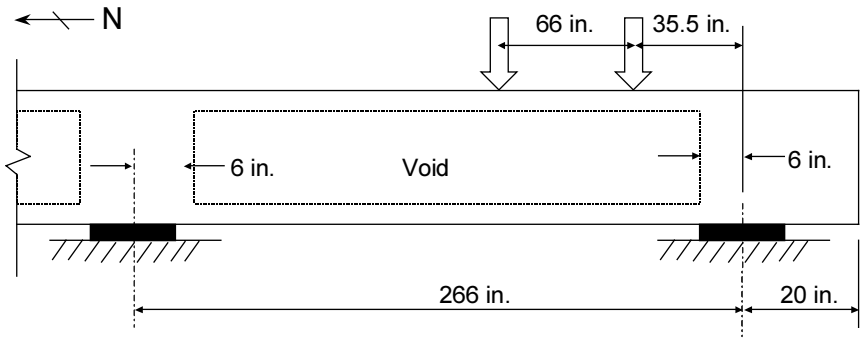

Figure 4.25 – Test Setup of BG2S

The sensor arrangement was similar to that of the flexure tests, but the sensors were spaced closer together because the area of interest is smaller. Unfortunately, the sensors were not able to bracket the shear area. Rather, they were placed a little to one side because of other transducers. This offset was not a problem since the entire shear area could be monitored with this configuration. A diagram showing the sensor placement for both tests is shown in Figure 4.26.

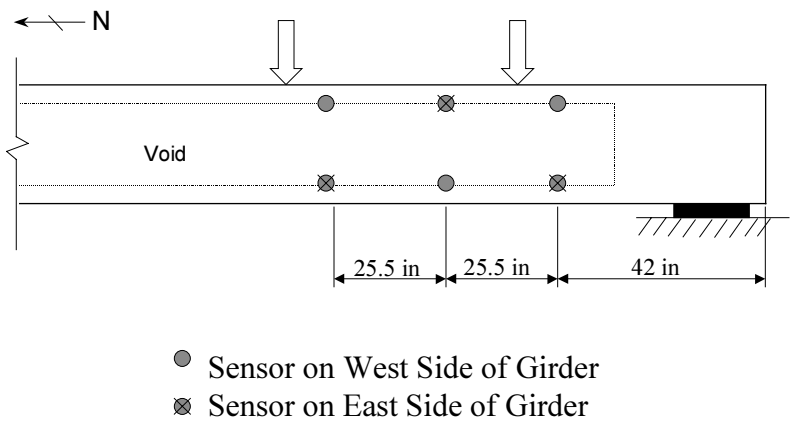

Figure 4.26 – Sensor Locations on all Shear Specimens

The loading schedule for the shear tests was constructed so that the Felicity Effect could be examined. Since the maximum load was expected to be considerably larger than in the flexure tests, a loading increment of 20 kips rather than 10 kips was used. The loading schedule for BG1S is shown in Figure 4.27. BG2S was accidentally loaded to an increase of 55 kips at the first interval, but the proper increase of 20 kips was used in subsequent intervals.

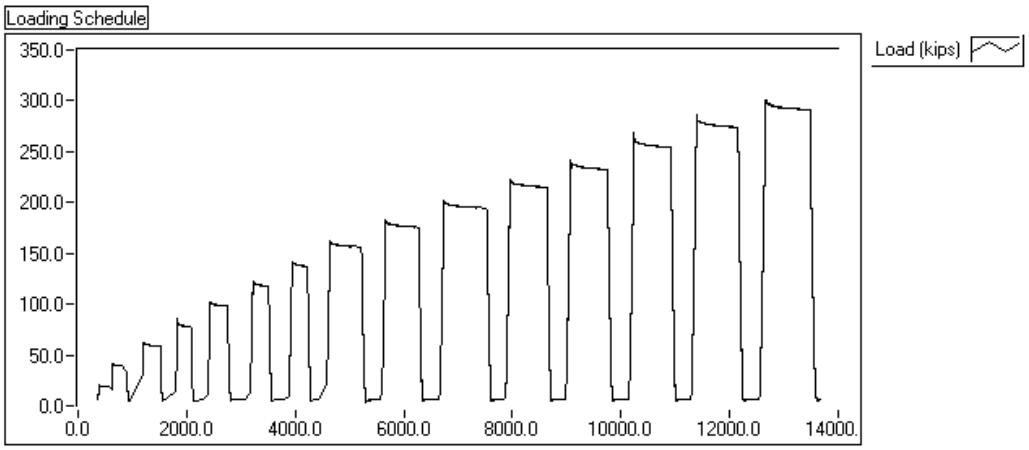

Figure 4.27 – Loading Schedule for BG1S

4.5.2 Results of the Shear-Dominated Tests on Box Girders

4.5.2.1 BG1S

Figure 4.28 shows the graph of cumulative MARSE vs. load for BG1S, up to the cracking load of 160 kips. The Felicity Ratio was as in the flexure tests (a cumulative MARSE increase of 300 above the value at 8 kips when reloading). Results are shown in Table 4.10. The Felicity Ratio is around 0.9 for BG1S until about 80 kips; during the next increment it then starts to decrease, and emission during load holds begins to increase.

The time-based graphs for BG1S are shown in Figure 4.29. Amplitudes at low loads are larger than in the flexure tests, but still relatively low. In fact, no hits above 90 dB occur until 140 kips is reached. Historic Index shows a major peak at the cracking load.

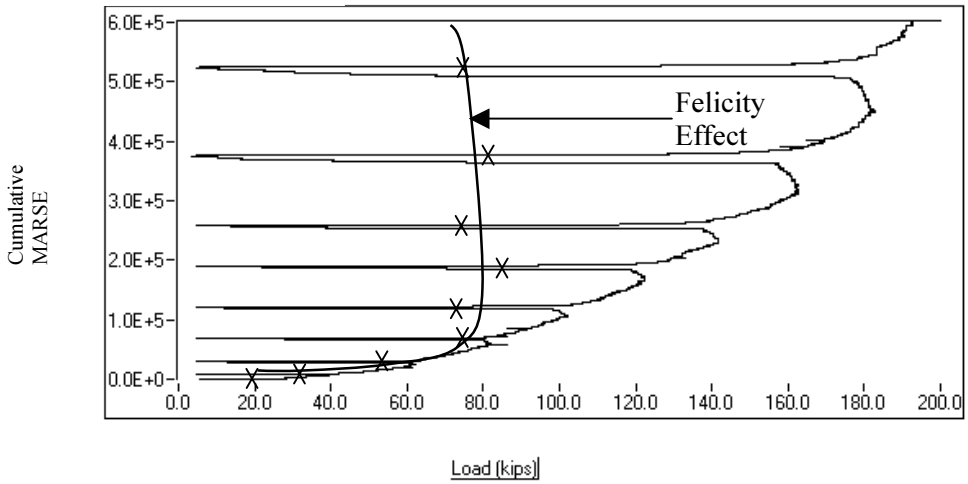

Figure 4.28 – Load Vs Cumulative MARSE for BG1S

Table 4.10 – Felicity Ratios for BG1S

Previous Load (kips)	Emission on Reload (kips)	Felicity Ratio/CBI	
20	22.80	1.14	
41	35.89	0.88	
61	55.70	0.91	
80	75.52	0.94	
101	72.53	0.72	
122	86.36	0.71	
142	77.02	0.54	First Detected Crack
162	80.38	0.50	
182	77.02	0.42	
201	40.00	0.20	

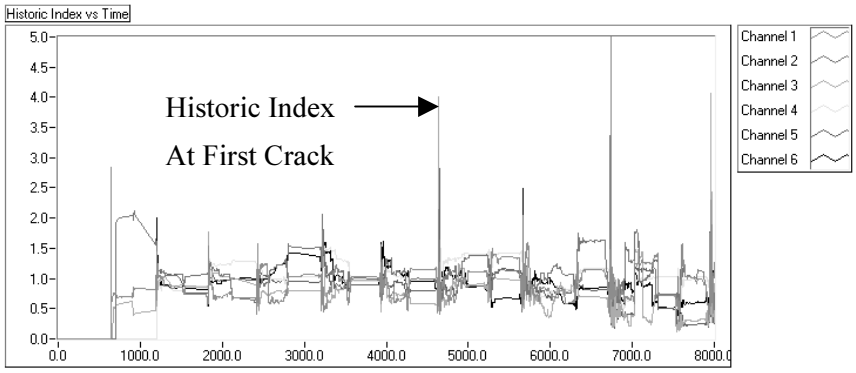

a) Historic Index Vs Time for BG1S

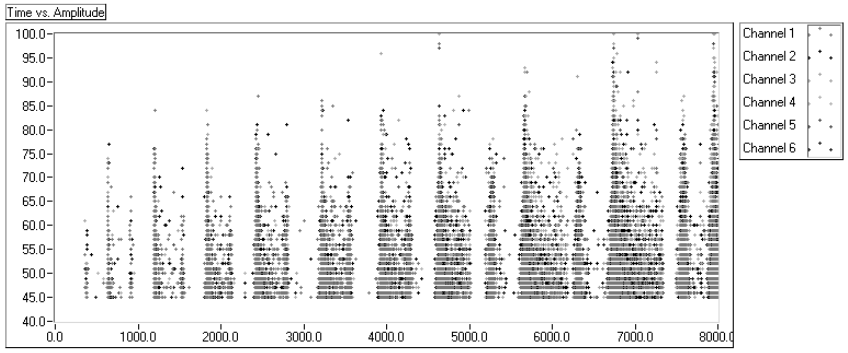

b) Amplitude vs Time for BG1S

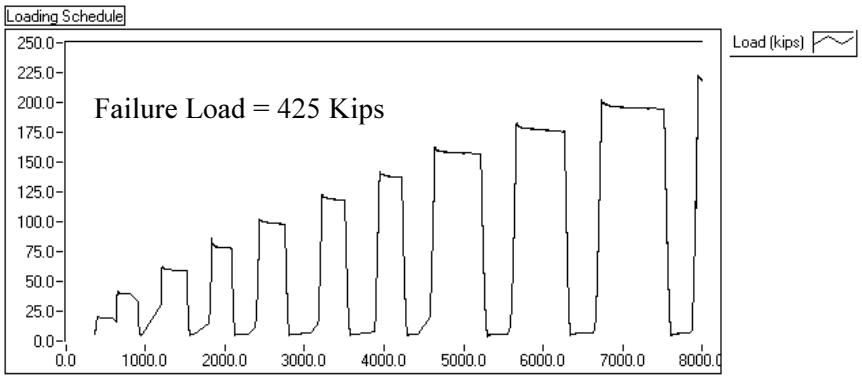

c) Load vs Time for BG1S

Figure 4.29 – Time Based Graphs for BG1S

4.5.2.2 BG2S

The badly damaged beam, BG2S, was also tested in shear. The load was accidentally increased to 55 kips for the first interval. While this made it impossible to examine the Felicity Effect at low loads, general behavior can be examined. Figure 4.30 shows the graph of cumulative MARSE vs. load for BG2S before cracking was detected. Results from the shear test resemble those from the flexural test. The badly damaged beam shows emission during load holds, and the Felicity Effect is prevalent, especially at higher loads (Table 4.11). In every cycle except the first, the Felicity Ratio is below 0.7.

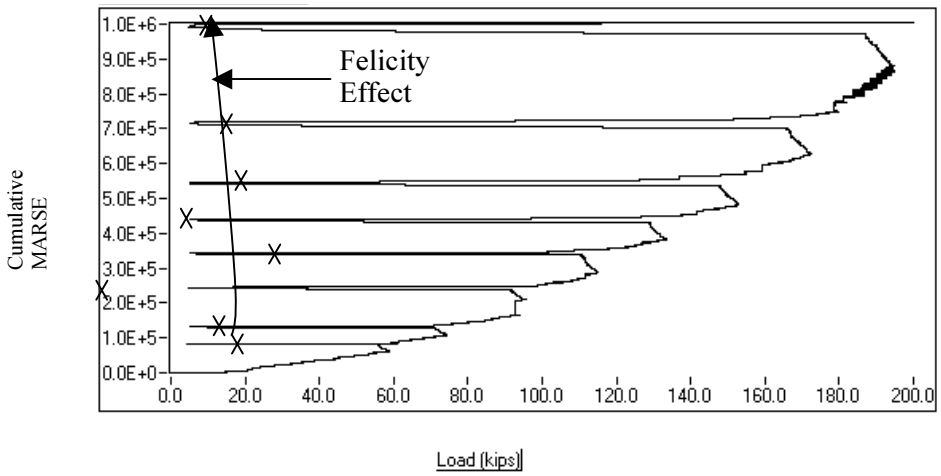

Figure 4.30 – Cumulative MARSE vs. Load for BG2S

Table 4.11 – Felicity Ratios for BG2S

Previous Load (kips)	Emission on Reload (kips)	Felicity Ratio/CBI	
56	58.32	1.04	
73	49.72	0.68	
95	16.82	0.18	
114	63.56	0.56	
133	37.38	0.28	
153	56.00	0.37	
172	53.46	0.31	First Detected Crack
194	42.25	0.22	
212	48.23	0.23	

Figure 4.31 shows hit amplitudes consistently above 90 dB for the entire test, and a few are from 95 to 100 dB.

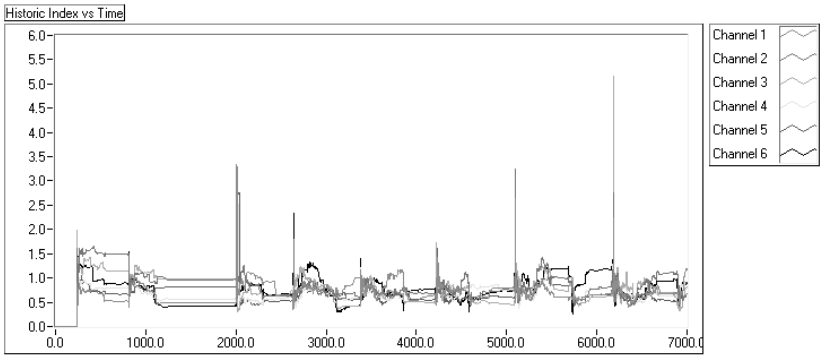

a) Historic Index vs Time for BG2S

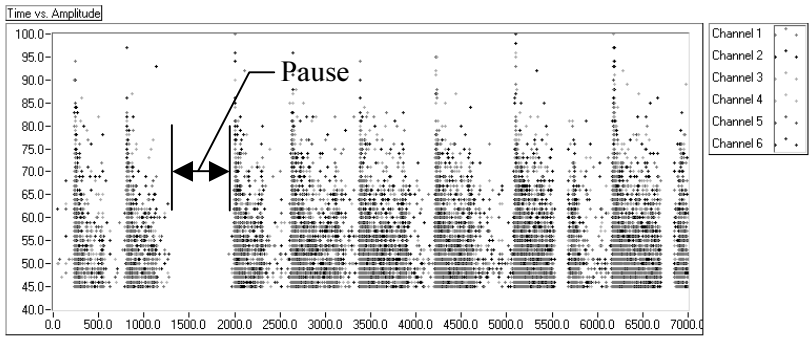

b)Amplitude vs Time for BG2S

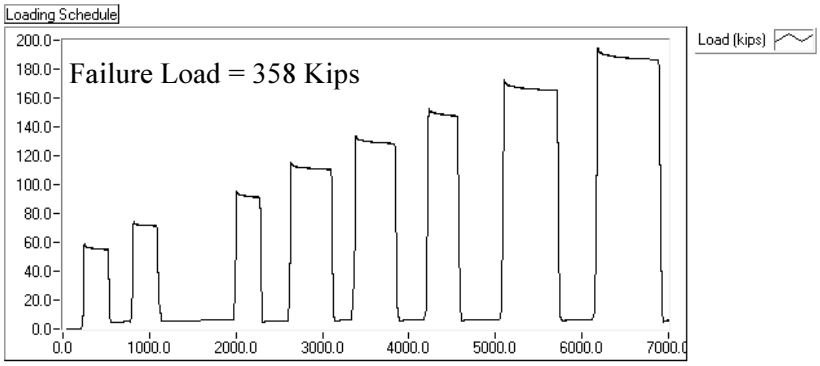

c) Load vs Time for BG2S

Figure 4.31 – Time Based Graphs for BG2S

4.5.2.3 BG4S

BG4S was the final shear test performed on a box girder section. This specimen failed very differently than the previous two shear specimens. BG4S had a bearing failure (Figure 4.32) while the previous specimens failed in the compression strut (Figure 4.33). A weak plane (vertical delamination) was created in the center of the web due to a combination of premature concrete deterioration and corrosion of the reinforcement.

Figure 4.32 – Bearing Failure of BG4S

Figure 4.33 – Compression Strut Failure of BG1S

During the test, a metallic clicking sound was heard periodically from the test setup. Although it did not originate from the test specimen, its cause was not found. By watching the acoustic emission as the noise was heard, the associated emission was determined to be low amplitude, long duration, and high MARSE, all characteristic of mechanical rubbing. This is also shown in the plot of amplitude vs. log duration in Figure 4.34. As this clicking was heard, hits were detected in the area marked on that figure. No emission in this area had been noted in any other tests, indicating that it was probably due to external sources. This external emission was eliminated with a Swansong II filter.

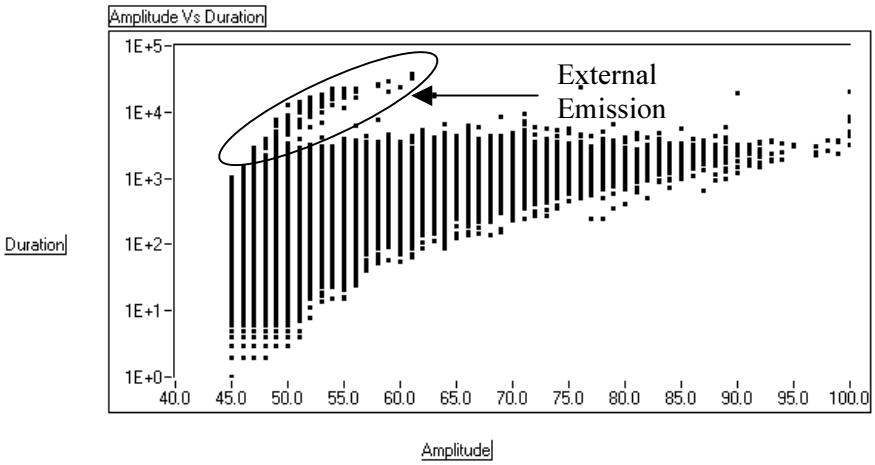

Figure 4.34 – Amplitude vs Log Duration for BG4S

The Swansong II filter is a standard technique for identifying and eliminating extraneous emission from a data set. It is incorporated into the procedure for testing tank cars (AAR IM 101) and the MONPAC procedure (Fowler et al. 1989), and is normally used to filter external emission from sources such as leaks or mechanical rubbing. The filter works by identifying "telltale" hits and eliminating all data within ½ a second before or after a telltale hit. Telltale hits are defined by their amplitude and duration and are listed in Table 4.12.

Table 4.12 – Definition of a "Telltale" Hit for the Swansong II Filter

Amplitude		Duration
< 5 dB plus the Threshold	And	> 2 milliseconds
	- Or -	
< 10 dB plus the Threshold	And	> 3.5 milliseconds
	- Or -	
< 15 dB plus the Threshold	And	> 4.5 milliseconds

The filtered plot of amplitude vs. log duration is shown in Figure 4.35. Hits in the uncharacteristic area are removed, indicating that the filter was effective. Remaining discussion of BG4S refers to filtered data.

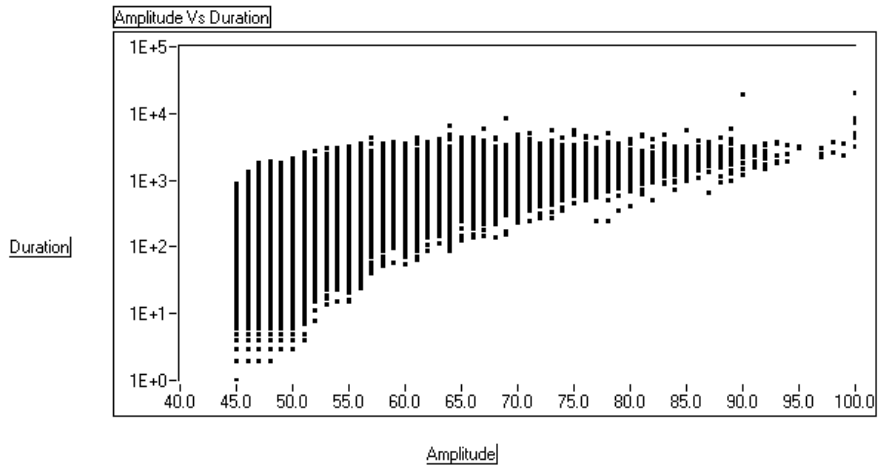

Figure 4.35 – Amplitude vs Log Duration for BG4S after Swansong II Filter

The acoustic emission response of BG4S was much different from that of the previous shear specimens. The graph of cumulative MARSE vs. load before cracking is shown in Figure 4.36. The major difference between this test and the previous shear tests is the emission during unloading. This trend is shown clearly for loads above 125 kips in Figure 4.36. If lower loads are examined more carefully, however, emission during unloads can be seen even in the first few cycles. This graph also shows that the overall amount of MARSE is low relative to the other shear specimens. The Felicity Ratios for this specimen are shown in Table 4.13. They stay around 1.0 until about half the cracking load, and then start to decrease.

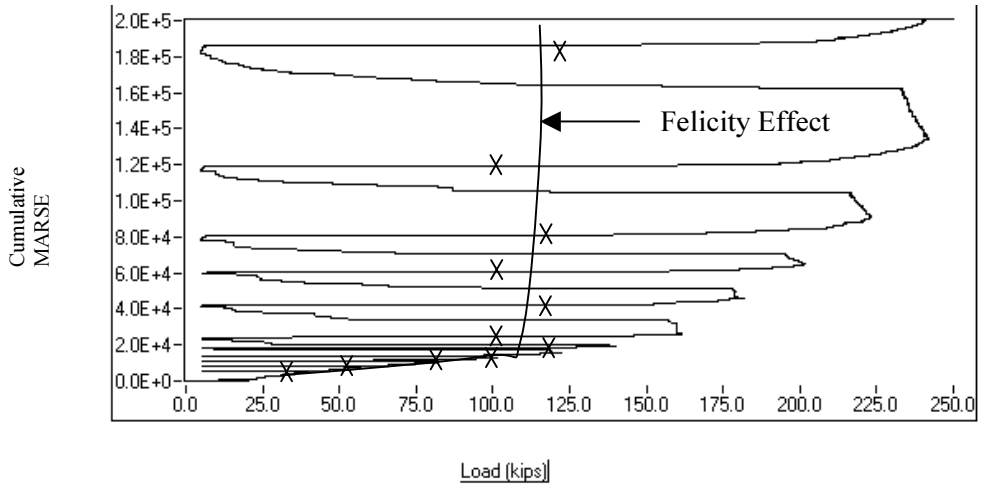

Figure 4.36 – Cumulative MARSE vs. Load for BG4S

Table 4.13 – Felicity Ratios for BG4S

Previous Load (kips)	Emission on Reload (kips)	Felicity Ratio	
40.7	43.0	1.1	
60.0	66.2	1.1	
82.3	81.5	1.0	
99.8	103.2	1.0	
121	127.2	1.1	
140.2	101.7	0.7	
161.6	127.2	0.8	
181.8	99.1	0.5	
201.6	123.8	0.6	
223.3	142.9	0.6	
242	109.2	0.5	First
262.2	94.2	0.4	← Detected Crack

As shown in Figure 4.37, no large peaks occur in the Historic Index before cracking, and no high amplitude hits occur until the 125 kip loading increment. Significantly, this is also where the Felicity Ratio begins to decrease.

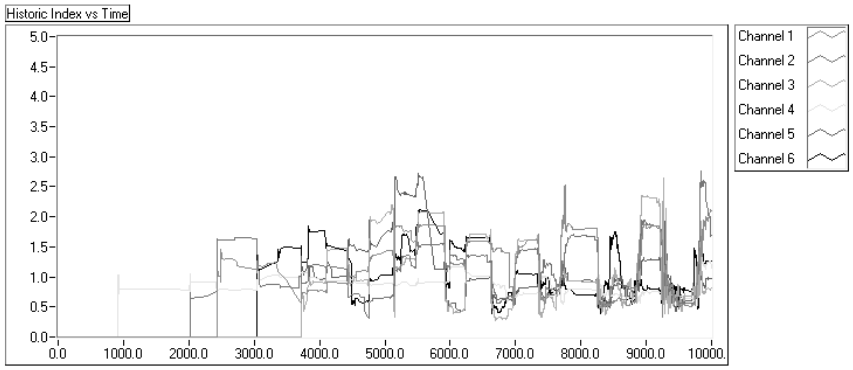

a) Historic Index vs. Time for BG4S

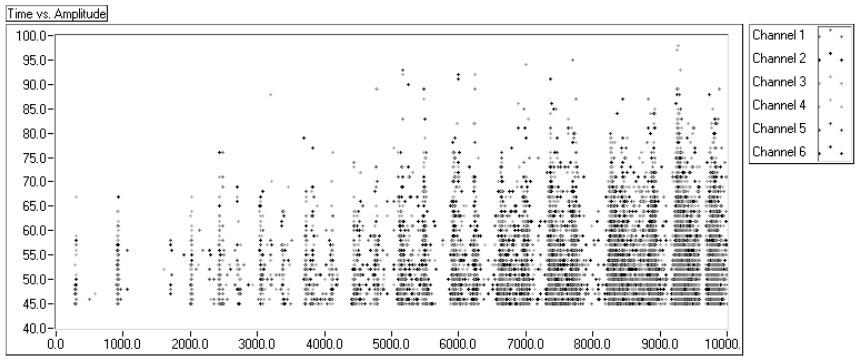

b) Amplitude vs Time for BG4S

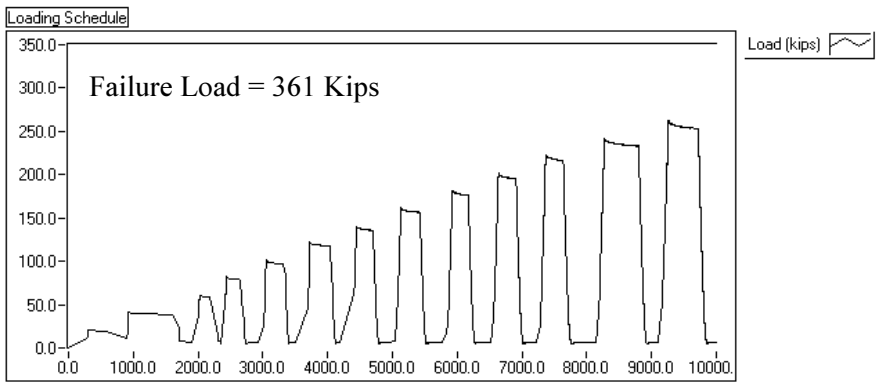

c) Load vs Time for BG4S

Figure 4.37 – Time Based Graphs for BG4S

4.5.3 Discussion of the Shear-Dominated Tests on Box Girders

Although BG4S had significant deterioration, as can be seen by its failure mode, it did not have the largest amount of acoustic emission, and its Felicity Ratios did not decrease rapidly, as was seen in the other badly damaged girders. One possible explanation, based on the crack pattern at failure (Figure 4.34), is that a delamination at the end may have blocked the acoustic emission from the sensors. A delamination at the end would also explain the emission during unloading. A delamination may cause

the outside wall to move slightly outward during loading. This would not create emission since there would be no rubbing between surfaces. On unloading, however, the delamination would close, and cause rubbing on the two surfaces. The high Felicity Ratios are then explained because of the orientation of the delamination. If the internal stress due to the premature concrete deterioration were relieved by a vertical crack in the plane of the web, the loading method used would not stress this type of defect. In the other shear tests, most of the cracking was parallel to the axis of the beam, and the horizontal shear would cause rubbing between the crack surfaces.

If the vertical delamination in the web is the cause for the difference in acoustic emission response of this test specimen, future tests should either use impact-echo to inspect for delaminations before monitoring with acoustic emission, or monitor acoustic emission closely during unloading cycles.

The other two shear tests, BG1S and BG2S, can be compared directly since they failed by the same mechanism. As shown in Chapter 3, BG2S was more deteriorated than BG1S. From these tests, cumulative MARSE is a good indicator of the amount of deterioration. Even though BG1S underwent more cycles than BG2S, its cumulative MARSE is lower. It is important to compare similar load levels, since the graph scales are different. The cumulative MARSE plots also show that emission during load holds starts at a lower load in BG2S. Finally, a graph comparing the Felicity Ratios for the two shear specimens is presented in Figure 4.38. Although the first point for BG2S is above 1.0, the ratio drops off significantly for the other cycles and is below BG1S for every other load increment.

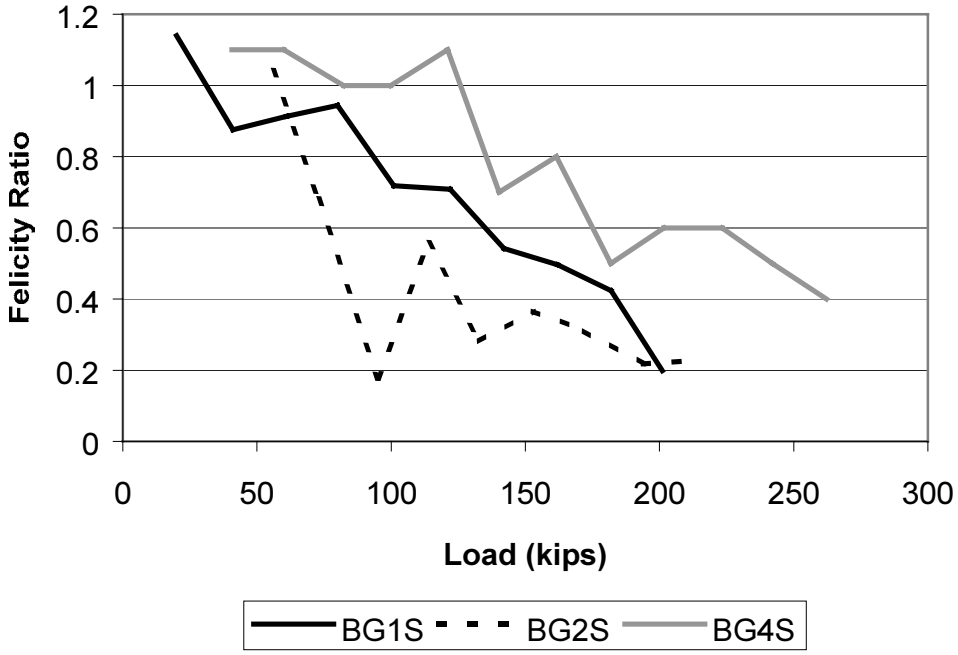

Figure 4.38 – Felicity Ratios for the Shear-Dominated Test on Box Girders

Another similarity to the flexure tests is that the badly damaged specimen exhibits hits with much higher amplitudes very early in the testing. Hits of 90 to 100 dB are common on even the first loading of BG2S, but do not appear at all in BG1S until approximately the 140 kip increment.

Unfortunately, Historic Index does not provide much information. Both tests show a large peak on the graph corresponding to the first detected crack, but it is unclear what the previous peaks signify. They may be due to crack opening not large enough to be detected visually. Regardless, these results are well above any load that could be applied in a practical field test.

The same general trends were detected in the shear tests as in the flexural tests, except that the difference in the specimens was not as great. This may be because the damage in BG1S, though small, was concentrated at the ends of the girders.

Vertical delaminations give a very different pattern of acoustic emission than horizontal cracks. They are not stressed in the same manner and produce more emission during unloading.

4.6 SHEAR TESTS OF FULL-SCALE TYPE C GIRDERS

4.6.1 Test Setup for Shear-Dominated Test on Type C Girders

The condition of the girders was determined by visual inspection as discussed in Chapter 3. Crack ratios were calculated by dividing the area of the cracks by the surface area of the girder. The results of these calculations are summarized in Table 4.14.

Table 4.14 – Crack Ratios for Type C Girders

Specimen	Crack Ratio %
Girder 1 - East End (G1ES)	1.64
Girder 1 – West End (G1WS)	1.57
Girder 2 – East End (G2ES)	0.71
Girder 2 – West end (G2WS)	1.76

The shear specimens were loaded by a hydraulic ram controlled with an air pump. This ram loaded a spreader beam, which was supported by bearing pads. The girder itself also rested on bearing pads, which isolated the specimen from any external vibration. A detail of the test setup is shown in Figure 4.39. Dimensions for the test setups are shown in Table 4.15.

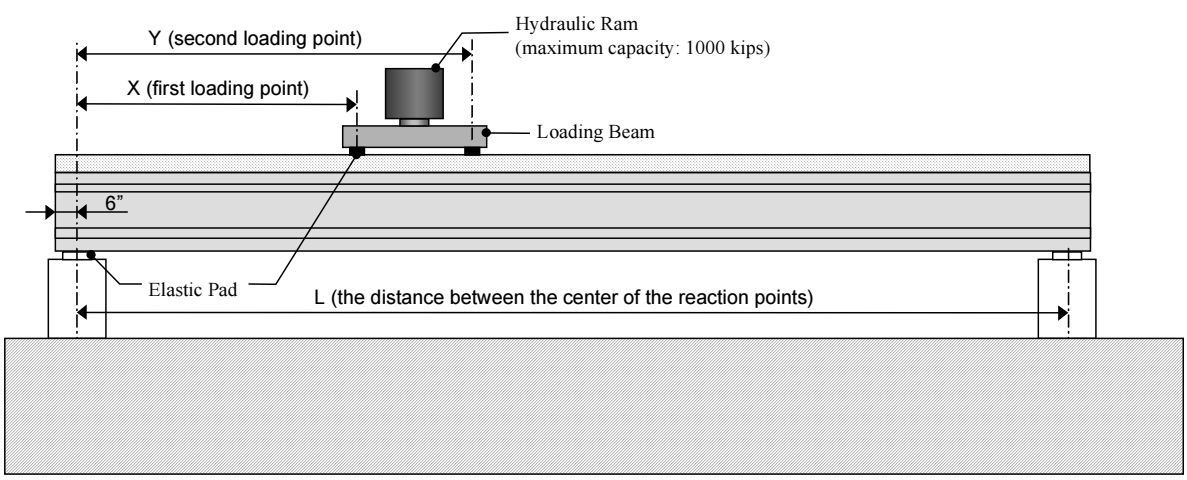

Figure 4.39 – Test Setup for Type C Girders

Table 4.15 – Dimensions of Test Setup

Dimension in Figure 4.39	G1ES	G1WS	G2ES	G2WS
L (Length in Feet)	30	30	35	35
X (Distance to the first loading point in Feet)	6	6	6	10
Y (Distance to the second loading point in Feet)	10	10	10	14

Sensor placement was based upon the same attenuation test that was described in the test setup for the flexure tests. Sensor placement is shown in Figure 4.40, and dimensions for this figure are shown in Table 4.16. Emission was recorded using a 6-channel MISTRAS digital acoustic emission system and R6I sensors. Data were analyzed using programs written by the author in C++ and LabView.

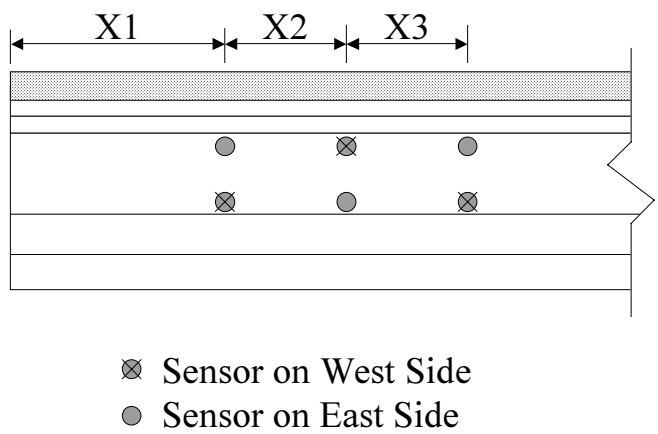

Figure 4.40 – Sensor Placement for Type C Specimens

Table 4.16 – Locations of Sensor Placement on Type C Girders

Dimension in Figure 4.40 (in inches)	G1ES	G1WS	G2ES	G2WS
X1	41	41	41	52
X2	25.5	25.5	25.5	25.5
X3	25.5	25.5	25.5	25.5

4.6.2 Results of Shear-Dominated Test on Type C Girders

4.6.2.1 G2WS

The first specimen tested was G2WS. Although mistakes were made in both the setup and the loading schedule, this specimen was still useful in that much was learned for the subsequent tests.

Since this was the first test, the ideal loading schedule was not clear. A loading increment of 40 kips was initially chosen, which is about 10% of the predicted capacity. After a load hold, the load would then be reduced 40 kips. Due to the amount of acoustic emission generated, the loading increment was cut back to 5%, or 20 kips, and finally after 200 kips the specimen was loaded without unloads until failure. Only

one full unload was performed, due to a stop at the end of the day and a restart the next morning. The actual loading schedule for G2WS is shown in Figure 4.41. With the hydraulic ram instead of the displacement-controlled loading setup used for the box girders, it is much more difficult to control the load.

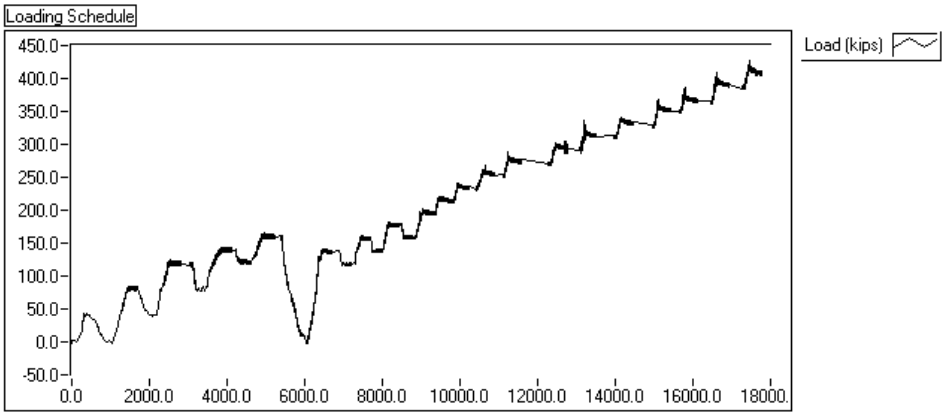

Figure 4.41 – Loading Schedule for G2WS

Since the loading schedule is inconsistent, it is difficult to draw conclusions from the data. The graph of cumulative MARSE vs. load is shown in Figure 4.42. It can be seen from the full unload that 10% unloads are insufficient to determine the Felicity Ratio, and emission in fact begins at a very low load. Significant emission occurs during unloaded periods, an indication that further unloads are necessary. Finally, significant emission occurs during load holds, as in the badly damaged specimens described earlier in this chapter.

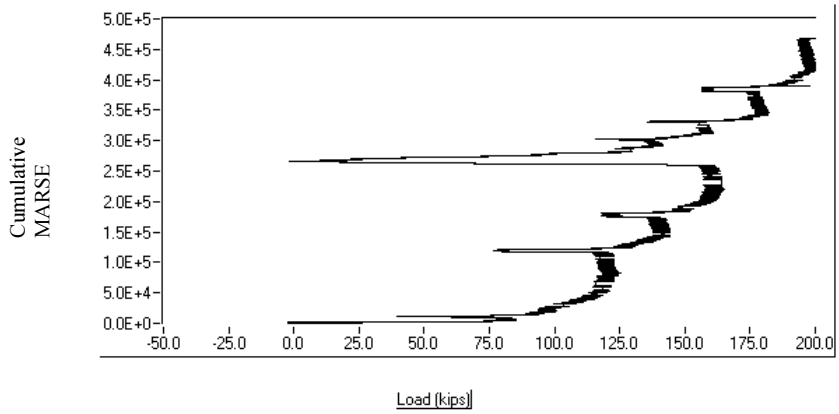

Figure 4.42 – Cumulative MARSE vs. Load for G2WS

Historic Index, amplitude, and load are plotted in Figure 4.43 up to the point that unloading stopped. Historic Index shows no significant peak in this time period. Amplitude of hits starts off low but reach 90 to 100 dB by the 120 kip loading increment.

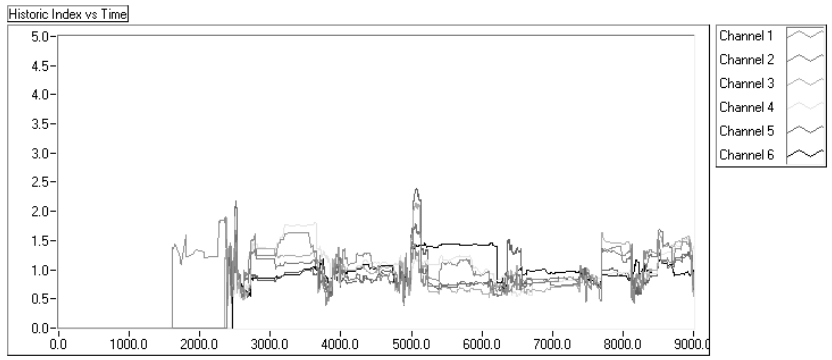

a) Historic Index vs. Time for G2WS

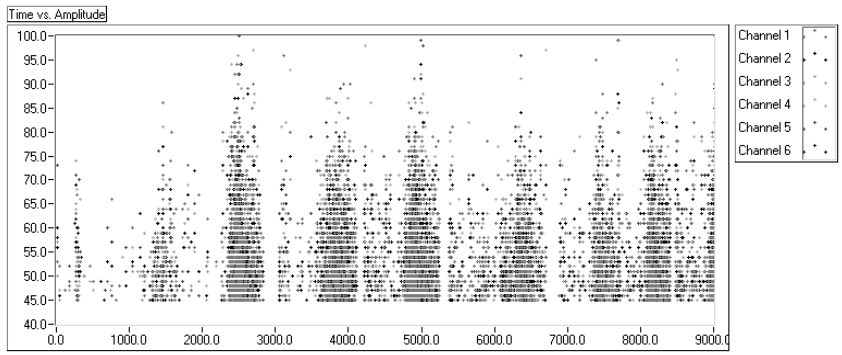

b) Amplitude vs. Time for G2WS

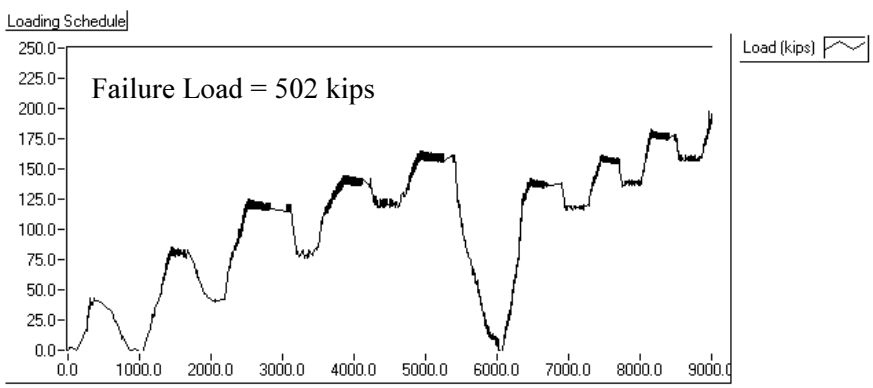

c) Load vs. Time for G2WS

Figure 4.43 – Time Based Graphs for G2WS

4.6.2.2 G2ES

From the visually determined crack ratio, G2ES was the least damaged specimen. Lessons from the first test were implemented and a shorter shear span was used with full unloads (Figure 4.44). This figure shows an apparent error in the load cell during the 180 kip load hold. This problem was corrected and the rest of the load values are correct. The loading schedule has constant intervals with full unloads, making it more convenient for studying the Felicity Effect. Since a shorter shear span was used, the sensors were shifted closer to the end in order to better bracket the area of interest.

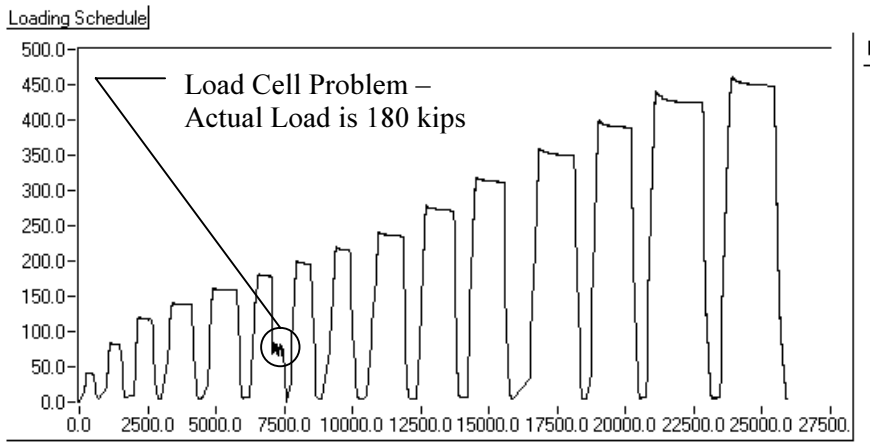

Figure 4.44 – Loading Schedule for G2ES

The first major shear crack was detected at 440 kips. Cumulative MARSE vs. load up to that point is plotted in Figure 4.45. As the load increases, emission during load holds increases and the Felicity Ratio decreases. The Felicity Ratio was calculated defining significant emission as the load where the cumulative MARSE is 300 above the value when the load passes 10 kips. In the analysis, 10 kips was used instead of 8 kips (the value used with the box girder specimens), because it was more difficult to control the load with the hydraulic ram. Although unloads were targeted at 5 kips, many were closer to 7 or 8 kips thus necessitating a higher load definition. The results of the Felicity Ratios are shown in Table 4.17. The Kaiser Effect is present until about 200 kips, and then starts to decrease. The decrease is also more significant near the cracking load.

The graph of Historic Index vs. time (Figure 4.46) displays one major peak at the cracking load, with a value of 101, off the chart. No other significant peak is detected. In the same figure, hit amplitudes are plotted vs. time. High amplitude hits begin at 180 kips, but do not become very prevalent until the 240 kip load increment, which is also where the Felicity Ratios begin to drop.

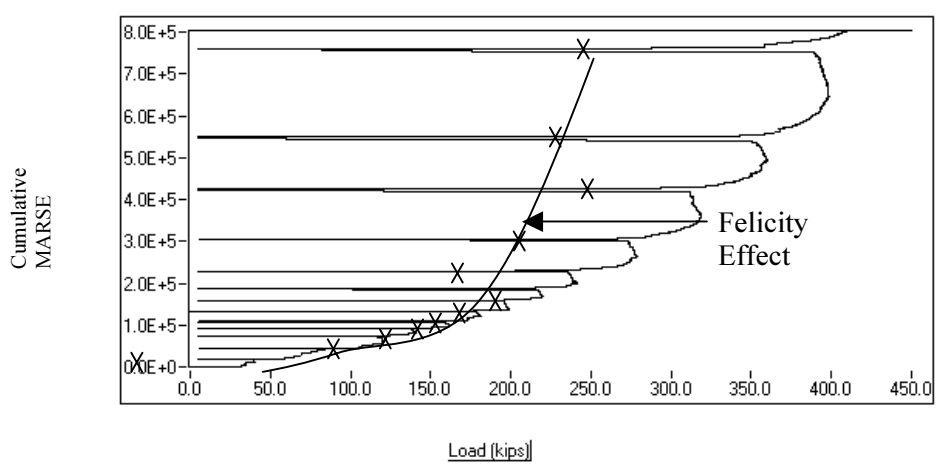

Figure 4.45 – Cumulative MARSE vs. Load for G2ES

Table 4.17 – Felicity Ratios for G2ES

Previous Load (kips)	Emission on Reload (kips)	Felicity Ratio/CBI
40	51	1.28
83	91	1.10
121	118	0.98
141	140	0.99
162	152	0.94
182	166	0.91
199	194	0.97
220	160	0.73
241	203	0.84
279	245	0.88
319	233	0.73
360	246	0.68
399	133	0.33
440	46	0.1

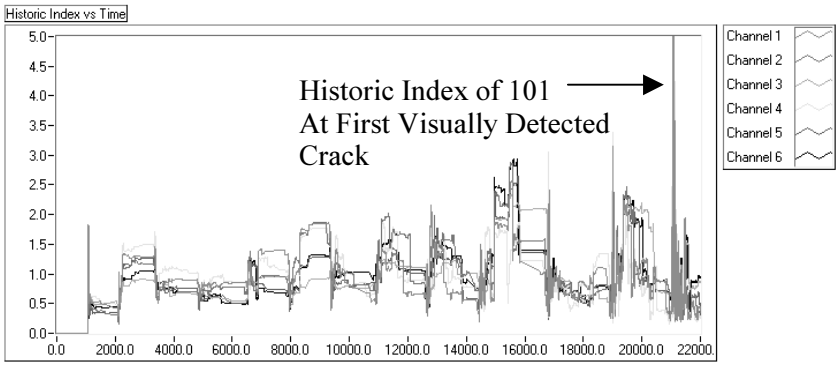

a) Historic Index vs. Time for G2ES

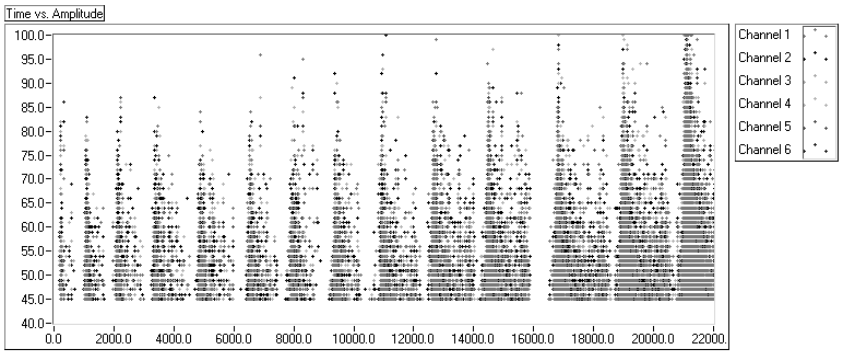

b) Amplitude vs. Time for G2ES

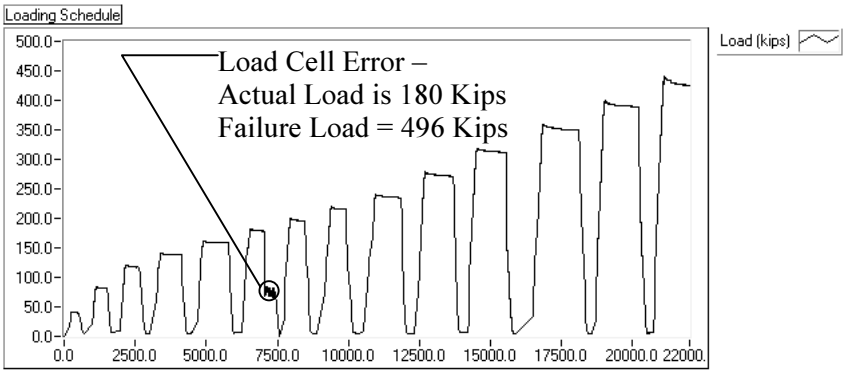

c) Load vs. Time for G2ES

Figure 4.46 – Time Based Graphs for G2ES

4.6.2.3 G1WS

The crack ratio of G1WS shows that it was one of the more damaged Type C specimens. G1WS was tested similarly to G2ES, except that it was shorter, giving a smaller shear force from a similar load. The rest of the setup, including sensor placement, was similar to that of G2ES. The loading schedule consisted of 30 kip increments with full unloading (Figure 4.47).

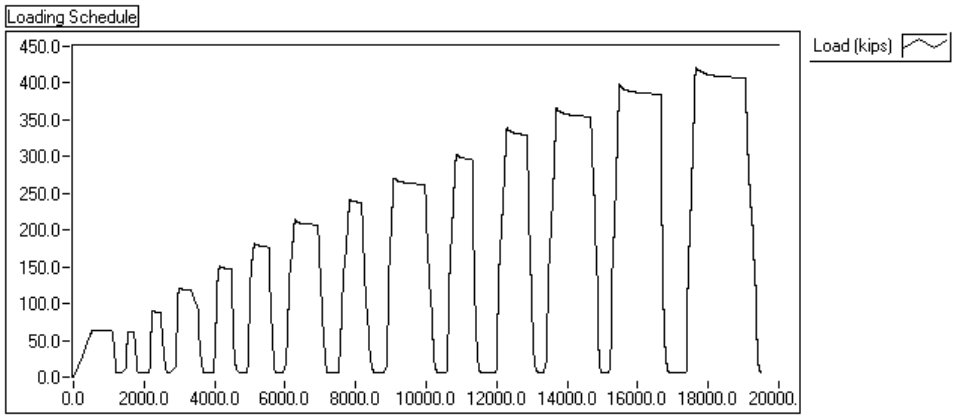

Figure 4.47 – Loading Schedule for G1WS

A diagonal shear crack was detected at 360 kips, a lower load than the previous specimen. Horizontal cracks were also detected in the web even earlier, at 270 kips (Figure 4.48). In this figure, most horizontal cracks were pre-existing and are due to the premature concrete deterioration, whereas most diagonal cracks opened during loading.

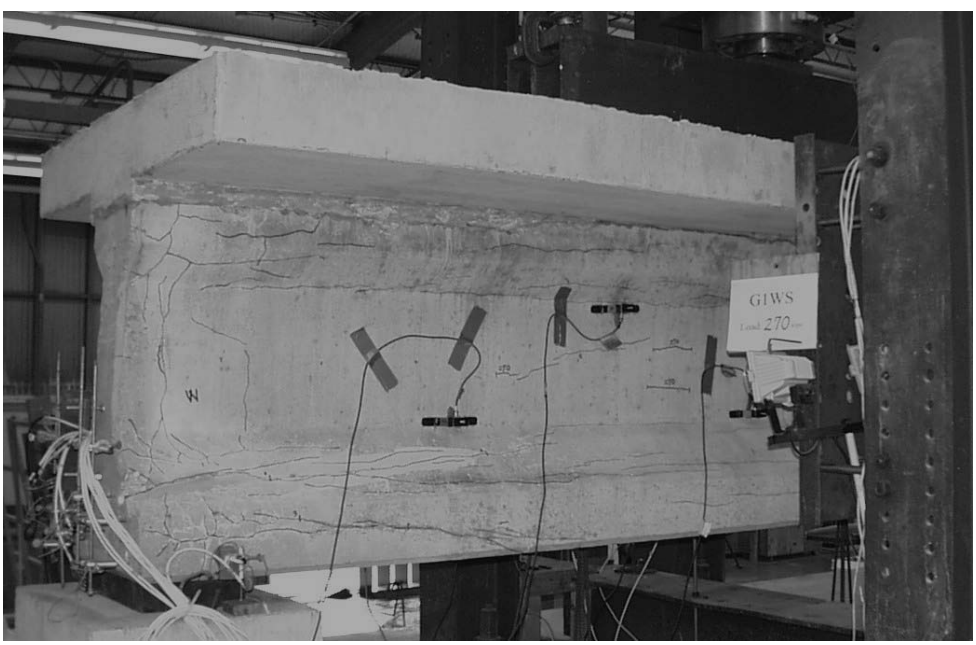

Figure 4.48 – G1WS under test at 270 kips

The graph of cumulative MARSE vs. load for G1WS before cracking is shown in Figure 4.49. One trend not evident in other specimens is the large amount of emission in the first few loading increments. The reason for this is unclear, and it affects only the first few increments. The remaining data show little emission during load holds until the horizontal cracks opened at 270 kips. In this test, the Felicity Effect is seen at very low loads. Felicity Ratios were calculated for G2ES (Table 4.18). They start off extremely low and decrease steadily as the load increases.

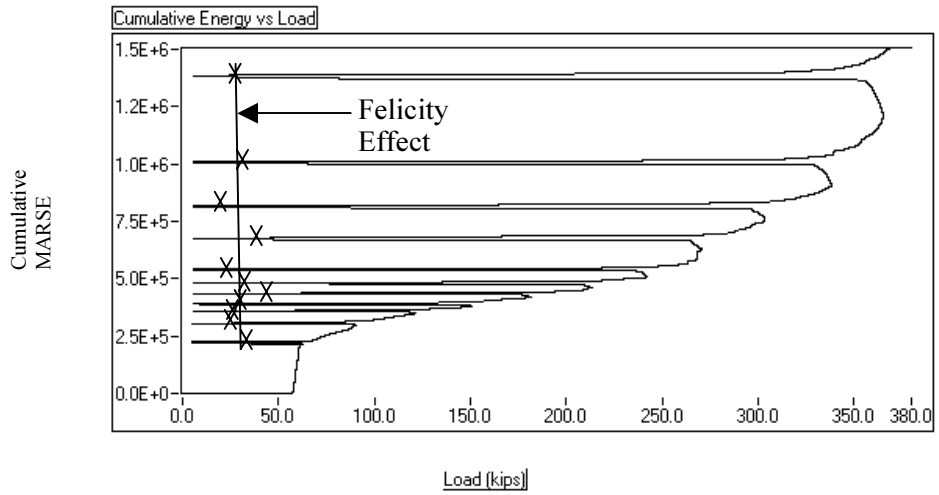

Figure 4.49 – Cumulative MARSE vs. Load for G1WS

Table 4.18 – Felicity Ratios for G1WS

Previous Load (kips)	Emission on Reload (kips)	Felicity Ratio/CBI
63	38	0.60
63	28	0.45
91	25	0.28
121	29	0.24
151	41	0.27
182	36	0.20
214	38	0.18
242	22	0.09
271	36	0.13 ← First Detected Crack
304	19	0.06
339	22	0.07
366	24	0.07
399	20	0.05

The graph of Historic Index (Figure 4.50) displays a small peak corresponding to the first detected crack, and it may provide some insight into why a crack was detected earlier than in the previous specimen. Although a small peak exists, it is not nearly as large as for the first crack. One possible explanation is that the cracks were pre-existing and opened wider during loading. When a crack opens, the Historic Index normally has a very large peak; in fact, for this specimen a peak during the 400 kip loading had a magnitude of 55. If the cracks were pre-existing, however, there would not be crack growth and therefore would not exhibit the same peak in Historic Index. Other evidence that the cracks were pre-existing is

that they do not run diagonally as expected, but rather horizontally. The horizontal cracks are consistent with the distributed damage seen in the field.

The graph of hit amplitude vs. time shows relatively low amplitudes until the horizontal cracks open at 270 kips.

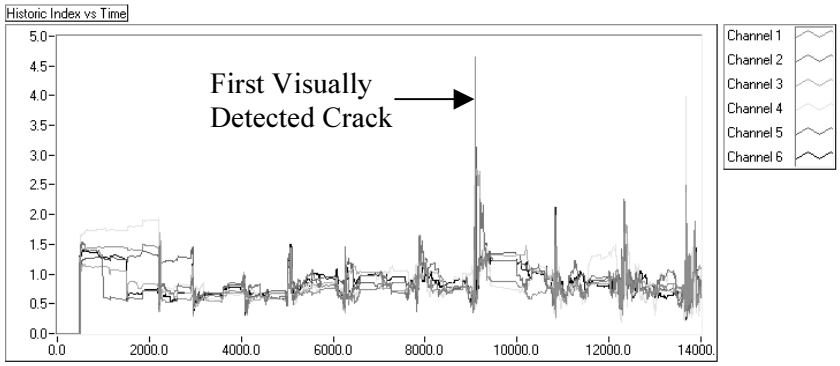

a) Historic Index vs. Time for G1WS

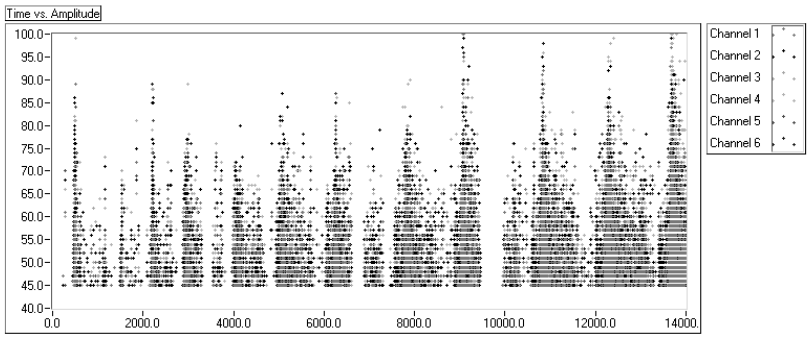

b) Amplitude vs. Time for G1WS

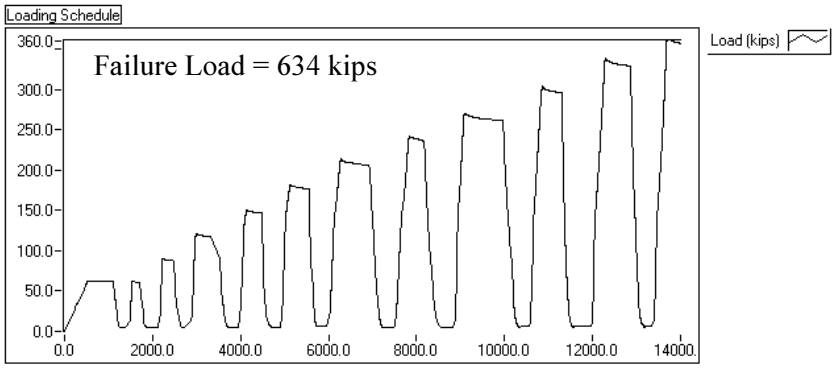

c) Load vs. Time for G1WS

Figure 4.50 – Time Based Graphs for G1WS

4.6.2.4 G1ES

The final shear specimen, G1ES, was one of the more damaged specimens, and in a similar condition to G1WS based on crack ratios. Details of the test setup were identical to G1WS with respect to shear span and sensor placement. A 30 kip loading increment was used, similar to the previous test. The actual

loading schedule is shown in Figure 4.51. The main difference from G1WS was the cracking loads. In G1ES the first crack was detected at 500 kips compared to 270 kips in G1WS. Even though their cracking loads varied, the failure loads for these two specimens were similar.

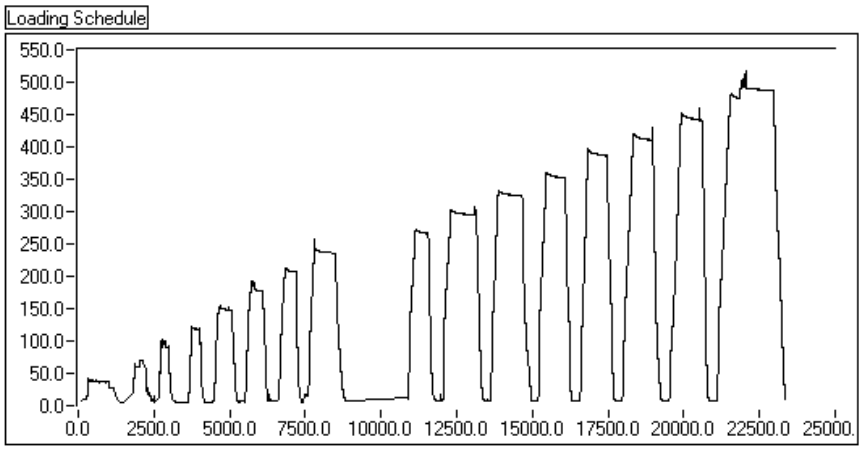

Figure 4.51 – Loading Schedule for G1ES

The plot of cumulative MARSE vs. load for G1ES is shown in Figure 4.52. Little emission occurs during load holds until about 270 kips. The Felicity Effect is prevalent throughout the test. Felicity Ratios were calculated using the same definition of 300 cumulative MARSE above the value at 10 kips, and are presented in Table 4.19. The Felicity Ratio begins at 0.76 and decreases rapidly, the same trend seen in G1WS.

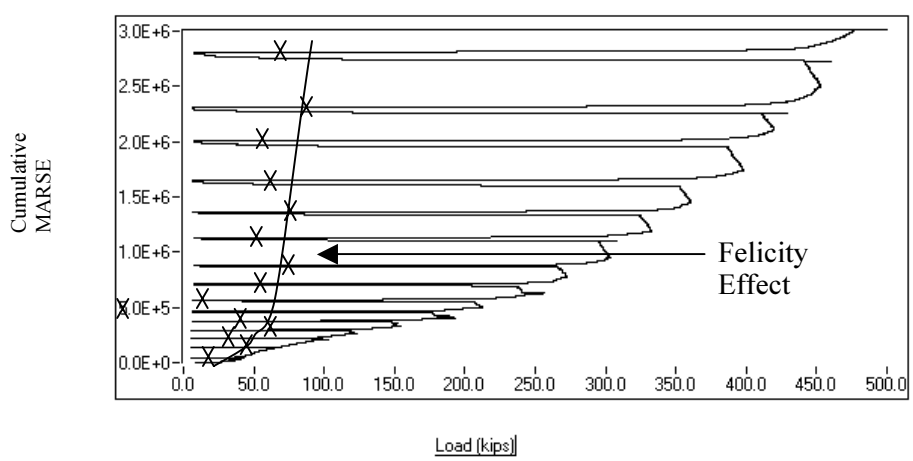

Figure 4.52 – Cumulative MARSE vs. Load for G1ES

Table 4.19 – Felicity Ratios for G1ES

Previous Load (kips)	Emission on Reload (kips)	Felicity Ratio	
43	33	0.76	
70	49	0.69	
102.5	41	0.40	
123	59	0.48	
154.5	42	0.27	
193	60	0.31	
212	17	0.08	
256.5	56	0.22	
272.5	77	0.28	
308	54	0.17	
333	77	0.23	
361	59	0.16	
398	49	0.12	
429	82	0.19	First Detected Crack
460	67	0.14	

The graph of Historic Index shows one large peak corresponding to the first detected crack, with a value of 168. In Figure 4.53, few high amplitude hits occur until approximately 270 kips, the same load where emission during load holds starts to increase.

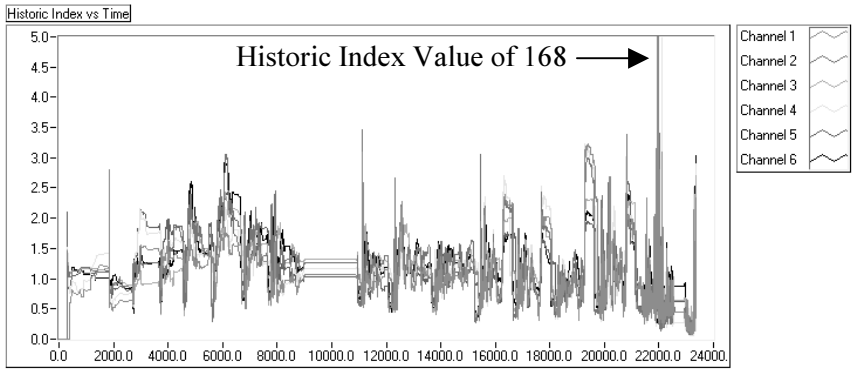

a) Historic Index Vs Time for G1ES

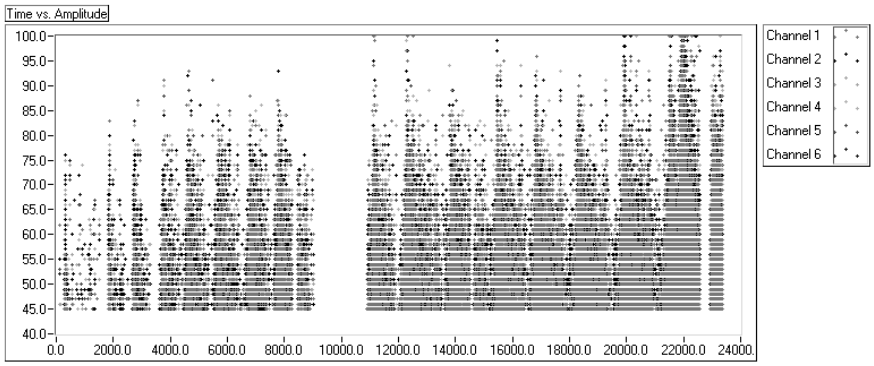

b) Amplitude vs Time for G1ES

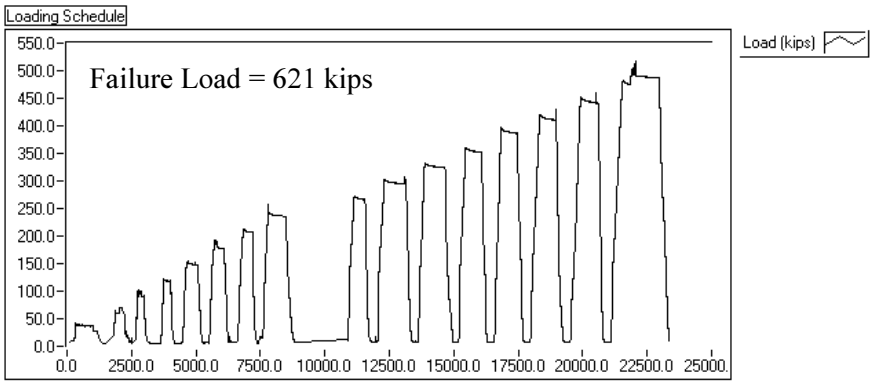

c) Load vs Time for G1ES

Figure 4.53 – Time Based Graphs for G1ES

4.6.3 Discussion of Shear-Dominated Tests on Type C Girders

Shear tests on Type C girders gave results similar to those on the box girder specimens. From the cumulative MARSE plots, it is seen that emission during load holds increases as damage increases. Also from the cumulative MARSE plot, Felicity Ratios can be extracted. From G2WS, it was discovered that the Felicity Ratios were quite large, and full unloading of the specimen was required to estimate them accurately. A graph comparing Felicity Ratios for the three shear specimens with full unloading cycles is

presented in Figure 4.54. A slightly different definition of the Felicity Ratio was used compared to the box girders, because of the increased difficulty in controlling the load with the hydraulic ram vs. the mechanical displacement-controlled testing frame. The slight change does not affect the results or conclusions. The Felicity Ratios show a dramatic difference between the girder with a low crack ratio (G2ES) and the two girders with the higher crack ratios (G1ES and G1WS).

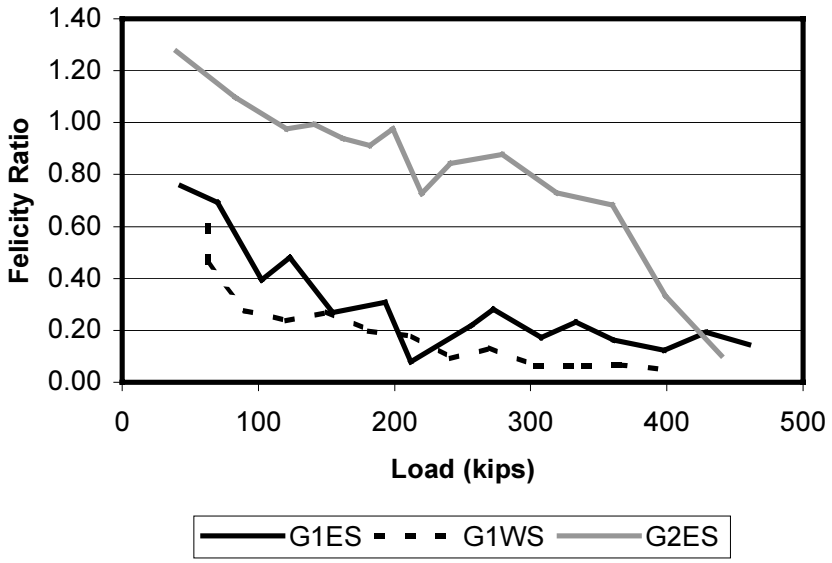

Figure 4.54 – Felicity Ratios for the Shear Tests on Type C Girders

Unlike the box girders, the magnitude of the hit amplitudes does not seem to be a good evaluation criterion. All specimens show similar trends regardless of damage.

Emission during load holds does not seem to be a good evaluation criterion either. There is little difference at load holds between the specimens with more deterioration and the one with little deterioration.

In these tests, the Historic Index seems to be a good indicator of cracking. Before cracking, it shows considerable scatter without very large peaks. It can be used, however to determine if a crack is due to loading or to opening of an existing crack.

4.7 DISCUSSION OF ACOUSTIC EMISSION TESTING AND EVALUATION CRITERIA

Acoustic emission shows considerable promise for evaluating distributed damage in prestressed concrete. In particular, Felicity Ratios are vastly different between the badly damaged specimens and less damaged ones, even at relatively low loads. Other potential evaluation parameters include the amount of emission, emission during load holds, and amplitude of hits.

From these tests, preliminary evaluation criteria were identified. Amount of emission and emission during load holds were not included as criteria, since the amount of emission depends on the geometry of the specimen, and emission during load holds depends on the length of time the load is held. The most promising evaluation criteria involve emission during unloading, Historic Index, amplitudes of hits, and the Felicity Ratio.

It was determined from the data that specimens should be loaded to at least 50% of the predicted cracking load, since at this level acoustic emission responses are distinct, and no additional damage is induced. The predicted cracking loads used in this analysis were 60 kips for the flexure tests, 200 kips for the shear

tests on box girders, and 450 kips for the shear tests on Type C girders. The following evaluation criteria relate to the behavior of the specimens at a load level of 50% of the cracking load.

- Emission during Unloading – The importance of this parameter was seen in BG4S, the specimen that failed in a bearing mode. If significant emission is seen during loading, the area being tested should be inspected for delaminations.
- Historic Index and Amplitude of Hits – A combination of a jump in the Historic Index and high amplitude hits are seen whenever a crack grows. If the Historic Index jumps 4 or more with hits of 90 dB or greater, it is probable that cracks are propagating.
- Felicity Ratio and Amplitude of Hits – Damage in a specimen was most closely related to the Felicity Ratio, and specimens with more damage show more high amplitude hits. A combination of these two parameters may be used to evaluate the amount of damage in a specimen. Suggested damage criteria for Felicity Ratios and hit amplitudes are presented in Table 4.20, and plotted against the results of the full-scale tests in Figure 4.55.

Table 4.20 – Suggested Evaluation Criteria for Distributed Damage

Damage Level	Felicity Ratio		Total Number of Hits above 85 dB
Minor	> 0.9	And	< 15
Intermediate	> 0.9	And	< 25 but > 15
		-Or-	
	> 0.6 but < 0.9	And	< 25
Severe	> 0.6	And	> 25
		-Or-	
	< 0.6		

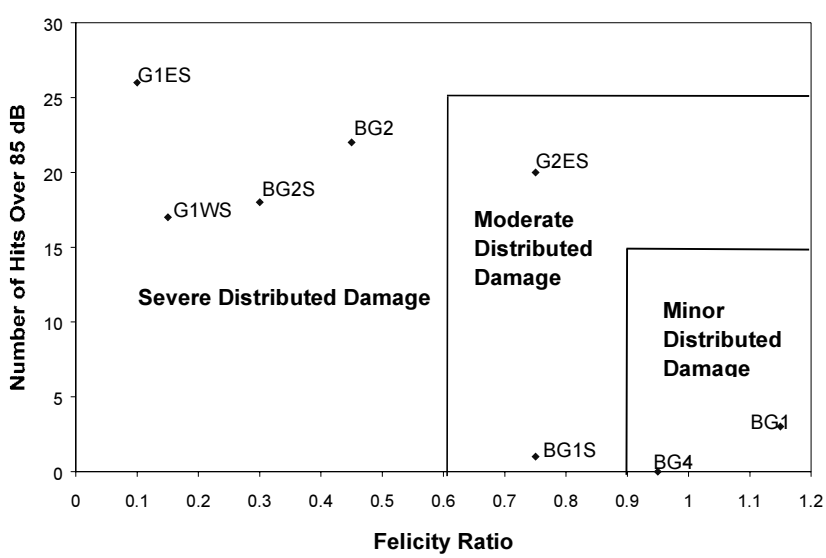

Figure 4.55 – Proposed Evaluation Criteria and Test Results

4.8 CONCLUSIONS FROM ACOUSTIC EMISSION TESTING

In prestressed concrete, distributed damage causes consistent changes in the acoustic emission response. Preliminary evaluation criteria are suggested based on emission during unloading, Historic Index, amplitudes of hits, and the Felicity Ratio. This method shows promise for quantifying distributed damage in prestressed concrete.

Acoustic emission has several advantages over other nondestructive tests. The main advantage is that it is global. One test can evaluate an entire structure quickly and effectively by placing sensors over the entire structure and stressing it sufficiently. Another advantage is that acoustic emission lends itself well to in-place monitoring. If background noise can be eliminated it may be possible to leave sensors on a bridge, continuously monitor normal traffic, and determine the increase in distributed damage. If a continuous monitoring program were not adopted, another less convenient solution would be to close the bridge and run equipment of known weight over it. Although this application was not researched as part of this report, the groundwork was laid for its possible future development.

Acoustic emission also has some drawbacks. One of the most significant drawbacks is that it is application specific. The results presented here apply only to prestressed concrete girders with loading conditions and sensor arrangements similar to those presented in this report. Also, as seen in BG4S, the loading method must stress the defect for detection. Another drawback is the high attenuation of acoustic emission in concrete. Although low-frequency sensors minimize this effect, it is still significant.

CHAPTER 5 – SHORT-PULSE RADAR

Short-Pulse Radar is a nondestructive test method that has been used successfully to find delaminations, reinforcement, layer thicknesses, and defects in concrete, pavement and soils. This chapter describes the method and summarizes experience in applying it to concrete with distributed damage.

5.1 INTRODUCTION TO SHORT PULSE RADAR

Short-Pulse Radar, sometimes referred to as Ground-Probing Radar (GPR), is based on reflections of electromagnetic energy from materials with different dielectric constants. It works like ultrasonic and pulse-echo methods, but uses electromagnetic energy rather than sound.

When electromagnetic energy encounters a boundary between two different materials, some is transmitted and the rest is reflected. How much is transmitted and how much is reflected depends on the relative values of the dielectric constants of the materials. The reflection coefficient at the interface of the two materials is given by:

$$\rho_{12} = \frac{\sqrt{e_{r1}} - \sqrt{e_{r2}}}{\sqrt{e_{r1}} + \sqrt{e_{r2}}} \qquad \text{(Eqn 5.1)}$$

where ρ_{12} is the reflection coefficient, and e_r is the dielectric constant relative to air for each material. Typical dielectric constants for various materials are shown in Table 5.1.

Table 5.1 – Typical Dielectric Constants for Various Materials

Material	Approximate Relative Dielectric Constant At 25 C
Clay Soil (Dry)	2.5
Air	1
Concrete	6
Styrofoam	1.03
Water	78
Steel	∞

The velocity with which the electromagnetic wave travels through a substance depends on the dielectric constant and is calculated as shown below:

$$V = \frac{C}{\sqrt{e_r}} \qquad \text{(Eqn 5.2)}$$

where C is the speed of light and V is the velocity of the wave though the material with relative dielectric constant e_r. As shown in Figure 5.1, an incident wave is introduced from the antenna. At the boundary between Medium 1 and Medium 2, some of the energy is transmitted and the rest is reflected back. The same thing happens at the boundary between Medium 2 and Medium 3. By recording the time between reflections, the thickness of Medium 2 can be calculated.

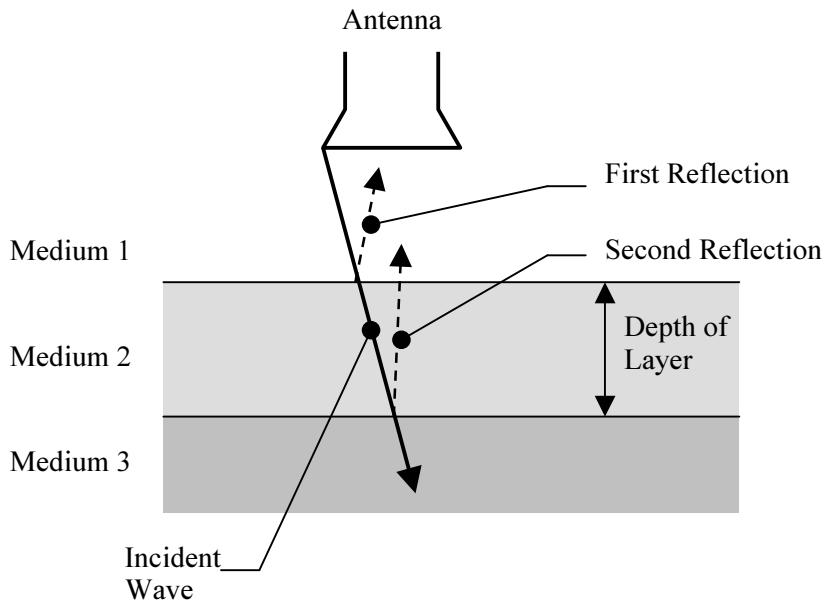

Figure 5.1 – Propagation of Electromagnetic Waves through Media of Different Dielectric Constants

Radar systems are set up with a "pitch-catch" antenna housing both an emitter and a receiver. The antenna emits a signal, pauses to pick up the reflections, and then emits a new signal. This happens at high speed, creating an almost continuous scan.

For evaluation purposes, each signal (A-Scan) is plotted next to the previous one creating a color-coded chart called a B-Scan. Figure 5.2 demonstrates this more clearly. On the left side of Figure 5.2 is one received signal, or A-Scan. In this area, there are 2 small colored lines, a pink one and a green one. Any signal to the right of the green line will be shown green in the B-Scan, and any signal to the left of the pink line will be represented as pink in the B-Scan. Between these two lines, the color changes accordingly. In essence, A-Scans are color-coded and plotted next to each other to create a B-Scan, shown to the right of the A-Scan. Differences in the signal, and the corresponding discontinuities in the specimen, are easier to see on the B-Scan than on the A-Scan.

5.2 TEST SETUP

Pulse Radar, Inc. (Houston, Texas) was contracted to perform a short-pulse radar survey on the box girder specimens at Ferguson Laboratory. Their equipment consisted of a 1 GigaHertz center frequency antenna with a high-speed data acquisition computer and a wheel mounted encoder to measure distance (Figure 5.3). Because the antenna covered about half the depth of the beam, two passes were required to monitor the entire side of the girder.

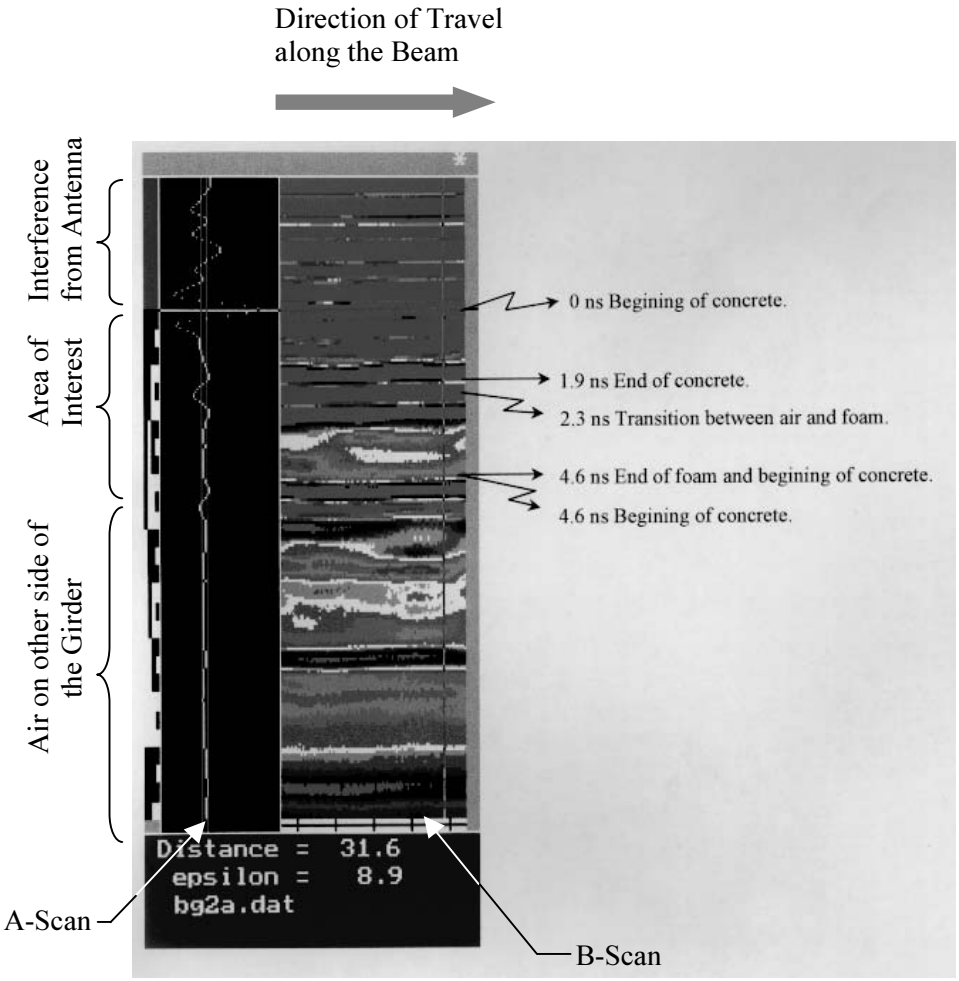

Figure 5.2 – Typical A-Scan and B-Scan from Sample BG2

Figure 5.3 – Short Pulse Radar Equipment

Since microwaves reflect only at a change in dielectric constant, short-pulse radar cannot detect closed cracks. Although it was anticipated that it would be difficult to identify the individual cracks, it was postulated that distributed cracking could affect the overall dielectric constant, and that this change in dielectric constant would be detected by the reflection of electromagnetic energy and by changes in the velocity of the wave in the concrete.

To test this hypothesis, two different specimens were tested: the girder with bad end damage (BG2); and the girder that was continuously soaked with water (BG4). BG2 was chosen because the damage at its ends was significantly worse than at other places along its length, which should cause a variation of dielectric constants between the ends and other areas. The continuously soaked girder was chosen because it had a variation of damage along the length, and was wet at the time of test. It was hoped that water, which has a much higher dielectric constant than concrete, would soak into the cracks, creating a much larger change in dielectric constant between the badly damaged areas and the less damaged ones. As can be seen in the table of typical dielectric constants, if air fills the cracks, the dielectric constant should decrease; if water fills them, the dielectric constant should increase.

Francisco Alvarez (Pulse Radar, Inc.) completed the testing along with researchers Brian Tinkey and Anna Boenig. The complete west side and southeast side of girder BG2 were scanned along the bottom and top of the girder. The northeast side was not scanned due to access problems. On BG4, only the bottom half of the west side was tested due to the location of the girder. Results are presented in the next section.

5.3 RESULTS OF THE SHORT PULSE RADAR SURVEY

Pulse Radar, Inc. completed the analysis and issued a report to The University of Texas at Austin, along with all the data files and software required for further review. Figures 5.4 though 5.6, taken from that report, provide a brief summary of their findings.

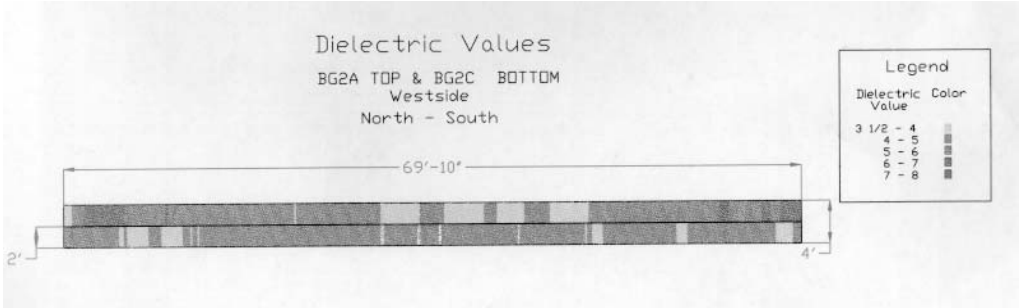

Figure 5.4 – Dielectric Values on West Side of BG2

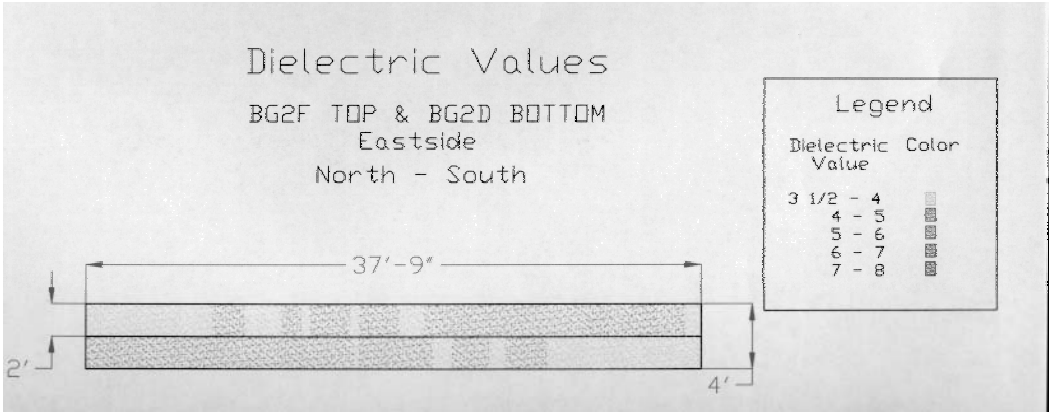

Figure 5.5 – Dielectric Values on East Side of BG2 at the A-End

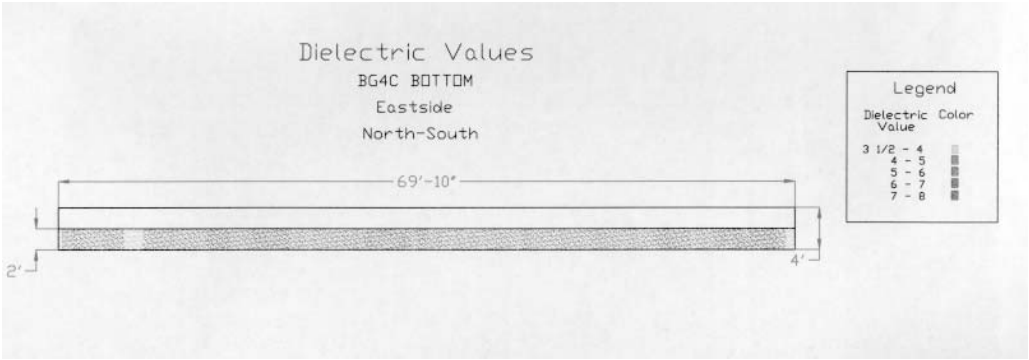

Figure 5.6 – Dielectric Values on the East Side of BG4

An independent review of the data at The University of Texas did not discover any other significant results.

5.4 DISCUSSION

It can be seen from Figures 5.4 and 5.5 that while dielectric values do vary along the length of BG2, this variation seems random and does not correlate with observed damage.

Interestingly, the dielectric values for BG4 are considerably higher than for BG2. This was expected because it was saturated with water at the time of testing.

Assuming that a difference in dielectric constants could be determined, this method has other difficulties. The first difficulty is accessibility. The antenna for the short pulse radar is quite large and requires sufficient space between the girders. Another difficulty is that this method would give an average dielectric constant over the depth, so that variations in deterioration within the width would not be detectable. Finally, data interpretation can be complicated and should only be done by experienced individuals.

5.5 CONCLUSION

Although short-pulse radar may be able to detect distributed damage, that hypothesis was not demonstrated here. At this time, short-pulse radar is unable to reliably distinguish the variation in amount of cracking. Although it can be successfully used to locate inclusions, delaminations, and other larger defects accurately and quickly, the detection of small, distributed cracks seems beyond its capacity. Much more research and development must be undertaken to make this method useful.

CHAPTER 6 – IMPACT-ECHO

6.1 INTRODUCTION TO IMPACT-ECHO

Impact-Echo is a nondestructive test method based on the propagation of a stress wave through concrete. An impact, usually caused by a small steel ball, is made on the surface, sending a pressure wave into the concrete. This wave is then reflected off the back surface or a defect. By analyzing the frequency of the reflected waves along with their known wave speed in concrete, it is possible to determine the depth to the back surface or the defect.

Impact-echo is preferred over ultrasonics for concrete due to the high attenuation of ultrasound in concrete. Since the aggregate in concrete is rather large compared to the wavelength of ultrasound, it is difficult to generate a large enough pulse with a piezoelectric sensor that will not attenuate quickly and will make the concrete appear homogeneous.

Figure 6.1 shows a schematic representation of a typical impact-echo test. Three types of waves are generated from the surface impact. The R-wave, or Rayleigh wave, is a surface wave that usually passes the transducer only once. The S-wave, or shear wave, has a maximum amplitude at 45 degrees from the impact and therefore travels away from the point of impact causing very little displacement at the sensor when reflected off the back wall. In contrast, the P-wave or compression wave has maximum amplitude at the center and will have the most influence on a transducer placed near the point of impact.

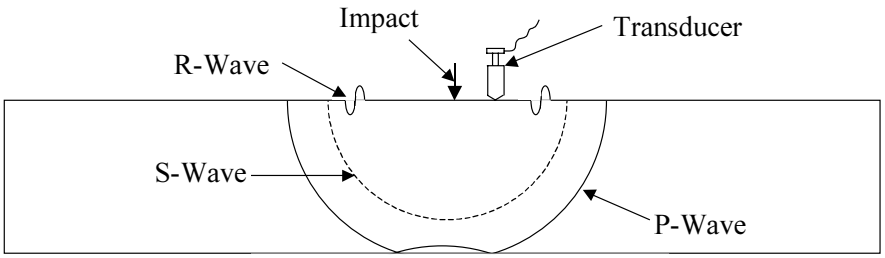

Figure 6.1 – Schematic Representation of Impact-Echo Test

The impact is normally caused by a steel ball tapped lightly against the surface. The required diameter of the ball depends on the depth of concrete and the minimum size of a significant defect. A larger ball produces a higher energy pulse that can detect flaws deeper in the specimen, but may not detect defects that are smaller or closer to the surface.

A typical displacement history from an impact-echo test on a 125 mm thick web is shown in Figure 6.2. The first part of the wave is the surface wave, or R-wave. Since this wave travels on the surface, if the test point is not near an edge the R-wave will not be detected again. The peaks after the initial R-waves are returns of the compression, or P-wave. Also shown in Figure 6.2 is the time difference, ΔT, between successive peaks. This corresponds to the time that it takes the P-wave to travel through the specimen, reflect off the back wall and return to the surface. These reflections create a periodic waveform. If the velocity and the time between peaks is known, the depth can be easily calculated.

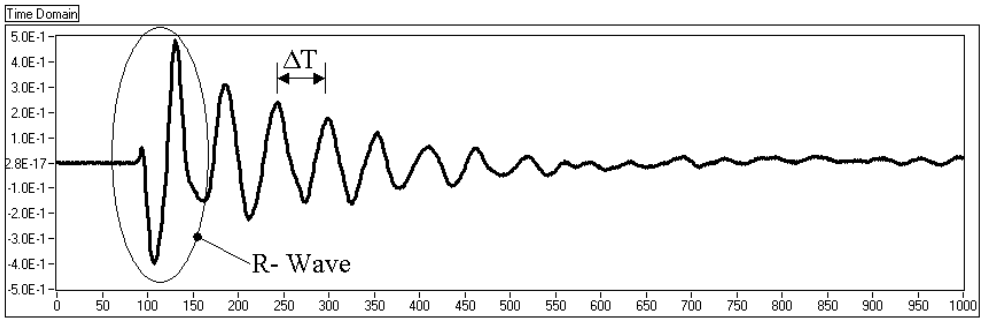

Figure 6.2 – Typical Displacement History for an Impact-Echo Test

If a defect is present in the specimen, the P-wave will reflect off both the defect and the back wall, complicating the displacement plot. It is nearly always difficult in practice to read the time between peaks directly from the plot since there are reflections from reinforcement, defects, sides, and voids. To solve this problem, a Fast Fourier Transform is used to transform the displacement history from the time domain to the frequency domain. Peaks on the frequency spectrum correspond to the dominant frequencies in the wave. Figure 6.3 is the frequency spectrum for the waveform shown previously in the time domain in Figure 6.2. Since this was from a solid specimen, there is only one peak, corresponding to the thickness of the web. If a defect were present in the sample, there would be two frequency peaks; one for the defect and the other for the back wall.

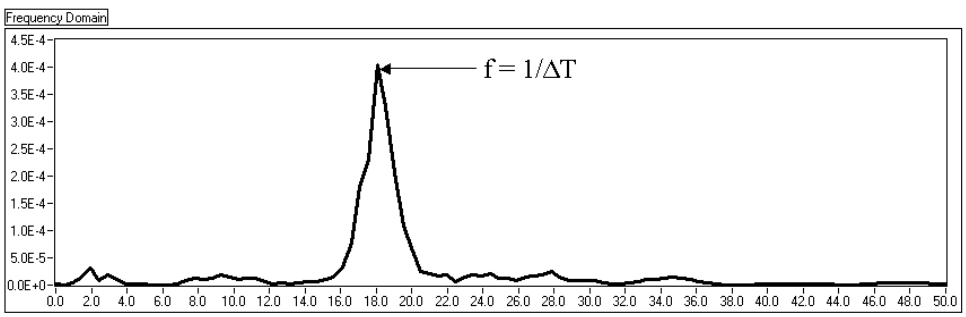

Figure 6.3 – Frequency Spectrum of a Typical Impact-Echo Test

Once the dominant frequencies are determined, the thickness corresponding to those frequencies can be determined (Kesner 1997):

$$d = \frac{C_p}{2f} \qquad \text{(Eqn 6.1)}$$

Where:

d = Depth

C_p = P-wave speed in concrete (Typically 4000 m/s)

f = Frequency

One of the major problems with impact-echo is that it is hard to apply to specimens with complicated geometry. The previous discussion has been limited to flat plates. When a specimen has a different geometry, however, complications arise such as reflections from sides or surface breaking cracks.

Despite this, impact-echo has been very successful in locating delaminations, voids, honeycombing, and other defects quickly and accurately (Malhotra and Carino 1991).

6.2 APPLICATION OF IMPACT-ECHO TO CONCRETE WITH DISTRIBUTED DAMAGE

Research was completed at Cornell University on applying impact-echo to concrete with distributed damage (Kesner 1997). A different type of analysis is required for concrete with distributed damage because instead of a discrete flaw, an overall degradation of the concrete must be detected. A method was proposed to quantify the amount of damage by monitoring how quickly the P-wave attenuates.

As a compression wave (P-wave) travels through concrete, some of its energy is lost due to scattering from voids, microcracks, and aggregate. When concrete cracks due to premature concrete deterioration, the scattering increases, causing more rapid attenuation. By quantifying how quickly the compression wave attenuates, it should be possible to quantify distributed damage in the concrete.

Kesner (1997) used finite element models to determine the theoretical response to a distributed damage. To model distributed cracking, some elements in the model were "softened" by lowering their modulus of elasticity. Analytically the P-wave attenuated by scattering at the interfaces between the softer elements and the normal elements. The resulting displacement histories from simulated impact-echo tests on these models were then filtered by a high-pass Butterworth filter with a 10 kHz cutoff to eliminate the low frequency components. This allowed for clear compression wave peaks and a more pronounced decay of the wave. Four major results were discovered from these models as damage increased:

1. the dominant frequency decreased;
2. the apparent wave velocity decreased;
3. the number of discernable P-wave decreased; and
4. the attenuation rate increased;

To quantify the rate of attenuation, a decay coefficient was defined by fitting an exponential decay function to the peaks of the successive P-wave arrivals. This function takes the form:

$$I = I_o \exp^{(-\alpha t)} \qquad \text{(Eqn 6.2)}$$

In the above equation, α is the rate of attenuation and is used to quantify the damage. An example of this process is shown in Figure 6.4.

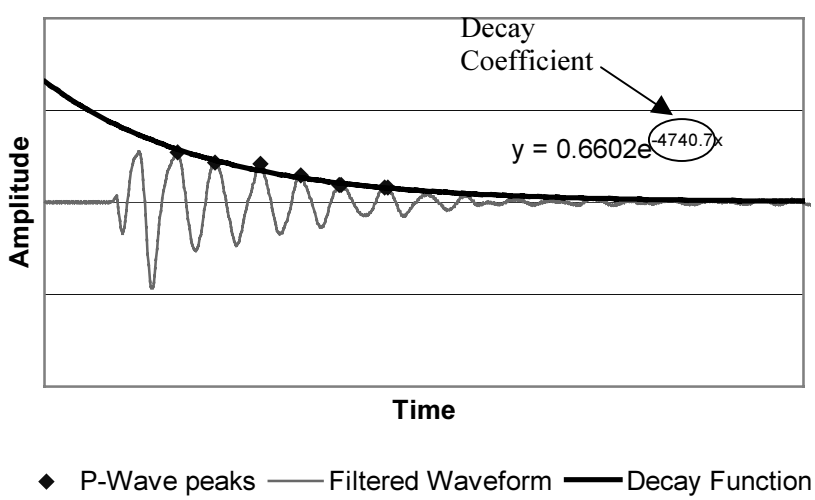

Figure 6.4 – Calculation of the Decay Coefficient

Results from the finite element models of Kesner (1997) are summarized in Table 6.1. As damage level increases, the number of P-wave arrivals decreases and the decay coefficient increases.

Table 6.1 – Results of Finite Element Models for 130 mm Thick Concrete Plate (Kesner 1997)

Damage Level	No. of P-wave Arrivals	Decay Constant
Little or None	13 or More	Less than 3100
Minimal	13 to 11	3100 to 4000
Moderate	11 to 10	4000 to 5000
Severe	9 or Less	Greater than 5000

The method described above was also applied by Kesner (1997) in a field test on box girders from the same group described in Chapter 2. Results from those tests were consistent with the finite element simulations. Sections with little to no damage had 17 to 24 discernible P-waves and decay coefficients of 1700 and 2030. A beam with moderate damage had 12 P-wave peaks with a decay coefficient of 4550. Finally, a heavily damaged specimen had a decay of 11600 using 4 P-wave arrivals, and 8950 using 6 P-wave arrivals.

6.3 TESTING PROGRAM

Impact-echo testing was performed at The University of Texas at Austin to evaluate the results presented in the previous section, and to explore the overall value of the impact-echo method to members with distributed damage. Two results from the Cornell study – reduction in dominant frequency and in apparent wave velocity – were not investigated since they were most likely due to the method of modeling attenuation. Because wave speed is related to the modulus of elasticity, "softening" elements would naturally decrease the wave speed and the dominant frequency. The major conclusions of the Cornell study, however (the number of discernable P-wave peaks and the decay coefficient), were investigated at The University of Texas at Austin.

Specimens BG1 and BG3 were tested at Ferguson Laboratory and analyzed to find their decay constants. These girders are described in Chapters 2 and 3. Both were from the same set of girders that were tested in the Cornell study (Section 6.2). In view of this, differences in geometry are not a factor. Since the testing at The University of Texas at Austin was performed after the Cornell testing, the girders would have had about 4 more years to deteriorate further, and should therefore have been in worse condition.

As discussed in Chapter 3, BG1 was a control girder with the least amount of cracking of any of the girders tested. Impact-echo tests were performed in areas of that girder that appeared visually to be in good condition. Although this girder had little damage compared to the others, it was not damage-free. Data were taken 5 feet from the south end, 7 feet from the south end, and 8 feet from the centerline. These areas were chosen since the visible damage there was small, clear P-wave peaks could be found on the waveform, and the test indicated that the thickness was close to the expected 127 mm, indicating solid concrete. Figures 6.5 and Figure 6.6 show the damage. The tested areas have light spider-web cracking, but no major cracks.

For comparison, tests were also conducted on BG3, the specimen with damage along its length. This specimen was chosen for its extensive spider-web cracking and lack of many large cracks. Tests were performed on this girder 3 feet from the north end and 22 feet from the south end. The point 3 feet from the north end is shown in Figure 6.7. There is extensive cracking on the left hand side as well as above the test point. The other testing point on BG3 is shown in Figure 6.8. Although there were no cracks in the immediate area, there were some in the web on the left side.

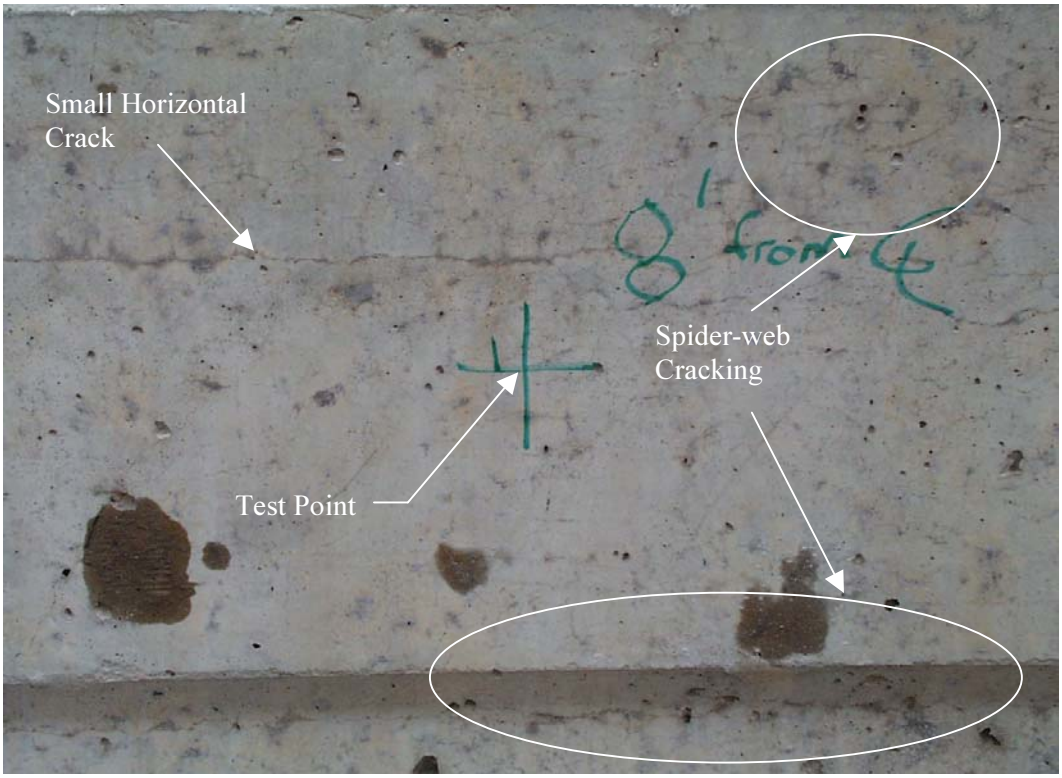

Figure 6.5 – Photo of the Test Point 8 feet from Centerline on BG1

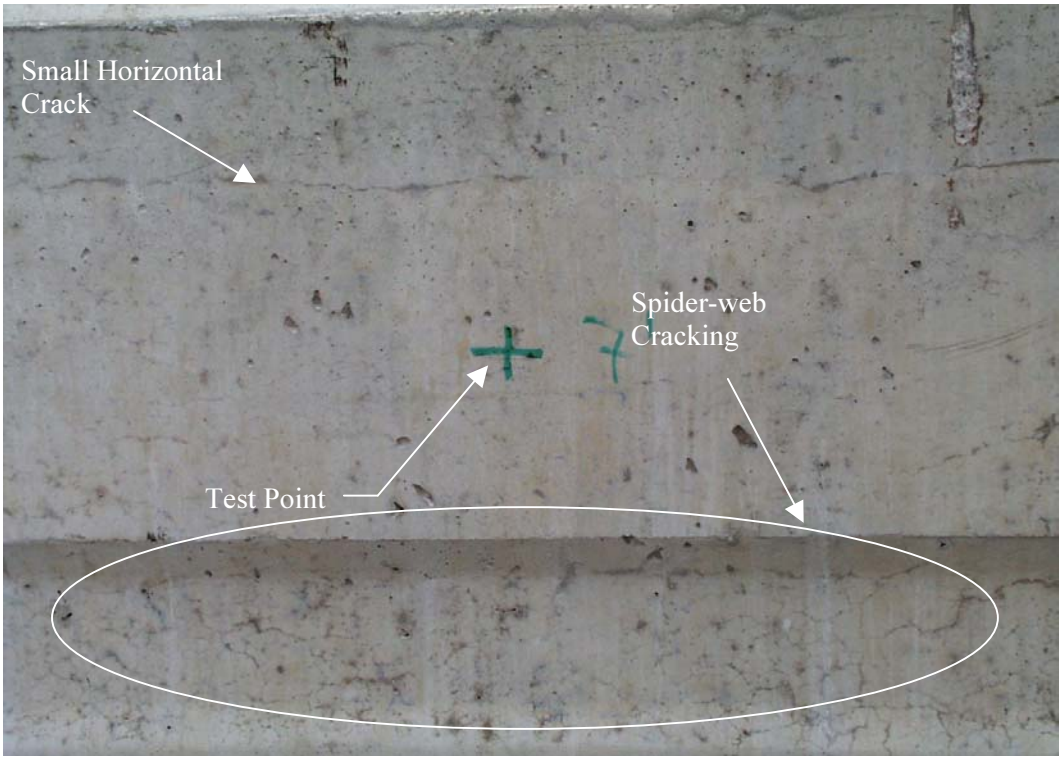

Figure 6.6 – Photo of the Test Point 7 feet from the South End of BG1

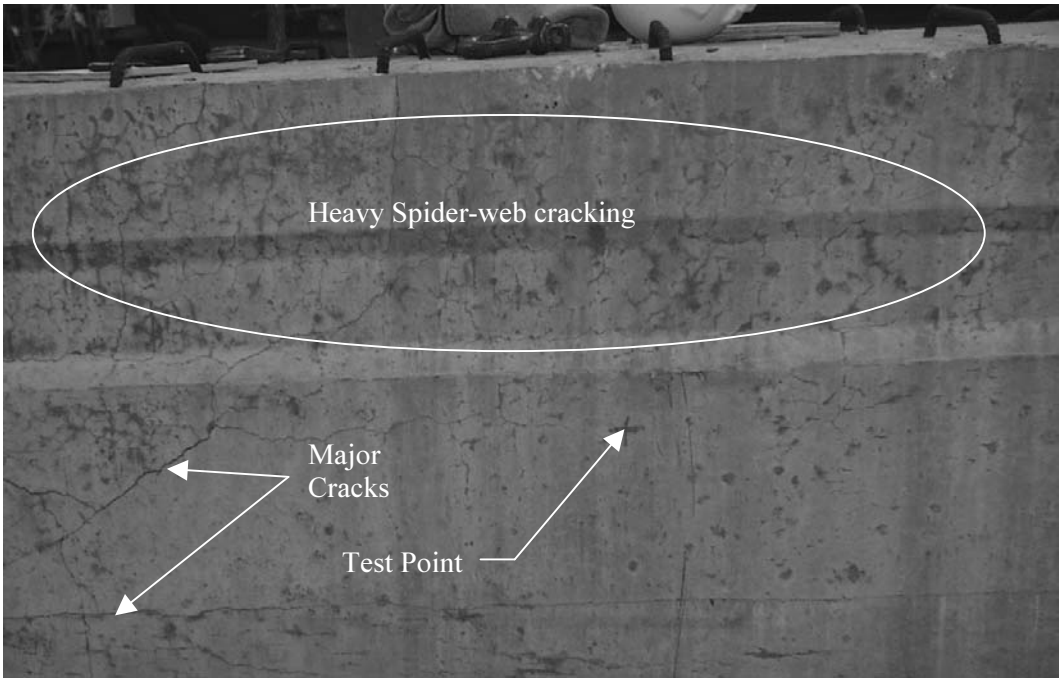

Figure 6.7 – Photo of the Test Point 3 feet from the North End of BG3

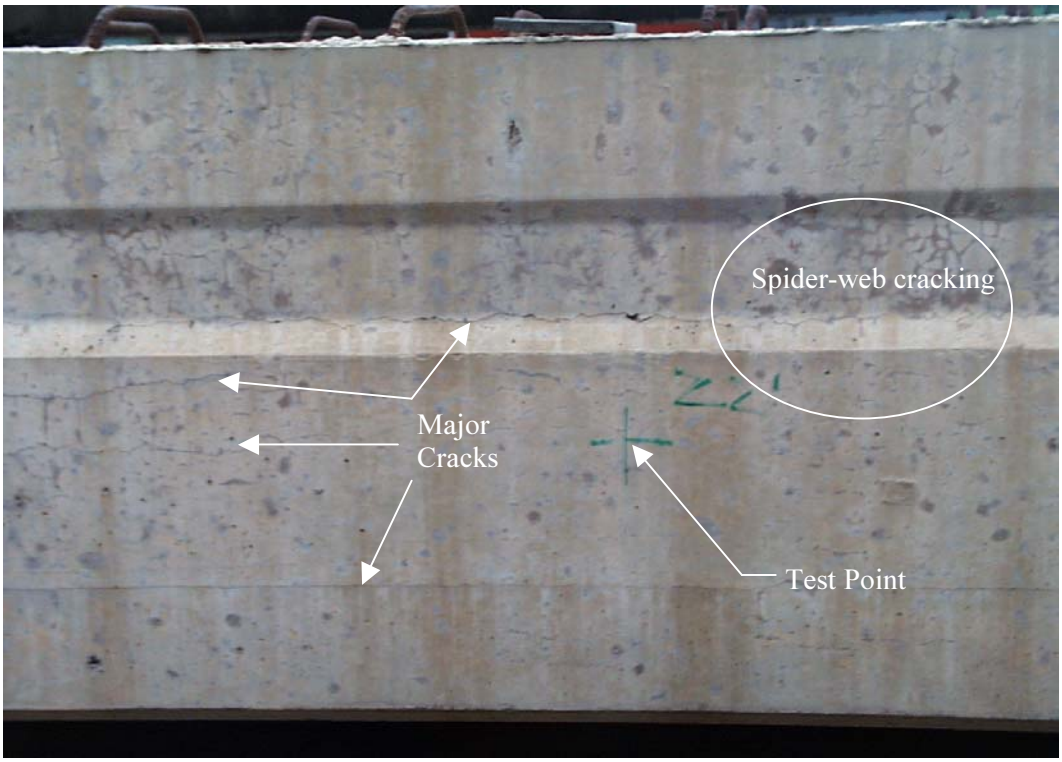

Figure 6.8 – Photo of the Test Point 22 feet from the South End of BG3

Data were collected with the DOCtor impact-echo equipment and VIKING software from Germann Instruments, Inc (Figure 6.9). Once data were collected, the waveforms were converted to an ASCII file for further analysis.

Figure 6.9 – Photo of DOCtor Impact-Echo Equipment

The displacement history for each test was filtered using a high-pass, 5th-order Butterworth filter in LabView. As suggested, a 10 kHz cutoff frequency was used. An unfiltered waveform and its resulting frequency spectrum are shown in Figure 6.10. Low-frequency elements were not as prevalent in the actual tests as in the finite-element simulations. The filter did make slight difference, however, and was used for all tests. The same test, filtered, is shown in Figure 6.11. Frequencies under 10 kHz are removed.

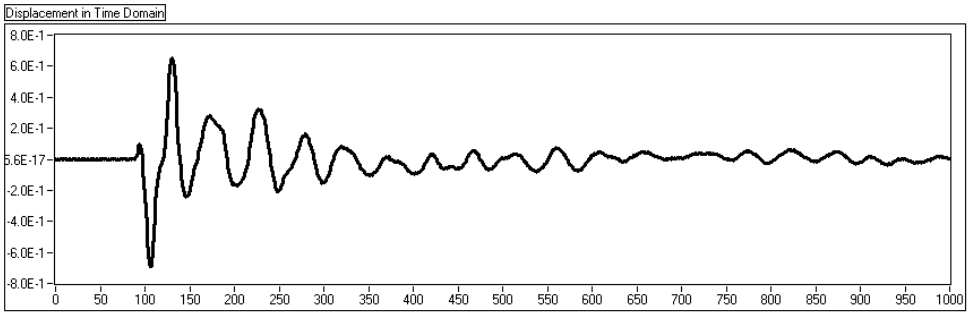

(a)

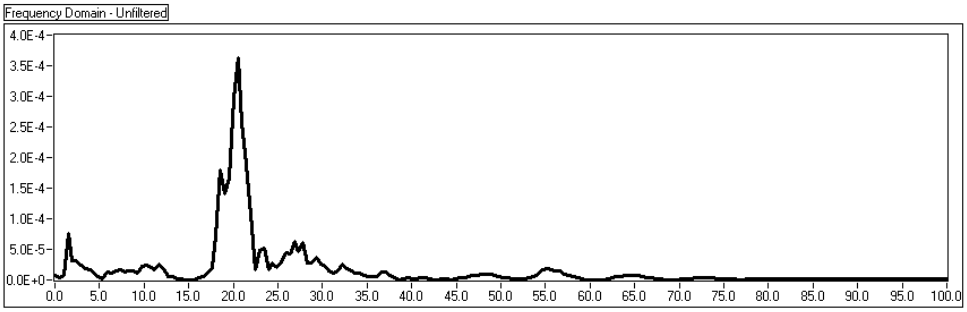

(b)

Figure 6.10 – (a) Unfiltered Displacement History in Time Domain (b) Unfiltered Frequency Spectrum

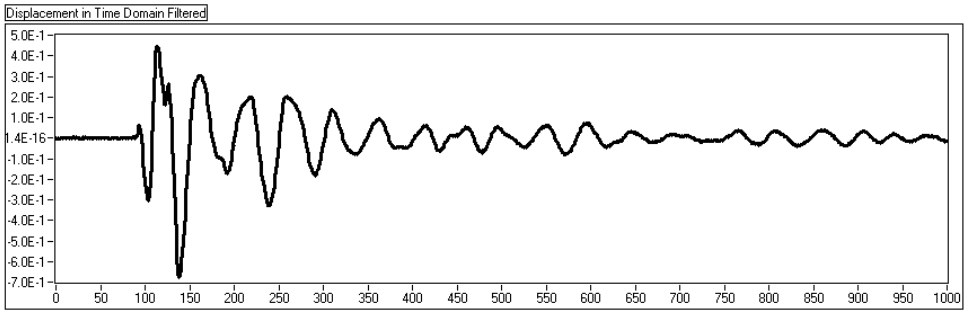

(a)

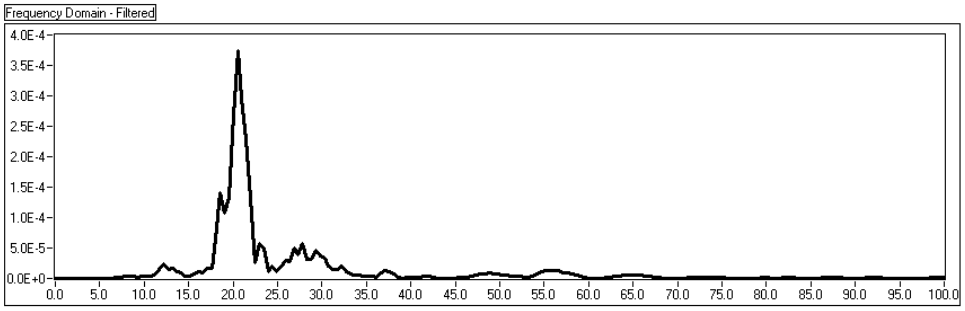

(b)

Figure 6.11 – (a) Filtered Displacement History in Time Domain (b) Filtered Frequency Spectrum

A summary of the procedure used in this analysis is outlined below:

1. Perform impact-echo test.
2. Convert the waveform to an ASCII file.
3. Filter out low frequencies using a Butterworth filter (this can be done easily in programs such as LabView or MatLab).
4. Plot the filtered displacement history and identify the peaks.
5. Use regression analysis to fit an exponential attenuation curve to the peaks.

6.4 RESULTS

Two tests were performed at each location on BG1, for a total of 6 tests. The filtered waveforms, the peaks used to fit the decay function, and the best-fit decay function are given in Appendix B. Fewer clear peaks were available than in the Cornell research. Instead of the 17 to 24 peaks available to calculate the decay constant, 4 to 7 peaks were used. Results are summarized in Table 6.2.

Table 6.2 – Results of Impact-Echo Tests on BG1

Sample Location	Test Number	No of Peaks Used	Decay Constant
8 feet from Centerline	1	4	5957
	2	6	4741
7 feet from South End	1	5	4910
	2	5	2891
5 feet from South End	1	6	3035
	2	7	3211
Average		5.5	4124

BG3 had considerably more damage than BG1 and was tested for comparison. Again, two tests were conducted per point, for a total of 4 tests. Plots displaying the filtered waveforms, the peaks used to fit the decay function, and the best-fit decay function are given in Appendix B. For the worst samples, no more than 5 peaks in any waveform were used to calculate the decay constant. Although the damage appeared visibly worse near the end of the girder, the decay constant was lower there. The results are summarized in Table 6.3.

Table 6.3 – Results of Impact-Echo Tests on BG3

Sample Location	Test Number	No of Peaks Used	Decay Constant
22 feet from South End	1	4	7316
	2	4	8274
3 feet from North End	1	5	5480
	2	4	5031
Average		4.25	6525

6.5 DISCUSSION OF IMPACT ECHO RESULTS

The impact-echo method clearly shows promise for quantifying the amount of distributed damage. Difficulties need to be resolved, however before the method can be used reliably for that purpose.

The most striking difficulty was choosing the P-wave peaks. It is difficult to choose how many peaks in the waveform should be skipped to account for the R-wave, and how far the P-wave arrivals can be distinguished. The R-wave arrives at the beginning of the displacement history, and should not be included when calculating the decay constant. It is sometimes difficult to distinguish, though, where the surface wave ends and the P-wave arrivals begin. In this analysis, two peaks were skipped to account for the surface wave. If only one peak had been skipped, however, the attenuation constants would have changed greatly. Increasing the number of peaks for the same displacement history would decrease the decay constant. It is often difficult, however, to use the same number of points in each waveform.

As discussed above, the value of the decay constant could vary greatly depending on how many and which peaks were chosen. To illustrate this, a test from BG3 with many easily discernable peaks was analyzed using a variety of peaks. The results are presented in Table 6.4. Calculated decay constants range from 3000 to 10000, depending on the P-wave arrivals that were chosen.

Table 6.4 – Decay Constants for a Test Performed on BG3

	Decay Constant	
Number of Peaks	If 2 Peaks are Skipped for R-Wave	If 1 Peak is Skipped for R-Wave
3	8185	9753
4	5032	8461
5	4040	6209
6	3210	5129
7	3145	4219
8	3678	3957
9	3423	4018
10	3240	3807
11	3319	3606
12	N/A	3639

Another difficulty is the possibility of reflections from sides or surface cracks. If the point being tested is close to a geometrical discontinuity, the reflected waves can become very complex, creating difficulty in identifying successive P-wave arrivals. Thus, impact-echo lends itself best to plate-like specimens such as girder webs. If girder flanges are to be tested, where prestressing strand might debond, the geometry makes the analysis very difficult.

There are a few possible ways to improve the impact-echo method. One way is to average the peaks of many tests to get a more accurate decay curve. The data in Appendix B commonly show interference in the signal, causing a variation in peak height in the displacement history. If several tests were performed at one point and the signals were combined, interference from one test would not significantly affect the results.

Since the impact-echo method is concerned only with peaks from reflections from the backwall, another possible method of improving the results would be to use a bandpass filter around the dominant frequency

to eliminate any interference. Results from a 5th-order Butterworth bandpass filter are shown in Figure 6.12. The significance of the R-wave is decreased, and the subsequent P-wave peaks are larger and easier to identify. Even when using these techniques, however, it is still necessary to determine how many peaks should be chosen.

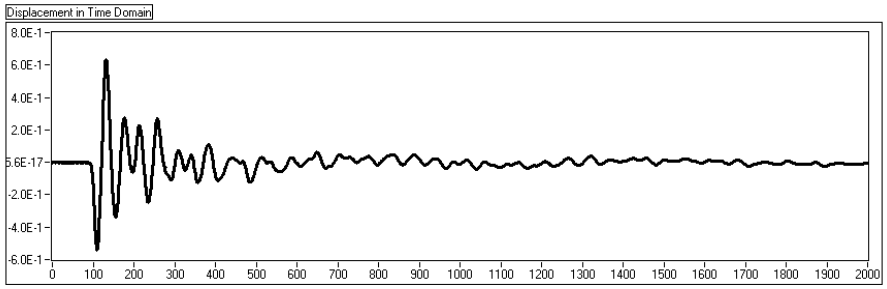

Unfiltered Signal

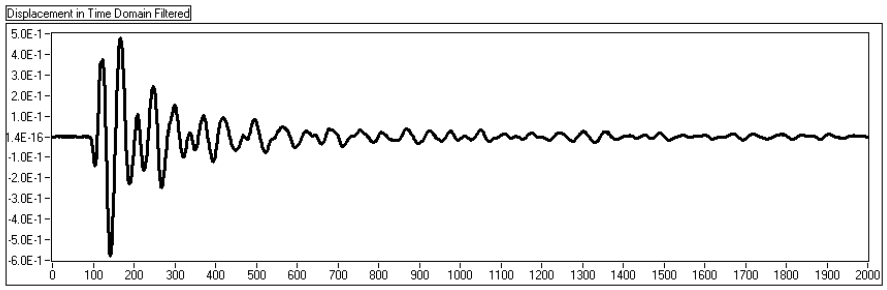

10 kHz Highpass Filter

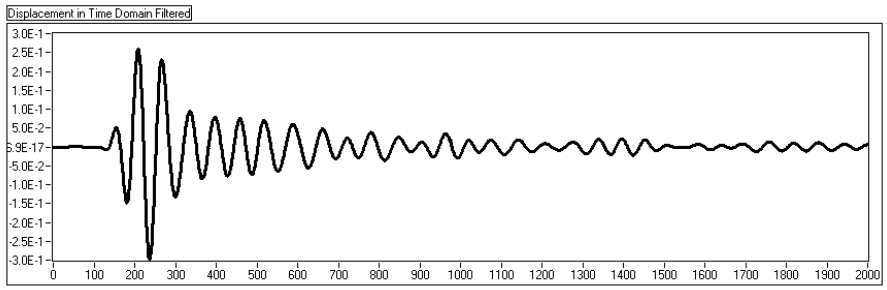

10 kHz to 20 kHz Bandpass Filter

Figure 6.12 – Results of Filtering the Displacement History

6.6 CONCLUSIONS REGARDING IMPACT-ECHO

Although the impact-echo method can in theory be used to detect distributed damage in concrete, it is difficult to apply to field specimens at this time. The current procedure of fitting a decay curve can be easily biased by the method of picking the P-wave peaks. If the difficulty of picking P-wave arrivals were solved and a correlation with the decay constant were still present, impact-echo would be valuable. Setup is quick, and many points can be tested quickly. In addition, if the distributed cracking has created a delamination, its size and shape could be determined easily.

Difficulties with the impact-echo method include the fact that it is a local test, developed for flat plates. If many boundaries are present near the test point, analysis of the data becomes quite difficult.

CHAPTER 7 – SUMMARY AND CONCLUSIONS

A study and literature review was performed to evaluate the use of four different nondestructive testing methods on prestressed bridge girders with a combination of delayed ettringite formation and alkali silica reaction. The methods were visual inspection, acoustic emission, short pulse radar, and impact echo.

7.1 VISUAL INSPECTION

Using a tape measure and a crack comparator, visual inspection was performed on all of the full-scale test specimens.

Visual inspection provided a good initial evaluation tool, since it could distinguish between the girders with varying degrees of damage. It is inexpensive and requires very little specialized equipment. However it can indicate only surface damage, it is operator-dependent, it is limited to easily accessible areas, and it is greatly affected by surface obstructions such as paint or stains.

Visual inspection can give a good qualitative indication of the degree of damage, and with the aid of crack indices (such as crack ratios), it can give a rough estimation of the progression of surface cracks. Visual inspection should be used along with another nondestructive test method.

7.2 ACOUSTIC EMISSION

Acoustic emission testing was performed on prestressed concrete girders with a wide range of damage. In total, ten tests were monitored on box and Type C sections under both shear and flexure.

Acoustic emission shows promise for quantifying distributed damage in a specimen. Based on this study, preliminary evaluation criteria are proposed (Section 4.7) using the emission during unloading, historic index, amplitude of hits, and the Felicity Ratio. Emission during unloading was related to delaminations; historic index and high amplitude hits were related to crack growth; and the Felicity Ratio and high amplitude hits could be correlated to damage.

Acoustic emission can inspect a large area of the bridge at one time and it lends itself well to in-place monitoring. Its drawbacks include:

i) the need to stress a defect enough for it to be detected. This is not normally a problem since a structurally significant defect will be stressed;

ii) the high attenuation of acoustic emission in concrete, which creates a need for many sensors;

iii) the need for road closures if a continuous monitoring program is not adopted.

If practical issues such as background noise from the traffic, protection of sensors and environmentally-induced emission from rain or freezing can be resolved, acoustic emission would be ideal for monitoring the increase of distributed damage.

Acoustic emission should be investigated further by verifying the laboratory results with field tests and determining the level and significance of background noise.

7.3 SHORT-PULSE RADAR

Short-pulse radar was used to examine two different box girders and thereby determine if differences could be seen between the varying degrees in damage along their length. One specimen was wet when testing so that water would fill the cracks and increase the dielectric constant; the other specimen was left dry to see if the air in the cracks would lower the dielectric constant.

Results from this testing did not show that this method could accurately gage the amount of damage at this time. Although a variation of dielectric constants was seen, it did not correlate with the areas of increased damage.

If in the future this method were able to determine the amount of distributed damage, it would have the advantage of speed. Since electromagnetic waves are airborne, no attachments to the girder are required, and results are very rapid.

Short-pulse radar should not be used to quantify the amount of distributed damage in concrete until more research is completed.

7.4 IMPACT ECHO

Impact-echo testing was performed on the webs of two box girders with different amounts of deterioration. Data from these tests were analyzed as proposed by Kesner (1997) to determine if the amount of distributed cracking could be determined by P-wave attenuation.

Results presented in this report, while encouraging, were found to be easily biased. The proposed method involves choosing the peaks of the returning P-waves and fitting an exponential curve to them in order to measure attenuation. The number of returning P-waves included in the regression could greatly change the results. In addition, it was sometimes difficult to distinguish the peaks of the P-waves due to interference from other reflections.

If a standard and reliable method of picking the P-wave peaks were found, the impact-echo method would be a valuable tool. The test is quick to set up and perform, but can determine the condition of the concrete only at the point where that the test is performed.

Research should be performed to standardize the method of choosing the P-wave arrivals before the test is used in the field. This process could possibly be helped by using a bandpass filter to isolate the frequency of interest and by combining multiple tests at the same point to eliminate the interference that might occur in any single test. The effectiveness of these suggestions was not determined.

7.5 CONCLUSIONS AND RECOMMENDATIONS

A summary of the major conclusions and recommendations that were arrived at through this study are listed below.

- Visual inspection provides a good qualitative evaluation and should be performed before any other tests are conducted.
- Acoustic emission shows promise for evaluating the amount of distributed damage in concrete.
- Evaluation criteria for acoustic emission on prestressed girders with distributed damage were proposed and should be verified with field tests.
- Short-pulse radar did not demonstrate the ability of detecting distributed damage.
- Impact-echo testing was encouraging, however somewhat subjective.
- A more standard procedure for impact-echo testing should be further researched before implementation.
- Other nondestructive tests that were not discussed, such as ultrasonics, should be investigated.

APPENDIX – IMPACT-ECHO DATA

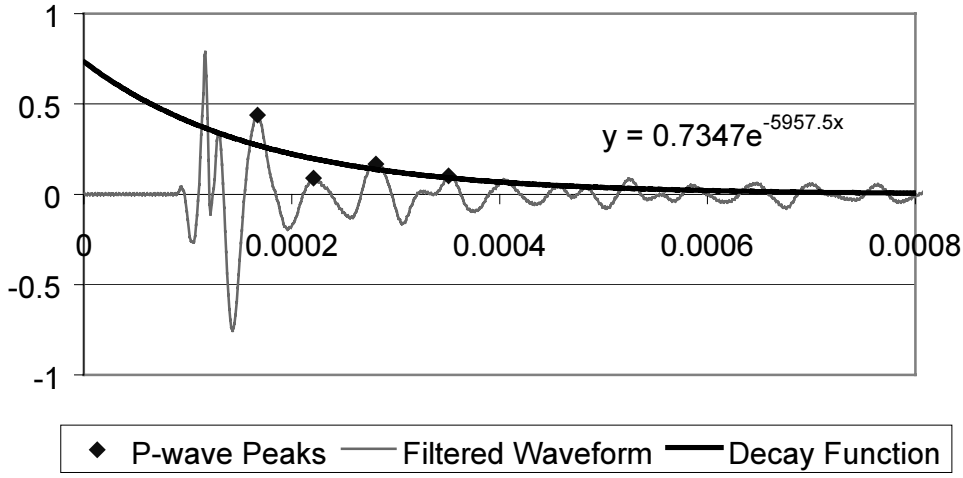

Figure A.1 - 1st Impact Echo test on BG1-8 Feet from Center

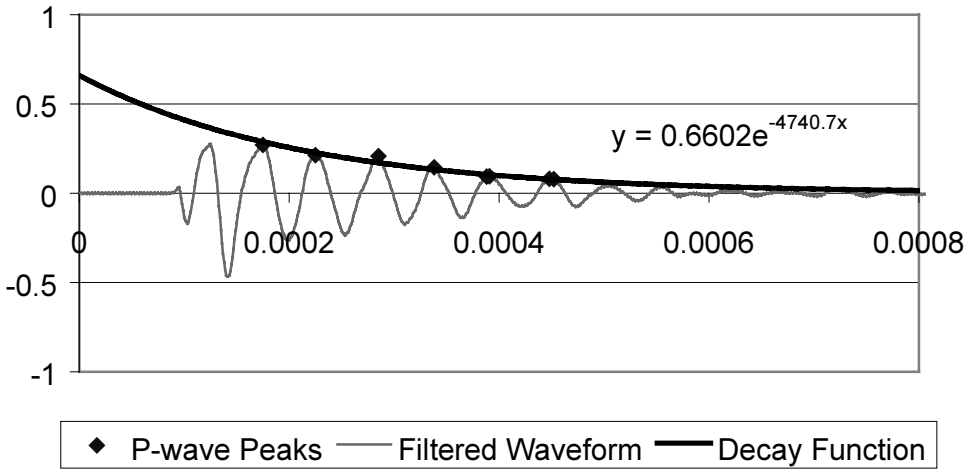

Figure A.2 - 2st Impact Echo test on BG1-8 Feet from Center

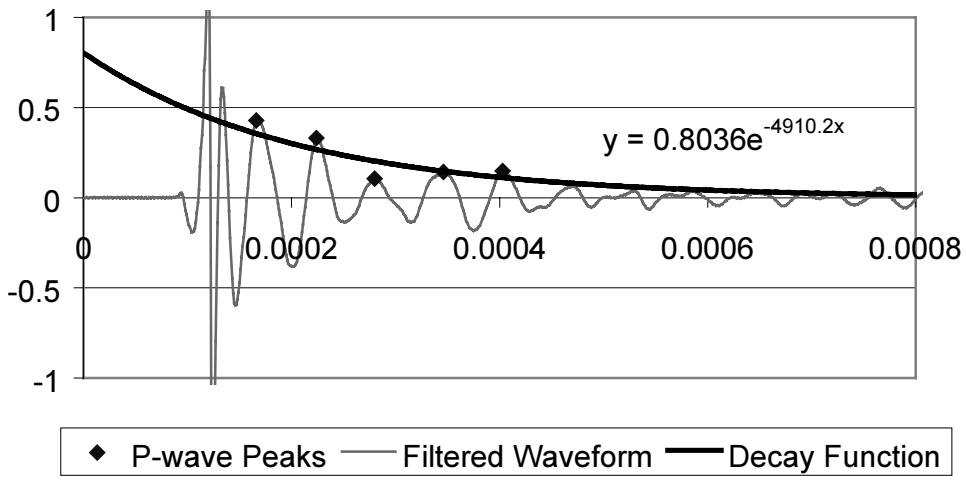

Figure A.3 - 1st Impact Echo test on BG1-7 Feet from South End

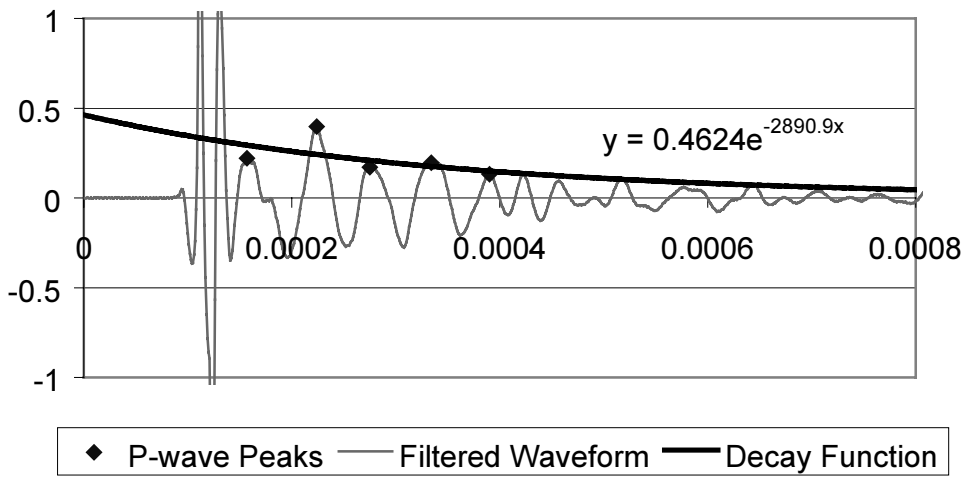

Figure A.4 - 2nd Impact Echo test on BG1-7 Feet from South End

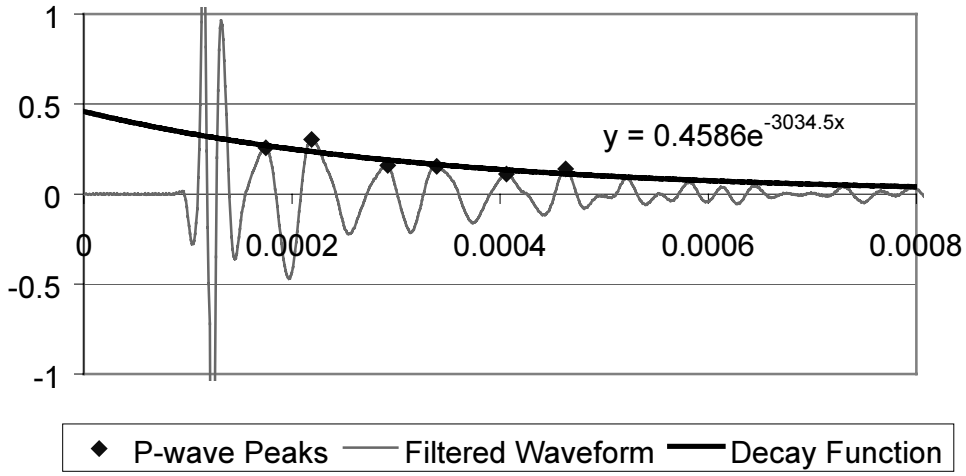

Figure A.5 - 1st Impact Echo test on BG1-5 Feet from South End

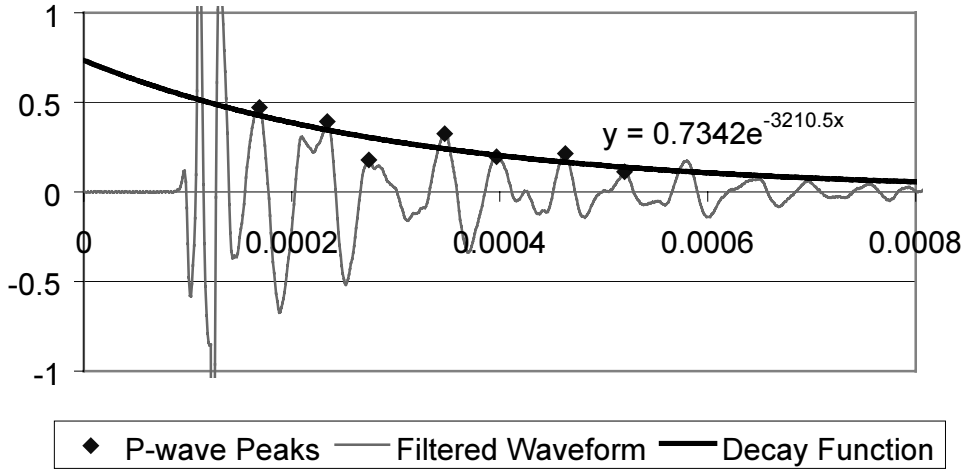

Figure A.6 - 2nd Impact Echo test on BG1-5 Feet from South End

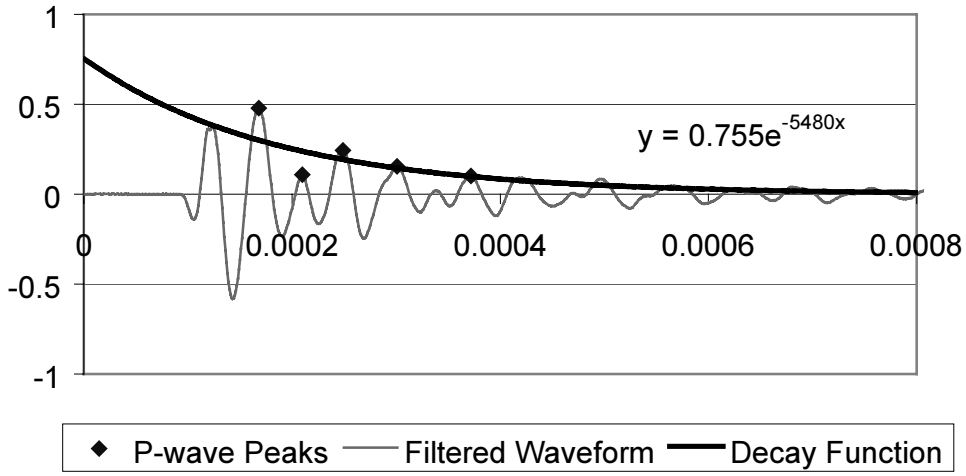

Figure A.7 - 1st Impact Echo test on BG3-3 Feet from North End

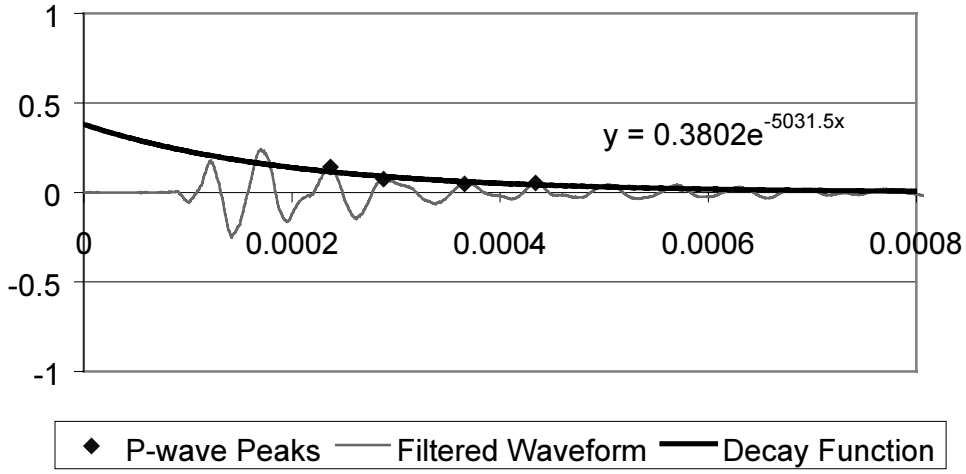

Figure A.8 - 2nd Impact Echo test on BG3-3 Feet from North End

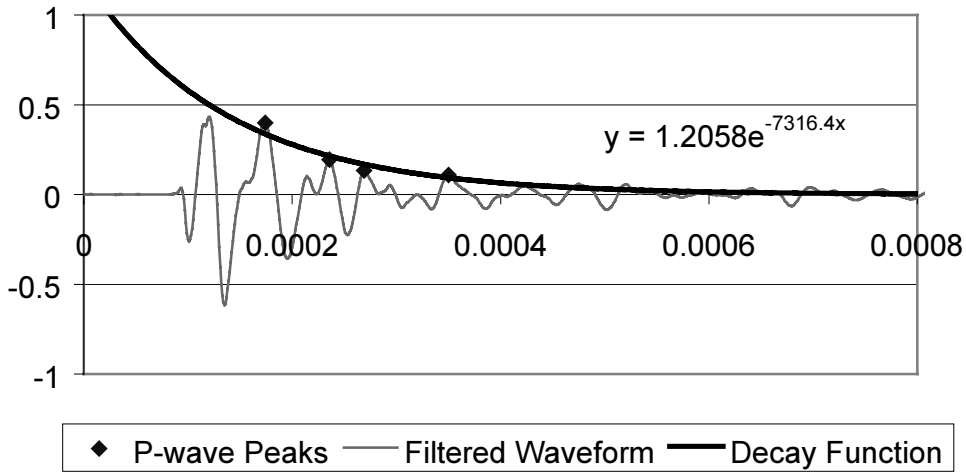

Figure A.9 - 1st Impact Echo test on BG3-22 Feet from South End

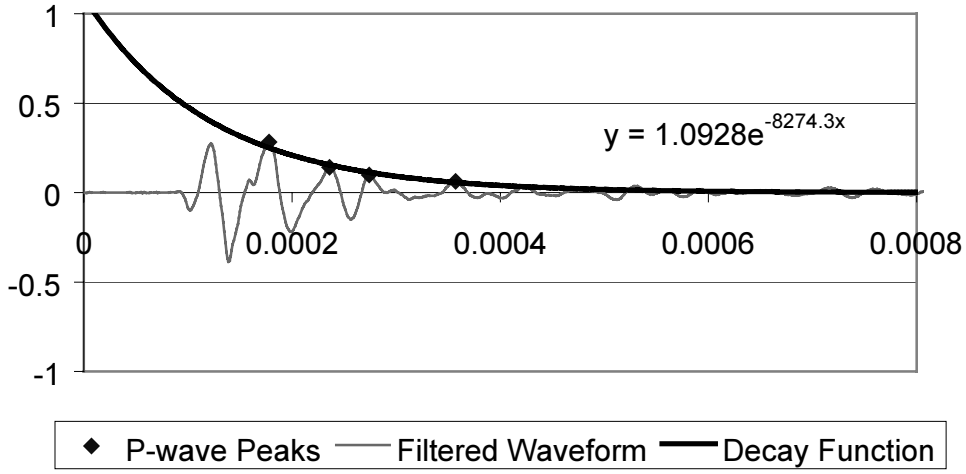

Figure A.10 - 2nd Impact Echo test on BG3 - 22 Feet from South End

REFERENCES

American Society of Mechanical Engineers, "Acoustic Emission Examination of Metallic Vessels during Pressure Testing" AMSE Code Section 5 Article 12, Boiler and Pressure Vessel Code, New York, 1998.

American Society of Nondestructive Testing, "Recommended Practice for Acoustic Emission Evaluation of Fiber Reinforced Plastic Tanks and Pressure Vessels," Committee on Acoustic Emission from Reinforced Plastics, Draft I October 1999.

American Society of Testing and Materials, ASTM E1316-94,"Standard Terminology of Nondestructive Examinations," 1994.

Association of American Railroads, Operation and Maintenance Department, "Procedure for Acoustic Emission Evaluation of Tank Cars and IM101 Tanks," Issue 8,Washington D.C. October 1999.

Barnes, C.A and Fowler, T.J. "Acoustic Emission Monitoring of Reinforced Concrete Structures," Proceedings of the Sixth International Symposium on Acoustic Emission from Composite Materials (AECM-6) San Antonio, Texas, American Society of Nondestructive Testing, June 1998, pp183-191.

Boenig, A., "Bridges with Premature Concrete Deterioration: Field Observations and Large-Scale Structural Testing," M.S. Thesis, University of Texas at Austin, May 2000

Bray, D.E., Stanley, R.K. "Nondestructive Evaluation a Tool in Design Manufacturing and Service," CRC Press, 1997.

Diederichs, U., Schneider, U. and Terrien, M., "Formation and Propagation of Cracks and Acoustic Emission," Development in Civil Engineering 7: Fracture Mechanics of Concrete, 1983, Edited by F.H. Wittman.

Fowler, T.J., Blessing, J.A., Conlisk, P.J., Swanson, T.L., "The Monpac System," *Journal of Acoustic Emission*, Volume 8, Number 3.

Fowler,T.J. "Experience with the Mandatory Acoustic Emission Test of an ASME Section X FRP Pressure Vessel," Proceedings of NACE Corrosion 97 Conference, Paper 370, 1997.

Funez, L.M., "Field Observations of Bridges with Premature Concrete Deterioration: Structural Implications," M.S. Report, University of Texas at Austin, December 1999.

Halmshaw, R "Non-Destructive Testing," Second Ed. Edward Arnold, London, England, 1991.

Ishibashi, A., Matsuyama, K., Ohta, S., Ohtsu, M., "Acoustic Emission Application for Diagnosis of Deteriorated Concrete of Harbor Structures."

Kamada, T., Iwanami,M., Nagataki, S., Yuyama, S. and Ohtsuki, N. "Application of Acoustic Emission Evaluation of Structural Integrity in Marine Concrete Structures," Progress in AE VIII (JSNDI), Proc. 13th Inter. AE Symp. Nov. 27-30, 1996, Nara Japan pp355-360.

Karabinis, A.H, and Fowler, T.J. "Experiences with Two Reinforced Concrete Aeration Basins," Presented at the 1983 Fall Convention, American Concrete Institute, Kansas City, Missouri September 25-30.

Karihaloo, B.L. and Nallathambi, P., "Notched Beam Test: Mode 1 Fracture Toughness," RILEM Technical Committee 89-FMT Report: Fracture Mechanics Test Methods for Concrete, 1989, Edited by S.P. Shah and A. Carpinteri.

Kesner, Keith Evan "Detection and Quantification of Distributed Damage in Concrete Using Transient Stress Waves," Thesis at Cornell University, December 1997.

Kim, Y. Personal Communication between Yong-mook Kim and Author at The University of Texas at Austin, March 2000.

Klingner, R.E., Fowler, T.J "Structural Assessment of In-Service Bridges with Premature Concrete Deterioration," Project Proposal for TxDot Project 0-1857, Submitted 1998.

Lawrence, 1997: Lawrence, B.L., E.D. Moody, R.N. Guillemette and R. L. Carrasquillo, "Evaluation and Mitigating Measures for Premature Concrete Deterioration in Texas Department of Transpiration Concrete Elements."

Malhotra V.M., Carino, N.J "CRC Handbook on Nondestructive Testing of Concrete" CRC Press, 1991.

Masi, A.K. and Sahu R. "Acoustic Emissions from Reinforced Concrete" *Experimental Mechanics*, December 1994 pp 379-388.

Murakami, Y. and Yuyama,S. "Acoustic Emission Evaluation of Structural Integrity in Reinforced Concrete Beams due to Corrosion of Reinforcement," Progress in AE VIII (JSNDI), Proc. 13th Inter. AE Symp. Nov. 27-30, 1996, Nara Japan pp217-244.

Nielsen, John and Griffen, D.F. "Acoustic Emission of Plain Concrete," *Journal of Testing and Evaluation*, JTEVA, Vol 5, No.6 , Nov 1977, pp 467-483.

Niseki, S., Satake, M. nad Gohke, m. "Quick Detection of Alkali-Aggregate Reaction by Acoustic Emission Monitoring," *Progress in Acoustic Emission V*, The Japanese Society of NDI, pg 529 1990.

Ohtsu, M "Determination of Crack orientaion by Acoustic Emission," *Materials Evaluation*, Sept 1987, pp 1070-1075.

Ohtsu, M "Estimation of Crack and Damage Progression in Concrete by Quantitative Acoustic Emission Analysis," *Materials Evaluation*, May 1999, pp521-525.

Ohtsu, M, Sakimoto, T., Kacai, Y., Yuji, S. "Evaluation of Concrete Structure Deterioration via AE Observation of Core Tests," *Journal of Acoustic Emission* Vol 7, No 4. Acoustic Emissions Group, pp 167-172, 1988.

Ohtsu, M. "Rate Process Analysis of AE Activity in Uniaxial Compression Test of Core Specimens" *Progress in Acoustic Emission V*, Japaneese Society of NDI, p 311, 1990.

Ohtsu, M., Okamoto, T., Yuyama, S. "Moment Tensor Analysis of Acoustic Emission for Cracking Mechanisms in Concrete," *ACI Structural Journal*, March-April 1998, pp 87-95.

"Report on Impact-Echo Evaluation of Distributed Cracking in Precast Concrete Beams," Prepared by Whitlock Dalrymple Posten & Associates, Inc., WDP Project No 99500, August 15, 1999.

Shiotani, T, Sakaino, N, Shigeishi, M, Ohtsu, M, Asai, Y, and Hayashi, T. "AE Characteristics of Full-Scale Concrete-Piles under Bending and Shear Load."

Uomoto, Taketo, "Application of Acoustic Emission to the Field of Concrete Engineering," *Journal of Acoustic Emis*sion, Vol 6, Nos 3, 1987 pp 137-144. Accoustic Emissions Group, Los Angeles, CA.

Yepez Roca, Luis Octavio "Acoustic Emission Examination of High Strength Prestressed Concrete Girders" Thesis presented to The University of Texas at Austin, August 1997.

Yuyama, S., Okamoto, T., Nagataki, S., "Acoustic Emission Evaluation of Structural Integrity in Repaired Reinforced Concrete Beams" Materials *Evaluation*, January 1994 pp 86-90.

Yuyama, S., Okamoto, T., Shigeiski, M., Ohtsu, M. "Acoustic Emission Generated in Corners of Reinforced Concrete Rigid Frame under Cyclic Loading," *Materials Evaluation*, March 1995 pp 409-412.